Waveguide Integrated MQW p-i-n Photodiodes

vorgelegt von
Dipl.-Ing.
Gan Zhou
geb. in Zhuji, China

von der Fakultät IV – Elektrotechnik und Informatik
der Technischen Universität Berlin
zur Erlangung des akademischen Grades

Doktor der Ingenieurwissenschaften
– Dr.-Ing. –

genehmigte Dissertation

Promotionsausschuss:

Vorsitzender: Prof. Dr. Wolfgang Heinrich

1. Gutachter: Prof. Dr.-Ing. Klaus Petermann

2. Gutachter: Prof. Dr. rer. nat. Martin Schell

3. Gutachter: Prof. Dr. Andreas Stöhr

Tag der wissenschaftlichen Aussprache: 19.07.2017

Berlin 2017

Zusammenfassung

In der vorliegenden Arbeit werden Wellenleiter integrierte Multi-Quantum-Well (MQW) p-i-n Photodioden entwickelt und charakterisiert. Im Vergleich zu Bulk Photodioden haben MQW-Photodioden besondere Eigenschaften, wie zum Beispiel einen hohen und einstellbaren Polarization-Dependent-Loss (PDL). Dies macht MQW-Photodioden zu einem potenziellen Kandidaten für unterschiedliche Anwendungen, besonders für Polarization-Diversität kohärente Empfänger. Außerdem können MQW-Photodioden die monolithische Integration von opto-electronischen Schaltungen vereinfachen.

Das Design von Wellenleiter integrierten MQW p-i-n Photodioden basiert auf dem Modell, das in dieser Arbeit dargestellt wird. Das Modell gilt für das Spektrum der Empfindlichkeit, den PDL, die 3-dB Bandbreite, die DC- und RF-Sättigungsabsorption und die Nichtlinearität. Die wichtigen physikalischen Effekte für das Modell sind die Transitzeit und die Dichte der freibeweglichen Ladungsträger in den MQW-Schichten. Beide Effekte beeinflussen die interne Quantum-Effizienz, die optische Sättigungsabsorption, und die 3-dB Bandbreite. Das Modell berücksichtigt den Einfluss des elektrischen Feldes (der Spannung) und der optischen Eingangsleistung.

Anschließend wird das Modell durch den Vergleich der Messergebnisse von drei erstellten Designs verifiziert. Die drei Designs werden durch die Empfindlichkeit, die Bandbreite, die maximale RF-Ausgangsleistung und die Nichtlinearität charakterisiert. Das Design „InP“ weist den höchsten PDL auf, wegen den stark beschränkten Exzitonen in den MQW-Schichten. Aufgrund der reduzierten Transitzeit haben die Designs „Q1.33” und „Al” bessere RF-Eigenschaften als das Design „InP“. Jedoch liefern die beiden Designs niedrigere PDL-Werte, wegen den schwächer beschränkten Exzitonen in den MQW-Schichten. Dann wird ein neues Design von Wellenleiter integrierten MQW p-i-n Photodioden dargestellt. Das neue Design benutzt die MQW Schichten mit einer kompressiven Verspannung. Die Simulationsergebnisse zeigen, dass das neue Design den hohen PDL des Designs „InP“ und die gute RF-Eigenschaft der Designs „Q1.33“ und „Al“ kombiniert.

Am Ende wird ein verbesserter kohärenter Empfänger mit den dargestellten Designs demonstriert.

Abstract

In this work, waveguide integrated multiple quantum well p-i-n photodiodes are developed and characterized. Compared to bulk photodiodes, multiple quantum well photodiodes have special properties including a large and tunable polarization dependent loss. It makes multiple quantum well photodiodes a potential candidate for various applications, especially in polarization-diversity coherent optical receivers. Furthermore, multiple quantum well photodiodes are supposed to simplify monolithic integration of optoelectronic circuits.

The design of waveguide integrated multiple quantum well p-i-n photodiodes is based on the model presented in this thesis. The model accounts for responsivity spectrum, polarization dependent loss, 3-dB bandwidth, DC and RF saturation, and nonlinearity. The important physical effects for the modeling of multiple quantum well photodiodes are the carrier transit time through the multiple quantum well layers and the free carrier density in the quantum wells. Both effects influence the internal quantum efficiency, the saturation of optical absorption, and the RF bandwidth. The model considers the influences of electrical field (bias voltage) and optical input power.

The model is verified by comparing to the measurement results of three fabricated designs of waveguide integrated multiple quantum well p-i-n photodiodes. The three designs are characterized in terms of responsivity, polarization dependent loss, dark current, DC saturation of optical absorption, bandwidth, maximum RF output power, and nonlinearity. Among them, the design “InP” shows the highest polarization dependent loss because of its strongly confined excitons in wells. However, its RF performances such as the 3-dB bandwidth and the RF output power are limited by its large transit time. Compared to the design “InP”, the design “Q1.33” and the design “Al” exhibit better RF performances thanks to their reduced transit time. However, due to the weaker confinement of excitons in wells they provide lower polarization dependent loss values. By using compressive strains in wells, a new design of the waveguide integrated MQW p-i-n PD is presented. The simulation results show that this new design combines the high-PDL performance of the design “InP” and the high-RF performance of the design “Q1.33” and the design “Al”.

In the end, a novel advanced coherent receiver using proposed waveguide integrated multiple quantum well p-i-n photodiodes is demonstrated.

Contents

1. Introduction

1.1 Motivation

Since quantum wells (QWs) were firstly observed in the 1970s by Bell Laboratories [1], they have been widely used in many electro-optics and optical-electro devices, such as lasers, modulators, and long-wavelength infrared detectors. Compared to the conventional lasers with bulk active layers, quantum well lasers have several advantages [1], such as higher gain and lower chirp. There are two popular types of quantum well based modulators. One is the electro-absorption modulator (EAM) and the other is the Mach-Zehnder modulator (MZM). Both modulators using quantum wells are based on the Quantum-Confined Stark Effect (QCSE). These modulators have a higher extinction ratio and higher modulation efficiency compared to the modulators using bulk materials [2]. Quantum wells can also be used in long-wavelength infrared detectors (from about 2μm to 20μm). These long-wavelength infrared detectors are based on the intersubband transitions in lightly doped quantum wells [3]. Compared to bulk long-wavelength infrared detectors, these detectors have a higher degree of uniformity, lower auger recombination rates, and tunability of the upper cutoff wavelength. Nowadays, the researches and fabrication techniques of the quantum well lasers, modulators, and long-wavelength detectors are well developed.

For optical fiber communication systems (wavelength range of 0.8 to 1.6μm), intrinsic multiple quantum wells (MQWs) can be used as the absorber of the photodiodes (PDs). Compared to the bulk PDs, these MQW PDs have a special property: larger and tunable polarization dependent loss (PDL) [4]. This unique property makes MQW PDs a potential candidate for various applications such as polarization-diversity coherent optical receivers. Moreover, MQW PDs are supposed to simplify monolithic integration of optoelectronic circuits. Nowadays, monolithic integration becomes more and more critical to achieve lower cost, higher reliability and improved performance [5]. A lot of efforts have been carried out to integrate different optical components on one single substrate. EAMs integrated with distributed feedback (DFB) lasers were demonstrated by K. Wakita [6]. R. Nagarijan integrated a tunable laser sources with EAMs and semiconductor optical amplifiers (SOAs) [7]. For all-optical signal processing, T. Yoshimatsu realized optical logic gates by integrating an EAM and PD [8]. A single chip transceiver was demonstrated with a monolithic integrated distributed Bragg reflector (DBR) laser, an EAM, a PD, and a SOA by J. W. Raring [9]. However, in order to integrate a bulk PD with other components such as laser, EAM, and SOA, regrowth and other complex processes are necessary because

most lasers, EAMs, and SOAs are made of a MQW structure to fulfill their properties as mentioned above. One effective solution to overcome this problem is to implement PDs with a MQW structure as an absorption region instead of bulk absorption regions.
There are a few research activities about MQW PDs. J.C Dries proposed an avalanche photodiode using strain-compensated InGaAs quantum wells [10] with a 2 μm cutoff wavelength. A multiple quantum well photodiode was demonstrated based on Ge/SiGe with 30 GHz bandwidth [11]. T. Bhowmick and S.S. Agashe proposed waveguide photodiodes using multiple quantum wells for the C-Band [12] [13]. However, no systematical analysis and no commercial design tools e.g. modeling of this kind of photodiodes have been presented so far. In this work, MQW PDs are systematically studied and modeled. I focus on the waveguide integrated MQW p-i-n PD based on III-V semiconductor materials.

1.2 Thesis outline

This work covers the theoretical aspect, the modeling, the design, and the analysis of the waveguide integrated MQW p-i-n PDs. Chapter 2 presents the theory of the waveguide integrated MQW p-i-n PD, including the band structures, the optical properties of MQWs, and the physical effects such as the carrier transit time and the free carrier density in the MQW PDs. In chapter 3 a model of a waveguide integrated MQW p-i-n PD is developed. The model accounts for optical absorption coefficient, responsivity, PDL, dark current, 3-dB bandwidth, DC and RF saturation, and nonlinearity. The important physical effects such as the carrier transit time and the free carrier density in MQWs are considered in the model. Chapter 4 summarizes the design and the fabrication processes of the waveguide integrated MQW p-i-n PDs. Chapter 5 presents the measurement results, including the responsivity, the PDL, the dark current, the DC saturation of optical absorption, the bandwidth, the maximal RF output power, and the nonlinearity of the devices. The measurements results are analyzed and compared with the simulation results based on the proposed model. Using the proposed waveguide integrated MQW p-i-n PD with large PDL, an advanced dual-polarization coherent receiver is demonstrated in chapter 6. Finally, the work in this dissertation is summarized in chapter 7. Some ideas for future work are proposed.

2. Theory of waveguide integrated MQW p-i-n PD

In this chapter, brief overviews of the p-i-n PD and the waveguide integrated PD are presented to address the choice of the waveguide integrated MQW p-i-n PD. After that the band structure and the optical properties of the MQW structures are introduced. In the end some physical effects in waveguide integrated MQW p-i-n PDs are discussed.

2.1 The waveguide integrated p-i-n PD

2.1.1 The p-i-n PD

A photodiode absorbs the optical signal and converts it into an electrical signal. Only by absorbing the light with the photon energy at least equal to the bandgap energy E_g of the absorber material, an electron can be excited from the valence band to the conduction band. For this band-to-band transition, the long-wavelength cut-off for photon absorption λ_g is given by

$$\lambda_g = \frac{hc}{E_g} = \frac{1.24}{E_g(\mathrm{eV})}\ (\mu\mathrm{m}) \tag{1}$$

where h is the Planck constant and c is the velocity of light in vacuum. Once an electron-hole-pair is created, the electron and hole can be transported with the applied electric field resulting in an induced current [14]. The interaction of current with external circuits provides the output signal [15].

Normally the material with a direct bandgap is preferred for the light absorption, since the absorption constant is high near the bandgap. Today's optical fiber exhibits minimum loss and minimum dispersion at 1.55µm and 1.3µm, respectively. For these telecom fiber applications, the photodiode material system should allow for a composite of highly absorbing and transparent layers for the wavelength range between 1.3µm and 1.6µm. The compound semiconductor system InGaAsP, grown lattice matched on InP substrate with a direct bandgap, fulfills these requirements. By varying compositions of the alloys, the bandgap can vary between 0.75eV (λg = 1.65µm) and 1.35eV (λg = 0.92µm). The ternary composite InGaAs lattice matched to InP is used in this thesis as the light absorbing material, which shows an absorption constant α of 7000cm^{-1} at 1.55µm wavelength [16].

The general characteristics of a photodiode are considered as quantum efficiency, responsivity, response speed, and saturation absorption. The external quantum

efficiency η_{ext} is the externally measured number of charge carrier pairs generated per incident photon

$$\eta_{ext} = \frac{I_{PD}}{e} \cdot \frac{h\upsilon}{P_{opt}} \tag{2}$$

where I_{PD} is the photogenerated current, e is the elementary electric charge, and P_{opt} is the incident optical power at the optical frequency of υ. When each photon generates one electron-hole-pair and neither photons nor carriers are lost, the external quantum efficiency η_{ext} equals 1. The responsivity is the ratio of the photocurrent to the optical power

$$R = \frac{I_{PD}}{P_{opt}} = \frac{\eta_{ext}\lambda(\mu m)}{1.24} \left[\frac{A}{W}\right]. \tag{3}$$

Thus, for a given external quantum efficiency, the responsivity increases linearly with wavelength. The responsivity can depend on the state of the polarization of the incoming light. The polarization dependent loss (*PDL*) is defined as

$$PDL = 10 \log\left(\frac{R_{max}}{R_{min}}\right) [dB]. \tag{4}$$

The response speed is determined by the combination of two factors: the carrier transit time and the *RC* time constant [17]. The depletion layer must not be too

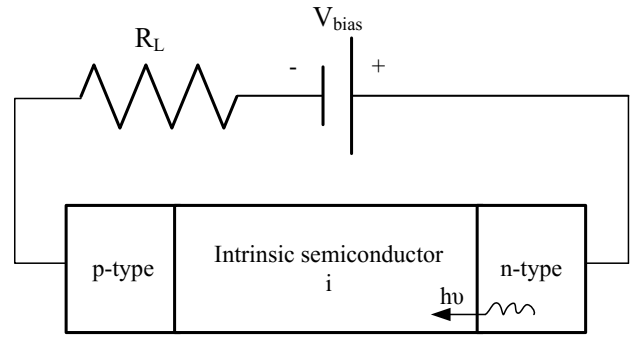

(a)

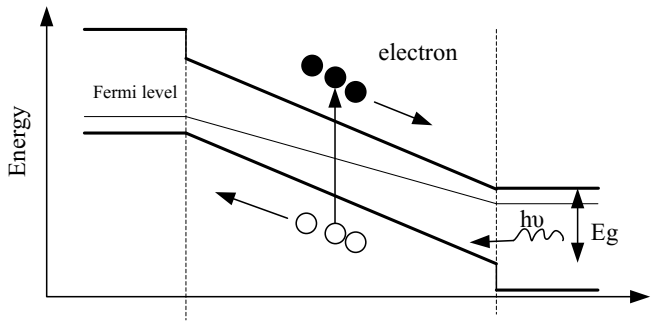

(b)

Fig. 1 (a) Cross-sectional view of a p-i-n diode at a reverse bias with an external load R_L. (b) Energy band structure of a p-i-n diode under a reverse bias [15].

wide; otherwise, the large carrier transit time through the depletion layer will limit the frequency response. It should also not be too thin; otherwise, the large capacitance due to the thin depletion layer will result in a large *RC* time constant limiting the bandwidth. At high optical input power, the performance of the photodiode will be affected, which is called as optical saturation absorption. There are many limiting factors such as the space charge effect, the thermal failure, and the voltage drop at external load [17].

There are many photodiode types, including the p-n junction diode, the p-i-n diode, the metal-semiconductor diode (Schottky barrier), and the heterojunction diode. The p-i-n photodiode is one of the most common photodetectors, because the thickness of depletion region can be tailored to optimize the quantum efficiency and frequency response.

Fig. 1(a) shows the schematic representation of a p-i-n diode. An intrinsic absorber layer is sandwiched between p- and n-type contact layers. Fig. 1(b) depicts the energy band structure of the heterostructure using InGaAs as absorber and InGaAsP as contact layers. The p- and n-type contact layers are designed to be transparent for the incoming light through the n-contact layer as shown in Fig. 1(b). As a result, the electron-hole-pairs are solely generated in the depletion region. The photon generated electron-hole-pairs will eventually be separated by the electric field as shown in Fig. 1(b), leading to current flow in the external circuits as carriers drift across the depletion layer [15]. Compared to the p-n photodiode, the p-i-n photodiode has many advantages. The thicker depleted absorber in a p-i-n PD offers higher responsivity and lower junction capacitance. The transparent contact layers eliminate the slow diffusion photocurrent. Moreover, there is an additional degree of freedom in the design of the depletion width to tailor the PD performances.

2.1.2 The waveguide integrated PD

To design a high-performance PD, some Figures of Merits (FoMs) have to be considered, such as a high responsivity, a high bandwidth, a high saturation photocurrent, and a high linearity. There are three common design approaches as shown in Fig. 2. In vertically-illuminated p-i-n PDs in Fig. 2(a) and (b), the input light travels through the p-contact (top-illuminated p-i-n PD) or the n-contact and the substrate (back-illuminated p-i-n PD). The input light is absorbed in the intrinsic absorber layer. To get a high responsivity, the thickness of the absorber should be large. However the thick absorber increases the transit time limiting the bandwidth. The bandwidth-efficiency-product (bandwidth × quantum efficiency) is limited to approximately 20GHz for top-illuminated p-i-n PD [18]. For back-illuminated p-i-n PD, the light can be reflected by the top metal and absorbed again in the absorber leading to a larger product of 35GHz [19].

To overcome the trade-off caused by the absorber thickness of the surface illuminated PD, the side-illuminated waveguide p-i-n PD is used as shown in Fig. 2(c). The absorber is embedded in an optical waveguide. In this PD, the optical absorption path is oriented perpendicular to the electrical field, since the light is laterally injected into the thin absorber layer. Thus, the carrier transit time and the responsivity are determined by two separated parameters: the absorber thickness determines the carrier transit time, while the absorber length controls the responsivity. A bandwidth-efficiency-product of 55GHz was achieved by K. Kato [20]. However, because of the low tolerance to lateral and vertical displacement of

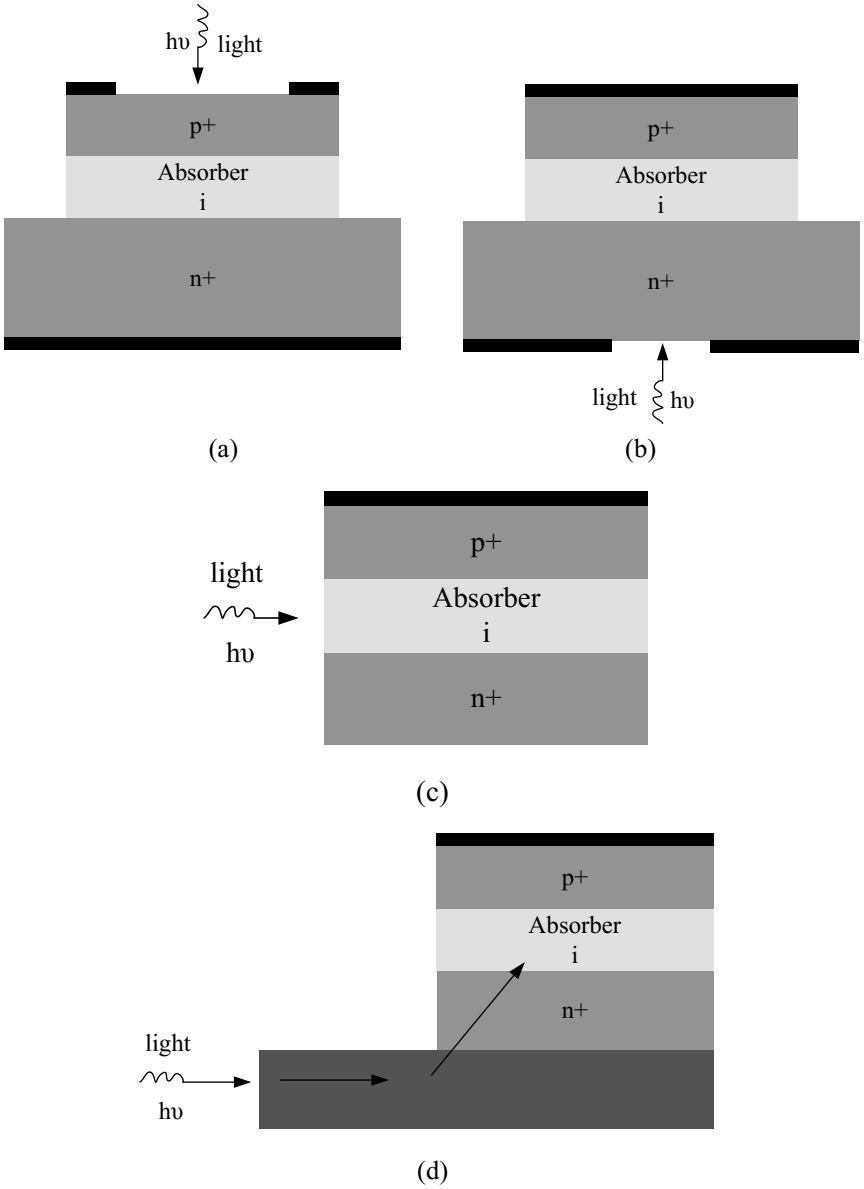

Fig. 2 Various photodiode approaches: (a) a top-illuminated p-i-n PD; (b) a back-illuminated p-i-n PD; (c) a side-illuminated waveguide p-i-n PD; (d) a waveguide integrated p-i-n PD based on the evanescent coupling.

the input light, this design implies the use of further optics or a tapered fiber for coupling. It makes the fiber-chip coupling more crucial and complex [16].
The waveguide integrated p-i-n PD in Fig. 2(d) offers the same benefits as the side-illuminated waveguide p-i-n PD and even more advantages. The input light travels along the optical waveguide and couples evanescently to the PD mesa located on top of the waveguide. This evanescent coupling ensures a more uniform power distribution in the absorber, improving the high-power capability [21]. An on-chip integrated spot size converter can be used for the fiber-chip alignment. Thus a cleaved fiber instead of tapered fiber can be used, which increases the coupling efficiency and alignment tolerances [16]. Moreover, the waveguide integrated p-i-n PD enables advanced monolithic integration with other components such as the power splitter, the multi-mode-interference (MMI), and the polarization beam splitter (PBS).
Considering the advantages of the p-i-n PD and the waveguide integrated PD, we put the focus on the waveguide integrated p-i-n PD using MQW as the absorber in this thesis.

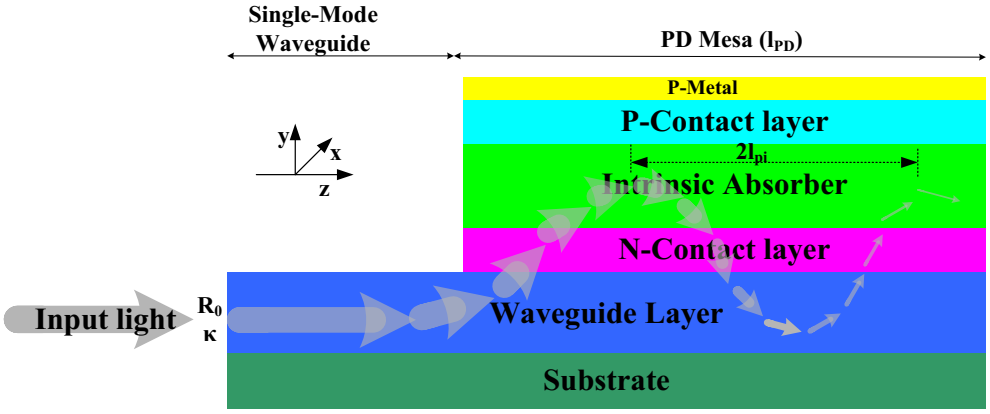

Fig. 3 Side view of the light distribution along the waveguide integrated PD.

Fig. 3 gives an example of a waveguide integrated p-i-n PD with light propagation. The PD Mesa (p-i-n PD structure) is located on top of the waveguide layer. The refractive indices of the waveguide layer, the n-contact layer, and the absorber layer should fulfill the following inequation: $n_{waveguide} < n_{n\text{-}contact} < n_{absorber}$ to ensure that the light will be coupled from waveguide to the p-i-n PD. The p-contact should have a smaller refractive index than the absorber ($n_{p\text{-}contact} < n_{absorber}$) to prevent the light from getting into the p-contact metal. Fig. 4 shows the simulated TE modes in *xy* plane for (a) the rib waveguide, (b)-(d) the PD mesa with a PD width of 5µm and a waveguide width of 2µm. The evanescent coupling of the light from waveguide to the p-i-n PD is the result of the mode beating effects between TE_{12} and TE_{13} modes in the PD mesa. The beat length l_{pi} can be calculated

$$l_{pi} = \frac{\pi}{|\beta_{TE_{12}} - \beta_{TE_{13}}|} = \frac{\lambda}{2\left(Re\left(N_{eff,TE_{12}}\right) - Re\left(N_{eff,TE_{13}}\right)\right)} \quad (5)$$

where $\beta_{TE_{12}}$ and $\beta_{TE_{13}}$ are the propagation constant for TE_{12} and TE_{13} mode, respectively. $Re\left(N_{eff,TE_{12}}\right)$ is the real part of the effective index of TE_{12} mode $N_{eff,TE_{12}}$, $Re\left(N_{eff,TE_{13}}\right)$ is the real part of the effective index of TE_{13} mode $N_{eff,TE_{13}}$, and λ is the wavelength. To obtain a quantum efficiency of η ($0<\eta<1$), the designed PD length l_{PD} can be estimated as:

$$l_{PD} = \frac{-\lambda \ln(1-\eta)}{4\pi\left(Im\left(N_{eff,TE_{12}}\right) + Im\left(N_{eff,TE_{13}}\right)\right)/2} \quad (6)$$

where $Im\left(N_{eff,TE_{12}}\right)$ is the imaginary part of the effective index $N_{eff,TE_{12}}$ of TE_{12} mode and $Im\left(N_{eff,TE_{13}}\right)$ is the imaginary part of the effective index $N_{eff,TE_{13}}$ of TE_{13} mode.

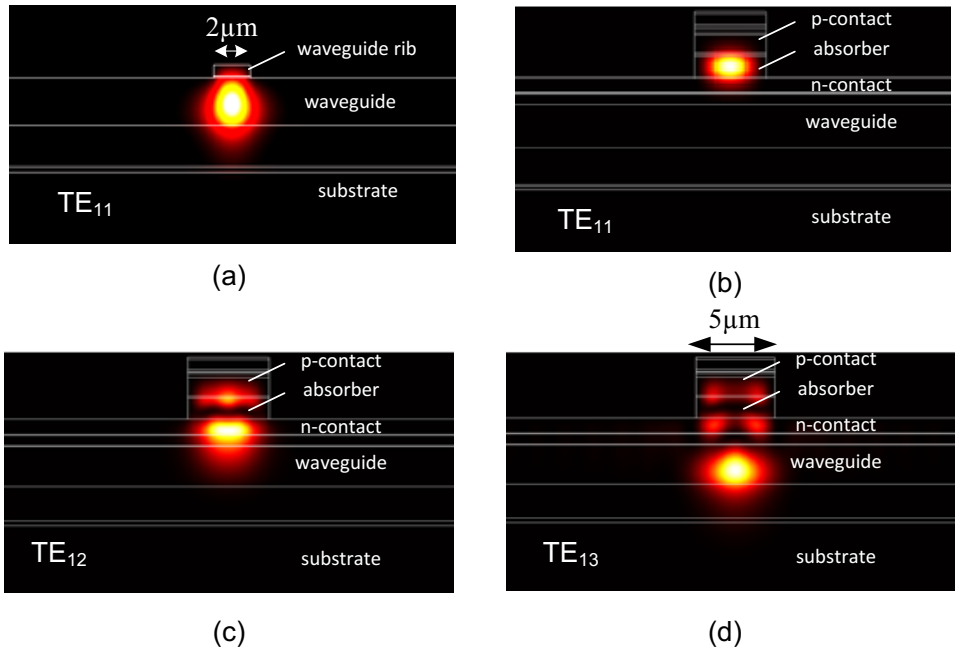

Fig. 4 Simulated TE intensity mode profiles of (a) single-mode rib waveguide, (b)-(d) PD mesa. (b)-(d) are the first, second, and third vertical modes, respectively in PD mesa.

2.2 Semiconductor band structure

Multiple quantum wells are thin layered semiconductor structures in which electrons and holes are strongly confined. Due to the quantum confinement of electrons and holes, many of the physical effects in MQWs can be observed and controlled at room temperature. For example, the "exciton", which can be easily seen in MQW structures at room temperature, is one of the most important

phenomena. MQW structures have many unique properties compared to bulk structures. One of them is the stronger absorption over narrow bands of photon energies. Besides, the absorption strength of the light can be strongly dependent on the polarization status of the input light (large PDL). Many of the effects, such as PDL and upper cut-off absorption wavelength, can be further tuned by varying the geometry or materials of quantum wells or introducing strain effects in quantum wells. These physical effects can be exploited in real devices.

2.2.1 Band structure for bulk structures

According to the quantum theory, the light absorption and generation are both based on the electron transition between two different electron energy levels with the presence of the light or free carriers. Thus, it is quite necessary to study the energy distributions in semiconductors to design the corresponding devices.
With absence of any electromagnetic fields, an electron in a vacuum at a position $\boldsymbol{r}$ can be described by a wave function φ [22]

$$\varphi = \mathrm{e}^{j(\boldsymbol{k}\cdot\boldsymbol{r}-\omega t)} \tag{7}$$

where t is the time, ω is the angular frequency, $\boldsymbol{r}$ is the position vector, and the wave vector is given by

$$\mathrm{k} = |\boldsymbol{k}| = \left|k_x\boldsymbol{e}_x + k_y\boldsymbol{e}_y + k_z\boldsymbol{e}_z\right| = \frac{2\pi}{\lambda} \tag{8}$$

where $\boldsymbol{e}_x$, $\boldsymbol{e}_y$, and $\boldsymbol{e}_z$ are the unit vector of the coordination system. The wave function φ and energy E of an electron obey the time-independent Schrödinger equation [23]

$$-\frac{\hbar^2}{2m}\nabla^2\varphi = \mathrm{E}\varphi \tag{9}$$

where $\hbar$ is the reduced Planck constant ($\hbar=h/2\pi$), h is the Planck constant, m is the mass of the electron, and ∇ is given by

$$\nabla = \frac{\partial}{\partial x}\boldsymbol{e}_x + \frac{\partial}{\partial y}\boldsymbol{e}_y + \frac{\partial}{\partial z}\boldsymbol{e}_z. \tag{10}$$

The dispersion (energy versus momentum $\boldsymbol{p}$ which is proportional to the wave vector $\boldsymbol{k}$ ($\boldsymbol{p}=\hbar\boldsymbol{k}$)) curve of this electron is illustrated in Fig. 6 (solid curve). The total energy E for this electron in a vacuum ignoring the influence of electromagnetic fields is only the kinetic energy E_k given as the following

$$E = E_k \approx \frac{\hbar^2 k^2}{2m}. \tag{11}$$

However, the situation will be much more complex if an electron is in a bulk material. For simplicity, the so called *effective mass approximation* has been found to be very suitable to describe the time-independent Schrödinger equation at relatively low electron momentum ($k \approx 0$) [23]

$$-\frac{\hbar^2}{2m^*}\nabla^2\varphi = \mathrm{E}\varphi. \tag{12}$$

where m^* is the effective mass of an electron in a bulk material. The energy of an electron in a bulk material and its wave function are expressed as [1]

$$E = \frac{\hbar^2 k^2}{2m^*}, \quad \varphi = e^{j\mathbf{kr}}u(\mathbf{k},\mathbf{r}) = F(\mathbf{r})u(\mathbf{k},\mathbf{r}) \tag{13}$$

where $F(\mathbf{r})$ is an envelope function and $u()$ is a Bloch function with the special property that it is periodic with the crystal lattice and repeats itself in each unit cell

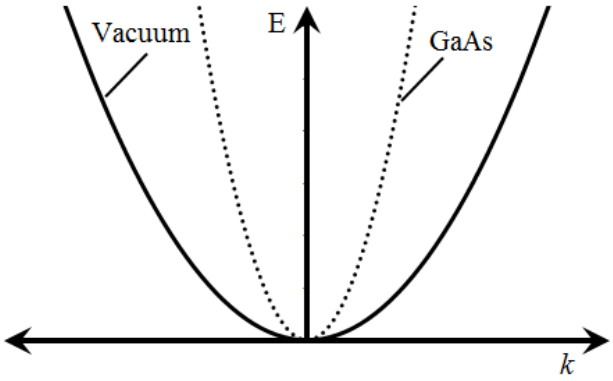

Fig. 6 The dispersion curve for an electron in a vacuum (solid curve) and an electron in GaAs (dotted curve) [23].

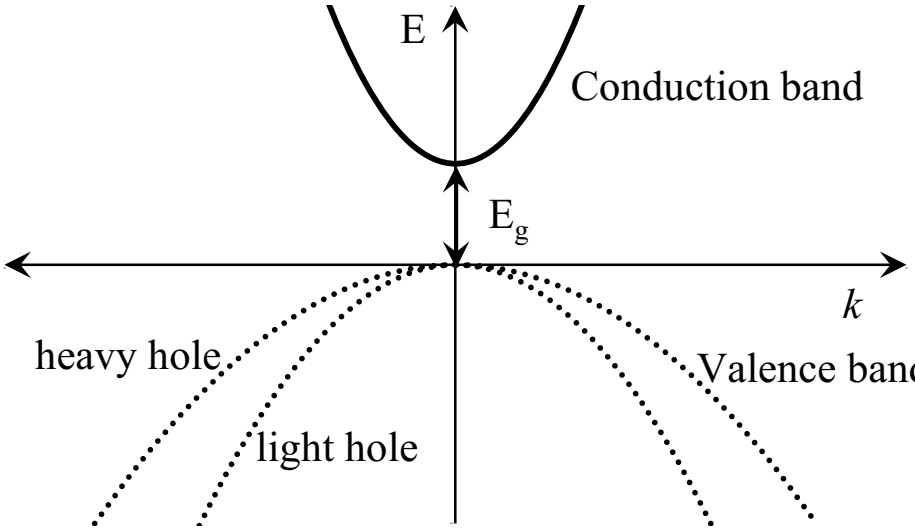

Fig. 5 The dispersion curve for an electron in the conduction band (solid curve), a heavy hole and a light hole in the valence band (dotted curve) [23].

of the crystal [24].

The effective mass m^* is a quantity that is used to simplify band structures by constructing an analogy to the behavior of a free particle with that mass, which can be represented by the curvature of the dispersion curve at $k \approx 0$. The effective mass has been revealed to be anisotropic, since the crystal potential along the [001] axis is different from that along the [111] axis [23]. Fig. 6 shows the dispersion curve for the electron effective mass in GaAs, in comparison with that of an electron in a vacuum [23].

Fig. 5 shows the energy versus wave vector curves for an electron in the conduction band (solid curve) and a hole in the valence band (dotted curve). The valence bands are known as the heavy hole (hh) and light hole (lh) band. The conduction band represents excited electron states. With the presence of an applied electric field, these electrons are accelerated to contribute to a current flow. The lowest energy difference between the two bands is called as the bandgap E_g which is shown in Fig. 5. According to the *effective mass approximation*, the electrons in the conduction band, the heavy holes and the light holes in the valence band behave as particle with different effective mass along different crystal axis.

The *effective mass approximation* is used for bulk materials. When two materials are placed adjacent to each other to form a heterojunction, this approximation is only valid with each material using the effective mass as a function of position. Considering the different bandgaps of different materials, the Schrödinger equation for this heterojunction can be expressed as [23]

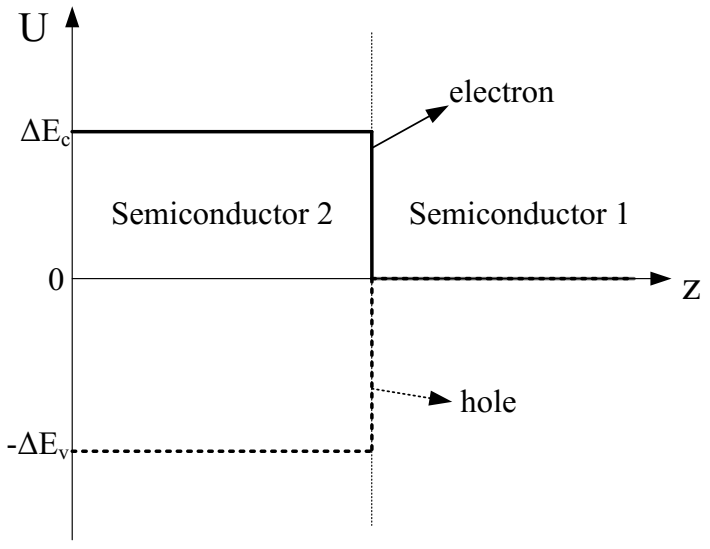

Fig. 7 The one-dimension potential energy *U(z)* in the conduction band (for electrons) and valence band (for holes) at a heterojunction [23].

$$-\frac{\hbar^2}{2m^*(z)}\nabla^2\varphi_e + \mathrm{U}_e(\mathrm{z})\varphi_e = \mathrm{E}_e\varphi_e \quad \text{for electrons} \tag{14}$$

$$-\frac{\hbar^2}{2m^*(z)}\nabla^2\varphi_h - \mathrm{U}_h(\mathrm{z})\varphi_h = \mathrm{E}_h\varphi_h \quad \text{for holes} \tag{15}$$

where $m^*(z)$ is the position z dependent effective mass and $U(z)$ is a constant potential energy representing the discontinuity in either the conduction (U_e) or the valence band (U_h) between two materials as shown in Fig. 7. The "band offset ratio" is used as an experimental quantity to join the two semiconductor materials together. It is the ratio of the conduction band energy difference ΔE_c to the band gap difference $\Delta E_g = E_{g1} - E_{g2}$, as shown in Fig. 8. The conduction band energy difference ΔE_c and the valence band energy difference ΔE_v fulfill the equation of $\Delta E_c + \Delta E_v = \Delta E_g$. Different heterojunction has different band offset ratio ($\Delta E_c/\Delta E_g$). For example, for undoped InP/InGaAsP heterojunction, the ratio is about 0.4, while for undoped InGaAlAs/InGaAsP heterojunction, the ratio is about 0.7.

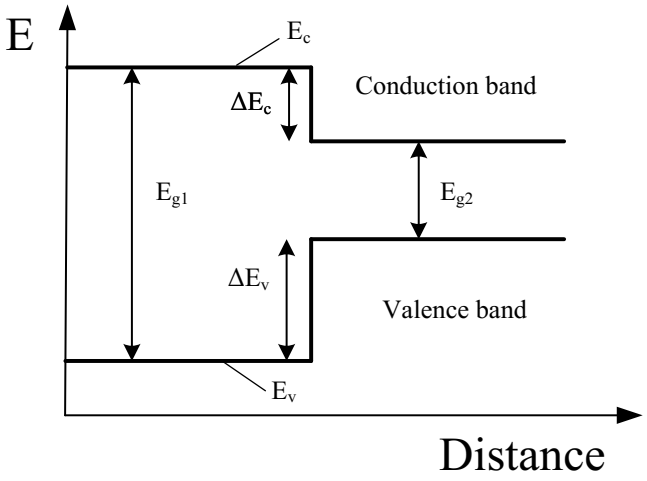

Fig. 8 The band diagram of an InP/InGaAsP heterojunction.

2.2.2 Band structure for quantum well structures

The heterostructure is the combination of multiple heterojunctions. For example, as shown in Fig. 9 a material layer "1" with a narrower band gap is sandwiched between two material layers "2" with a wider band gap. The both materials are undoped. That forms a double-heterojunction.

If layer "1" is sufficiently thin (about tens of atomic layers) for quantum properties to be exhibited, this heterostructure is called as single quantum well (SQW). The layers "1" and "2" are called as "well" and "barrier", respectively. Normally, there are two types of systems. All the structures illustrated so far are examples of type-I system. In this particular material system type, electrons have higher energies in

barriers than in the wells ($E_c(2)>E_c(1)$) and holes have lower energies in barriers than in the wells ($E_v(2)<E_v(1)$). The band gap of well material is fully inserted within the band gap of barrier material. Thus, any electrons or holes falling into the quantum wells are within the same layer of material as shown in Fig. 9. The electrons and holes in the type-I system recombine quickly. In this thesis only the type-I system is considered.

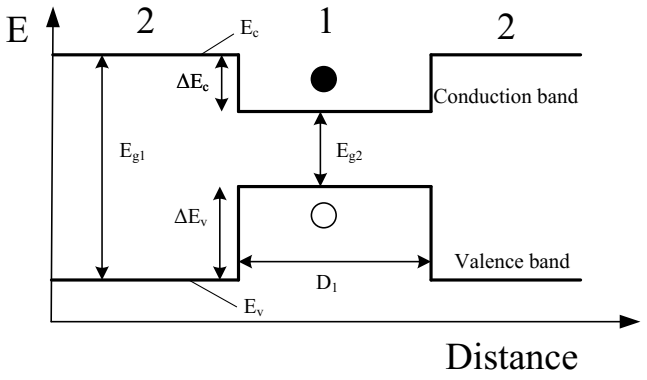

Fig. 9 The band diagram of a type-I double-heterojunction. Material 1 as the well, and material 2 as the barrier.

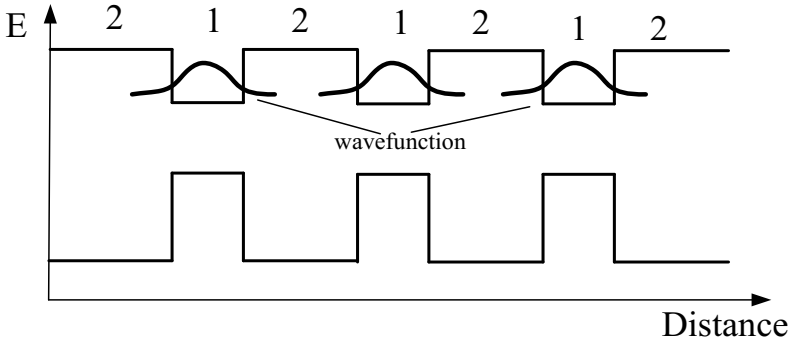

(a)

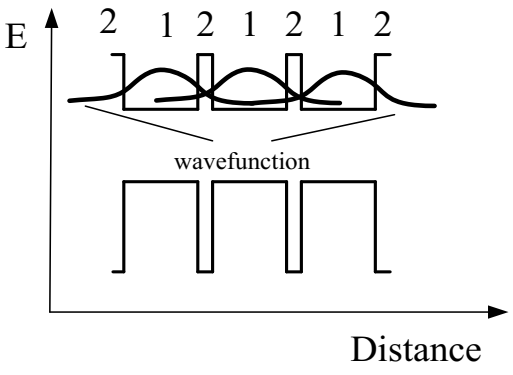

(b)

Fig. 10 Schematic of the wave functions in of (a) a MQW structure and (b) a SL structure.

If the layer structure for the SQW is repeated, MQW or superlattice (SL) can be formed. The difference between the MQW and the SL is the extent of the interaction between the quantum wells, as shown in Fig. 10. For the ideal MQW structure, there is no overlapping of the wave function φ of the electrons in two adjacent quantum wells. Thus, the MQW exhibits the properties of a collection of isolated single quantum wells. However, in the SL structure, there is a significant wave function φ penetration between quantum wells. Usually, the barrier width of quantum well structure is much larger than that of the supperlattice structure to prevent the interaction between quantum wells. In following sections of this thesis, we will just talk about the MQW structure.

A. Sub-band in MQW

Since the physics of the MQW structure is essentially the same as a set of independent wells, we can analyze the physics of SQW instead for simplification. Fig. 11 shows the schematic diagrams for a bulk structure and a MQW structure. In the bulk material (D_x, D_y, D_z >>0.1μm), the electrons and holes are free to move in all the directions (x, y, z direction). Both the distribution function of the energy of states and the density of states are continuous. But in the quantum well structure, the thickness of the well D_w is comparable to the Broglie wavelength of the electrons and holes (about tens of nanometer). Thus, the electrons and holes are

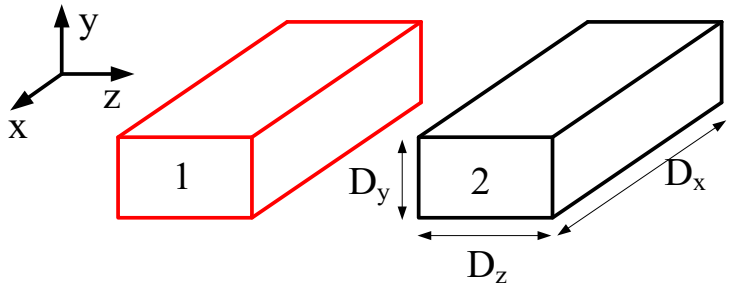

(a)

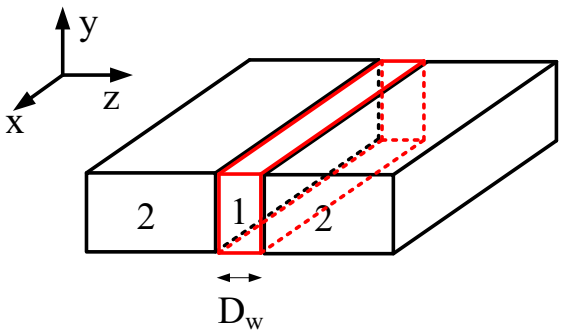

(b)

Fig. 11 (a) The bulk structure, material 1 and material 2; (b) the SQW structure, material 1 as the well and material 2 as the barrier

confined in the direction perpendicular to the layers (*z* direction in Fig. 11). The motion energy of states in *z* direction (confined-state energy) becomes quantized, which can be discrete values of E_1, E_2, E_3 …. In the directions parallel to the layers (*x* and *y* direction), the electrons and holes do not have the confinement. The distribution of in-plane motion energy is still continuous. We call this kind of system "2-dimentional electron gas".

The envelope wave function and the energy of particles (electrons, heavy holes or light holes) in quantum wells satisfy the time-independent Schrödinger equation as shown in Eq. (14). If we set Eq. (10) in to Eq. (14), the Schrödinger equation would be as follows

$$\begin{cases} -\frac{\hbar^2}{2m^*(z)}\left(\frac{\partial^2}{\partial x^2}+\frac{\partial^2}{\partial y^2}+\frac{\partial^2}{\partial z^2}\right)\varphi_e + \mathrm{U}_e(\mathrm{z})\varphi_e = \mathrm{E}_e\varphi_e \; for\; electrons \\ -\frac{\hbar^2}{2m^*(z)}\left(\frac{\partial^2}{\partial x^2}+\frac{\partial^2}{\partial y^2}+\frac{\partial^2}{\partial z^2}\right)\varphi_h - \mathrm{U}_h(\mathrm{z})\varphi_h = \mathrm{E}_h\varphi_h \; for\; holes \end{cases}. \quad (16)$$

As the potential energy *U* can be written as *U=U(x,y,z)=U(z)* since there is no energy discontinuity in *x* and *y* direction. The wave function φ can be expressed as

$$\varphi(\mathrm{x},\mathrm{y},\mathrm{z}) = \varphi_x(x)\varphi_y(y)\varphi_z(z). \quad (17)$$

The wave function, which describes the behavior of the particles in *xy* directions, should be the function of plane wave which is the same as in the bulk materials

$$\varphi_x(x) = Ae^{jk_x x}, \varphi_y(y) = Be^{jk_y y} \quad (18)$$

where $\boldsymbol{k_t}=k_x\boldsymbol{e_x}+k_y\boldsymbol{e_y}$ is the vector parallel to the layers. After substituting Eq. (17) and Eq. (18) into Eq. (16), we get

$$\frac{\hbar^2}{2m^*(z)}\left(k_x^2+k_y^2\right)\varphi(\mathrm{x},\mathrm{y}) = E_t\varphi(x,y), \quad (19)$$

$$\begin{cases} -\frac{\hbar^2}{2m^*(z)}\frac{\partial^2}{\partial z^2}\varphi_e(\mathrm{z}) + \mathrm{U}_e(\mathrm{z})\varphi_e(\mathrm{z}) = \mathrm{E}_{z,e}\varphi_e(z) \; for\; electrons \\ -\frac{\hbar^2}{2m^*(z)}\frac{\partial^2}{\partial z^2}\varphi_h(\mathrm{z}) - \mathrm{U}_h(\mathrm{z})\varphi_h(\mathrm{z}) = \mathrm{E}_{z,h}\varphi_h(z) \; for\; holes \end{cases} \quad (20)$$

where E_t and E_z stands for the eigenenergy in plane and in *z* direction, respectively. Solving Eq. (19), the in-plane eigenenergy can be gotten

$$E_t = \frac{\hbar^2}{2m^*(z)}\left(k_x^2+k_y^2\right) = \frac{\hbar^2}{2m^*(z)}k_t^2. \quad (21)$$

The dispersion curve for the particle in-plane is the same as in Fig. 5. The in plane eigenenergy E_t is continuous. However, solutions of Schrödinger equation in *z* direction (Eq. (20)) produce discrete states of energy $E_z|_{i^{th}\,energy\,state} = E_i$. Summarizing, the total energy of a particle in quantum well system is given by

$$E = E_z + E_t = E_i + \frac{\hbar^2}{2m^*(z)} k_t^2, i = 1, 2, 3, ... \quad (22)$$

where E can be E_e for the energy of electrons and E_h for energy of holes, i is the quantum number of the discrete states which is i_e for electrons, i_{hh} for heavy holes, and i_{lh} for light holes. The dispersion curve for a particle (electron, heavy hole, or light hole) in a quantum well is shown in Fig. 12. In the plane of the quantum well, there is a continuous range of allowed energies. In bulk materials, such domains are called "energy bands". But in quantum wells, we have instead "subbands" that are associated with confined levels. The particle (electron or hole) in a given

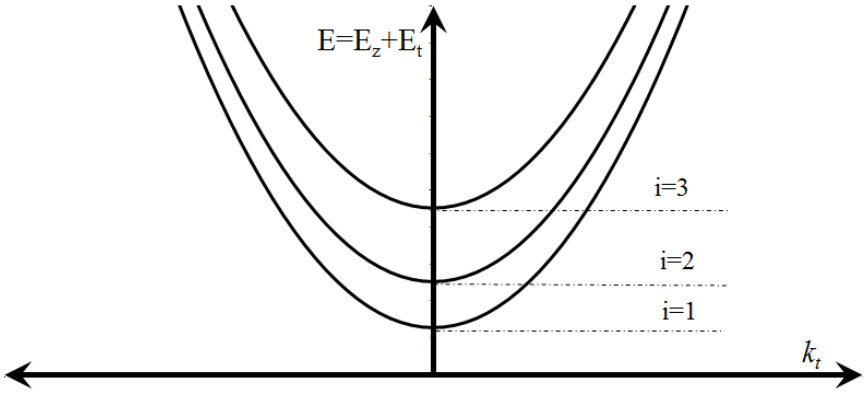

Fig. 12 Schematic showing the in-plane (k_t) dispersion curve and the subband structure.

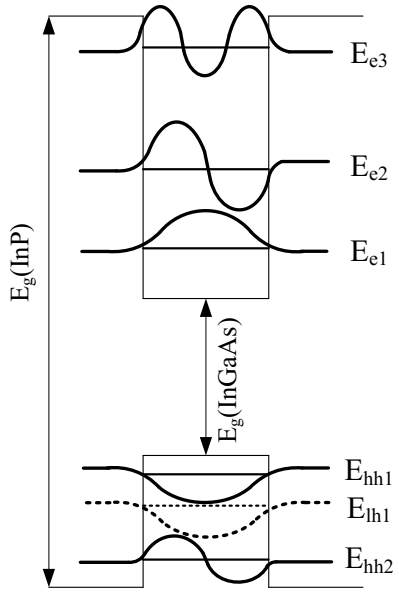

Fig. 13 Eigenenergies E_n and wave functions $\varphi(z)$ in a InGaAs/InP single quantum well (E_e: electrons, E_{hh}: heavy holes, E_{lh}: light holes).

confined state can have any energy equal or larger than the confined state energy (E_1, E_2, … E_i) in the subbands.

To analyze the dependence of the discrete eigenenergies E_i on the geometry and material of the quantum well, we use the simplest case-"infinite well". It is assumed that the barriers of the quantum well are infinitely high. Then the wave function must be zero at the walls of the quantum well. Based on the particle-in-a-box model, the solution of Eq. (20) is obtained as

$$E_i = \frac{\hbar^2}{2m^*}\left(\frac{i\pi}{D_w}\right)^2 \; i = 1,2,\ldots. \qquad \varphi_n = Asin\left(\frac{\pi z i}{D_w}\right) \tag{23}$$

where D_w is the thickness of well. From Eq. (23), the eigenenergies depend on the effective mass and the well thickness D_w. Narrow wells and small effective masses enlarge the eigenenergies. The interval between the eigenenergies becomes large at high levels i. Only in narrow wells, the discrete energy levels are remarkable. Of course, in reality, the barrier height cannot be infinite. The finite barrier height depends on the band gap discontinuity ΔE_c for electrons, ΔE_v for heavy holes, and light holes. The solutions will be more complex, which will be discussed in Chapter 3.

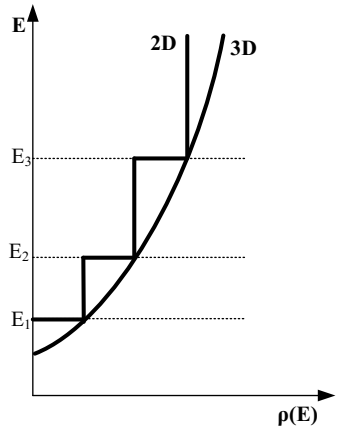

Fig. 14 Diagram of two dimensional (2D) density of states function for each subband and the three dimensional density of states function.

Eq. (20) accounts for the electron, the heavy hole, and the light hole in the quantum well. Using the effective mass of the electron m_e^*, the heavy hole m_{hh}^*, and the light hole m_{lh}^* together with the band-discontinuity caused one-dimensional potential energy $U(z)$ of the electron, the heavy hole, and the light hole in Eq. (20), the eigenenergies E_i and the wave functions $\varphi(z)$ can be obtained. An example of eigenenergies E_i and wave functions $\varphi(z)$ in the InGaAs/InP quantum well structure is shown in Fig. 13. According to Eq. (23), the eigenenergy is inverse proportional of the effective mass. Since the effective mass

of the light hole is smaller than that of the heavy hole, the eigenenergy of the light hole $E_{lh,i}$ is larger than the eigenenergy of the heavy hole $E_{hh,i}$. Thus, in quantum wells the valence bands for the heavy hole and the light hole are not degenerated anymore and separated.

The distribution of density of states in 3-dimentional (3D) bulk material is parabolic as shown in Fig. 14. According to Eq. (22), the in-plane energy contour surface is a circle. The number of states within dE_t per unit area is [23]

$$D(E_t)dE_t = \frac{k_t dk_t}{\pi} \tag{24}$$

Using Eq. (23), the states per unit area and per unit energy is obtained

$$D(E_t) = \frac{m^*}{\pi\hbar^2}. \tag{25}$$

The density of states which is the number of states per unit volume and per unit energy is

$$\rho(E) = m^*/\pi\hbar^2 D_w. \tag{26}$$

According Eq. (26), the two dimensional (2D) density of states is constant with energy, which is only relative to the effective mass and the well thickness. After summing all the density of states in the allowed energy subband, the density of states for a given subband is a "step" that starts at the corresponding eigenenergy. Fig. 14 indicates the correlation between the overall 2D (quantum well) and the 3D (bulk) density of states functions.

B. Exciton

Since the free electrons in the conduction band and the free holes in the valence band are negative and positive charged particles, they can attract each other by Coulomb attraction. Their motions are not independent any more. The attractive potential leads to a reduction (E_b) in the energy of the electron and hole. This bond state of an electron and a hole is called as an exciton. It is an electrically neutral quasiparticle existing in insulators, semiconductors, and some liquids. The exciton is regarded as an elementary excitation of condensed matter that can transport energy without electric charge [25].

There are normally two ways to generate excitons as shown in Fig. 15. By absorbing a photon of an energy equal or larger than the discrete energy difference between holes and electrons, a free electron is created and an empty state (hole) is left within the valence band ("high energy excitation"). The hole often forms a bond with an electron in the conduction band. Thus, an exciton is formed ("exciton formation" in Fig. 15). The second way is that if the photons of energy just below the band gap can also be absorbed to create excitons directly ("resonant excitation" in Fig. 15) [23].

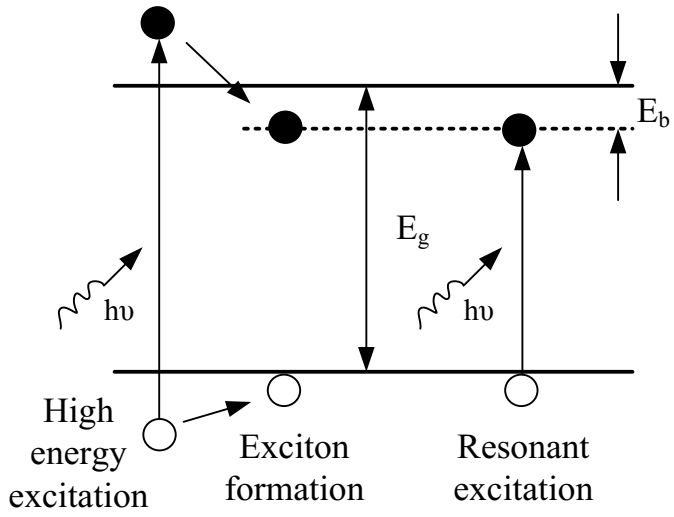

Fig. 15 Schematic representation of the generation of excitons.

The model of a hydrogen atom can be used to analyze the properties of excitons. In bulk material, the binding energy E_b^{3D} of an exciton can be obtained as [23]

$$E_b^{3D} = \frac{\mu e^4}{32\pi^2 \hbar^2 \epsilon_r^2 \epsilon_0^2} \tag{27}$$

where ε_r is the relative permittivity and ε_0 is the permittivity of free space. μ is the reduced mass which is given by

$$\frac{1}{\mu} = \frac{1}{m_e^*} + \frac{1}{m_h^*} \tag{28}$$

where m_e^* is the effective mass of the electron. m_h^* is m_{hh}^* for the effective mass of the heavy hole, and m_{lh}^* for the effective mass of the light hole. And the Bohr radius which is used to express the most probable distance between the proton and the electron of hydrogen becomes

$$\lambda_{ex}^{3D} = \frac{4\pi\epsilon_r\epsilon_0\hbar^2}{\mu e^2}. \tag{29}$$

The total energy of the exciton in bulk materials can be obtained

$$E_{ex} = E_g - E_b^{3D}. \tag{30}$$

Fig. 16 shows an exciton in a bulk material and an exciton in a quantum well structure [4]. The excitons in a quantum well are different from that in a bulk material, due to the strong confinement in a quantum well. Since the size of the exciton in a bulk material is normally larger than the well thickness, the exciton in a quantum well must become much smaller in the direction perpendicular to the quantum wells (z direction in Fig. 15). There are two limiting cases for the

analysis of excitons in a quantum well. In the case of a large well thickness (two orders of magnitude larger than the de Broglie wavelength $\lambda = {}^{h}/_{p}$, where $p = |\boldsymbol{p}|$), the exciton should be like an exciton in bulk. In the case of a narrow well (comparable to the de Broglie wavelength $\lambda = {}^{h}/_{p}$), the exciton will become 2D. Using the model of 2D hydrogen atom, the binding energy and Bohr radius of 2D exciton can be obtained

$$E_b^{2D} = \frac{\mu e^4}{8\pi^2 \hbar^2 \epsilon_r^2 \epsilon_0^2} = 4E_b^{3D}, \tag{31}$$

$$\lambda_{ex}^{2D} = \frac{2\pi\epsilon_r\epsilon_0\hbar^2}{\mu e^2} = \lambda_{ex}^{3D}/2. \tag{32}$$

From Eq. (31) and Eq. (32), the binding energy of a 2D system is four times larger than that of a 3D system. And the Bohr radius of the 2D system is half of that of the 3D system. Since the excitons in a quantum well cannot achieve any of both limiting cases, the binding energy of an exciton in a quantum well E_b and the Bohr radius in a quantum well λ_{ex} obey

$$\lim_{D_w \to \infty} E_b = E_b^{3D} \ \ and \ \ \lim_{D_w \to 0} E_b = E_b^{2D}, E_b^{3D} < E_b < E_b^{2D}, \tag{33}$$

$$\lim_{D_w \to \infty} \lambda_{ex} = \lambda_{ex}^{3D} \ \ and \ \ \lim_{D_w \to 0} \lambda_{ex} = \lambda_{ex}^{2D}, \lambda_{ex}^{2D} < \lambda_{ex} < \lambda_{ex}^{3D}. \tag{34}$$

The accurate calculation of the exciton binding energy and the Bohr radius for certain quantum well geometries is more complex, and will be discussed in Chapter 3. Since the electron and hole are closer together in a quantum well than in bulk material, the absorption strength to create such excitons should be larger.

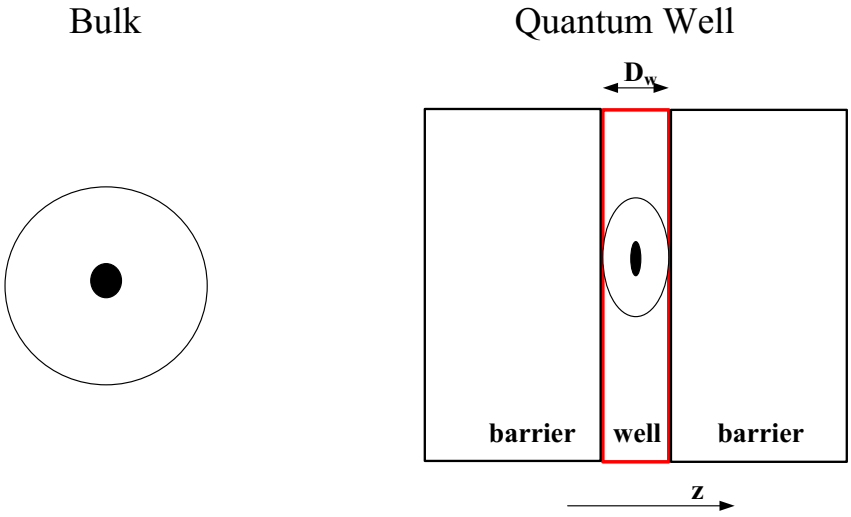

Fig. 16 Comparison of exciton size and shapes in bulk and quantum well.

From Eq. 29, the exciton in a quantum well has larger binding energies than that in bulk material. Because of the larger binding energy, the exciton cannot be easily destroyed by optical phonons or ionized by an electrical field. The electron and hole are closer together than in the 3D case, so that the absorption strength to create such an exciton is larger. Normally, the quantum well excitons can be easily resolved at room temperature, but the bulk excitons can be resolved only at low temperature. Thus, the exciton is one of the most important phenomena in quantum wells.

C. Strain in quantum well

In the previous sections, the lattice constants of the well and the barrier materials are the same. The fast development of epitaxial growth technology has opened up the possibility of growing heterostructures in which a mismatch of the lattice constant of the adjacent materials exist. In quantum wells, this lattice mismatch is accommodated via an elastic strain, modifying the electronic properties of the quantum well structures. The effects of strain are of particular interest in quantum well structures.

A thin epitaxial layer with the lattice constant of a_e is deposited on a thick substrate with the lattice constant of a_s. If a_e equals to a_s, it is the lattice match situation. But if a_e is different from a_s, the epitaxial layer will be well deposited without defects or dislocations only when the epitaxial layer is thin enough that the stress produced by the lattice constant mismatch can be balanced through the elastic strain of the epitaxial layer. In that case, the lattice constant a_e of the epitaxial layer will be forced to be equal to the lattice constant a_s of the substrate. Thus, the epitaxial layer suffers biaxial stress along the growth interface (x, y direction in Fig. 16) and no stress along the growth direction (z direction). The crystal is able to relax freely along that direction [23]. The stress in the quantum well can be written as

$$\sigma = \begin{pmatrix} \sigma_1 & 0 & 0 \\ 0 & \sigma_2 & 0 \\ 0 & 0 & 0 \end{pmatrix}. \tag{35}$$

The stress has only two diagonal components σ_1 and σ_2 along the growth interface, while σ_3 along growth direction equals zero.

The lattice mismatch can be schematically illustrated in Fig. 17. For material A, the lattice constant a_e is smaller than the lattice constant of the substrate a_s. The tensile strain forces the in-plane (x, y direction) lattice constant $a_{//}$ to increase to be same as the lattice constant of the substrate a_s, while the lattice constant in the growth direction (z direction) $a_{\perp}$ will decrease due to compressive strain. For material B, the lattice constant a_e is larger than the lattice constant of the substrate a_s. The compressive strain forces the in-plane (x, y direction) lattice constant $a_{//}$ to

decrease to be same as the lattice constant of the substrate a_s, while the lattice constant in the growth direction (z direction) $a_\perp$ will increase due to tensile strain. The strain can be calculated

$$\epsilon_{//} = \epsilon_{xx} = \epsilon_{yy} = \frac{a_{//} - a_e}{a_e} = \frac{a_s - a_e}{a_e}, \tag{36}$$

$$\epsilon_\perp = \epsilon_{zz} = \frac{a_\perp - a_e}{a_e} = -2G\epsilon_{//} \approx -\epsilon_{//} \tag{37}$$

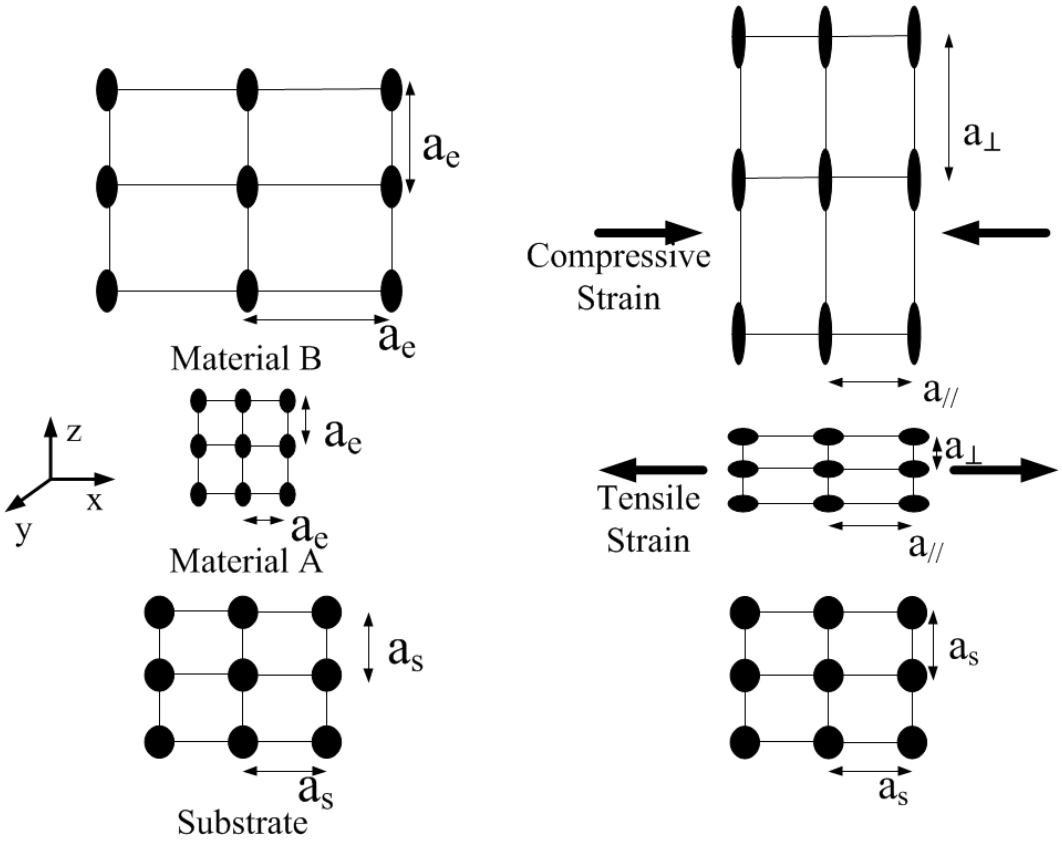

(a) (b)

Fig. 17 Schematic illustration of a substrate with two mismatched layers (Material A and Material B). (a) free-standing unstrained materials, Material A with smaller lattice constant $a_e<a_s$, Material B with larger lattice constant $a_e>a_s$; (b) the compressive strain (Material B grows on the substrate), and the tensile strain (Material A grows on the substrate).

where G are elastic stiffness factor which is about 0.5 [26]. From Eq. (36), $\epsilon_{//}<0$ stands for a compressive strain and $\epsilon_{//}>0$ stands for a tensile strain. It is worth mentioning that the strain we always discuss refers to the in-plane strain.

For strained epitaxial layers, a certain amount of elastic strain can be accommodated by any material without generating dislocations or defects. But if the thickness of the epitaxial layer is large enough (larger than the critical

thickness h_c) so that the elastic strain energy lies above the energy of dislocation formation, dislocations and defects are generated to relieve the high lattice mismatch strain which destroys the epitaxial layer. There are two models for the critical thickness h_c. Matthews used the mechanical equilibrium model to calculate the critical thickness h_c [26] [27]

$$h_c = \frac{b}{4\pi|\epsilon_{//}|(1+\dot{v})}\left[\ln\left(\frac{h_c}{b}\right)+1\right] \tag{38}$$

where $b = \frac{a_s}{\sqrt{2}}$, $\dot{v}$ represents in-plane Poisson's ratio for cubic semiconductor ($\dot{v} \approx 0.3$), and a_s is the lattice constant of the substrate. The unit of the obtained critical thickness is the same as the unit of a_s. For example, the critical thickness is calculated as 110nm by growing a material with a compressive strain of -0.12% on an InP substrate.

The strain in a bulk epitaxial layer induces the modification of the band structures. The compressive strain and the tensile strain have different effects on the shift of energy levels, as shown in Fig. 18. The compressive strain, caused by the material with a larger lattice constant, shifts the conductive band bottom up and the valence band bottom down, which increases the band gap. The heavy hole and the light hole are separated from each other. The valence band bottom of the heavy hole lies above that of the light hole. On the contrary, the tensile strain, induced by the material with a smaller lattice constant, shifts the conductive band bottom down and the valence band bottom up, which decreases the band gap. The valence band bottom of the heavy hole lies under that of the light hole.

These phenomena can be expressed as follows. Since the larger lattice constant brings the larger distance between the atoms, the outermost electrons have weaker

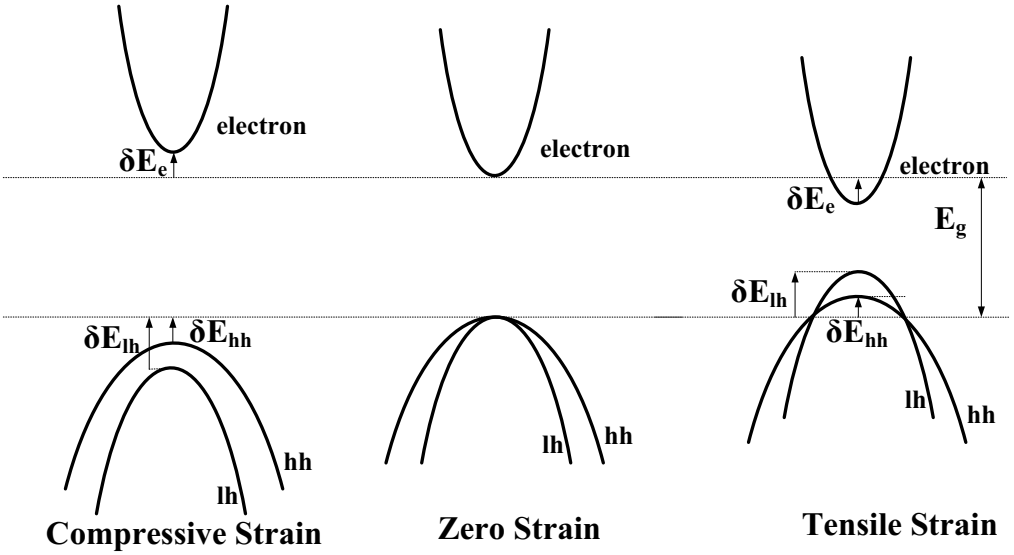

Fig. 18 The effects of different strains on the band structure

periodic potential field, which decreases the bandgap of the material. It means that the bandgap is inversely proportional to the lattice constant. The compressive strain forces the in-plane lattice constant to decrease to be equal to the lattice constant of the substrate. With the reduced lattice constant, the distance between the outermost electron and the nucleus becomes smaller which enhances the periodic potential field. The larger periodic potential field shifts the conduction band up and the valence band down, increasing the bandgap of material. The carrier band shift is inversely proportional to the carrier mass. Since the mass of the heavy hole is much larger than the mass of the light hole, the band shift of the heavy hole δE_{hh} is smaller than the band shift of the light hole δE_{lh}. As a result, the bottom of the heavy hole energy band lies above that of the light hole. The same theory can also be used for the tensile strain. Thus, the band gap considering the energy band shift induced by the strains is expressed

$$E_{\mathrm{g,ehh}} = E_g + \delta E_e - \delta E_{hh}, \tag{39}$$

$$E_{\mathrm{g,elh}} = E_g + \delta E_e - \delta E_{lh} \tag{40}$$

where $E_{g,ehh}$ and $E_{g,elh}$ stand for the band gap of the electron-heavy-hole pair and the electron-light-hole pair, respectively.

2.3 Optical properties in MQWs

In MQW structures, the optical absorption can be considered as two individual kinds of absorptions: the optical absorption of the band-to-band continuum transition (continuum absorption) and the optical absorption of the exciton resonance (excitonic absorption) [28]. This section will talk about these two optical absorptions and their dependence on the electrical field and the input light polarization.

2.3.1 Continuum absorption in MQWs

In semiconductor materials, the valence band electron can be seen as part of a molecular bond. Only if the molecular bond is broken, the electron can be free to move in the crystal lattice of the semiconductor. And then the electron is in the conduction band. The energy required to break the covalent bond is the energy distance between the valence band and conduction band (at least the band gap E_g). Thus, only the photons with the energy greater than the semiconductor band gap E_g can be absorbed to create an electron in the conduction band and a hole in the valence band. The photons with the energy lower than the semiconductor band gap will not be absorbed and will pass through the semiconductor (transparent).

In order to understand the optical absorption of band-to-band continuum transition, electron-photon interactions in the crystal need to be characterized. In quantum

mechanics books [24] [29], the total transition rate from the valence band state with a wave function of φ_h to a particular conduction band state with a wave function of φ_e is given

$$W_{v\to c} = \frac{2\pi}{\hbar}|H'_{eh}|^2 \rho_{red} f_v(1-f_c) \tag{41}$$

where ρ_{red} is the reduced density of states which can be obtained as

$$\rho_{red} = \frac{1}{2}\left(\frac{1}{\rho_c}+\frac{1}{\rho_v}\right)^{-1} \tag{42}$$

where ρ_c and ρ_v are the distribution function of the density of states in the conduction band and in the valence band, respectively, as shown in Fig. 14 (ρ^{2D} for quantum well structures, and ρ^{3D} for bulk materials). f_v represents the probability of the valence band state being occupied, and *1-*f_c stands for the probability of the conduction band state being unoccupied. According to the Fermi-Dirac distribution [29], the electron occupation probability f_v and f_c is defined as

$$f_{c,v} = \frac{1}{1+\exp[(E_{e,h}-E_{fc,fv})/k_B T]} \tag{43}$$

where $E_{e,h}$ is the individual energy for electrons and holes, respectively, $E_{fc,fv}$ are the nonequilibrium quasi-Fermi levels in the conduction bands and valence bands [30], respectively, k_B is Boltzmann's constant, and T is the temperature of the crystal. $|H'_{eh}|^2$ can be obtained as follows

$$H'_{eh} = \int_v \varphi_h^* H'(r)\varphi_e d^3r = <\varphi_h|H'(\boldsymbol{r})|\varphi_e>, \tag{44}$$

where $H'(\boldsymbol{r})$ stands for the time-dependent perturbation to the original Hamitonian considering the electron-photon interaction, which can be obtained

$$H'(\boldsymbol{r}) = \frac{e}{2m}A(\boldsymbol{r})\hat{\boldsymbol{e}}\cdot\boldsymbol{p}, \tag{45}$$

where $A(\boldsymbol{r})$ is the potential of the photon [1], $\hat{\boldsymbol{e}}$ is the unit polarization vector in the direction of $A(\boldsymbol{r})$, and $\boldsymbol{p}$ is momentum vector of the electron.

For a bulk material, the plane waves in Eq. (13) can be used in the wave function overlap integral in Eq. (44). By absorbing a photon, the electron in the valence band can only be raised to a state with the same momentum in the conduction band (valence band to conduction band transition) based on the momentum-conservation rule. As the energy of the photons increases above E_g, more and more electrons from the valence band can make the valence band to conduction band transition. The absorption coefficient increases with the energy of the

photons. Thus, the optical absorption spectrum as shown in Fig. 19 has a form that directly follows the density of states as shown in Fig. 14.

In quantum wells the wave functions of the electron and hole are cosine-like (symmetric) or sine-like (antisymmetric) functions as shown in Fig. 13. Since there is always orthogonality between symmetric and antisymmetric function, the overlap integral is nearly zero between the wave function of the electrons and the holes with different quantum number i, i_{hh}, and i_{lh}. Thus, only the transitions between the states with the same quantum number in valence and conduction bands are allowed [28]. Since the density of states in MQW structure is a step-form as shown in Fig. 14, the optical continuum absorption in MQWs is also a step-form as shown in Fig. 19. Each step starts at the energy of the energy difference between the sub-bands of the same quantum number in valence band and conduction band.

In quantum wells, the well dimensions are much smaller than the light wavelength. Thus, the potential of the photon can be considered as a constant A_0 in the wells. According to [1], Eq. (44) can be written as

$$|H'_{eh}|^2 = (\frac{eA_0}{2m})^2 |M_T|^2, \tag{46}$$

where $|M_T|^2$ is defined as the transition matrix element which is obtained as

$$|M_T|^2 = |< u_h|\hat{\boldsymbol{e}} \cdot \boldsymbol{p}|u_e >|^2 |< F_h \, | F_e >|^2. \tag{47}$$

where u_e and u_h are the Bloch function for electrons and holes, respectively, and F_e and F_h is the envelope function for electrons and holes, respectively, according to the wave function expression in Eq. (13).

The transition matrix element depends strongly on the angle between the wave vector $\boldsymbol{k}$ (the same direction with the momentum $\boldsymbol{p}$) and the electric unit vector $\hat{\boldsymbol{e}}$ of the light. For bulk material, the transition matrix element has the same value for

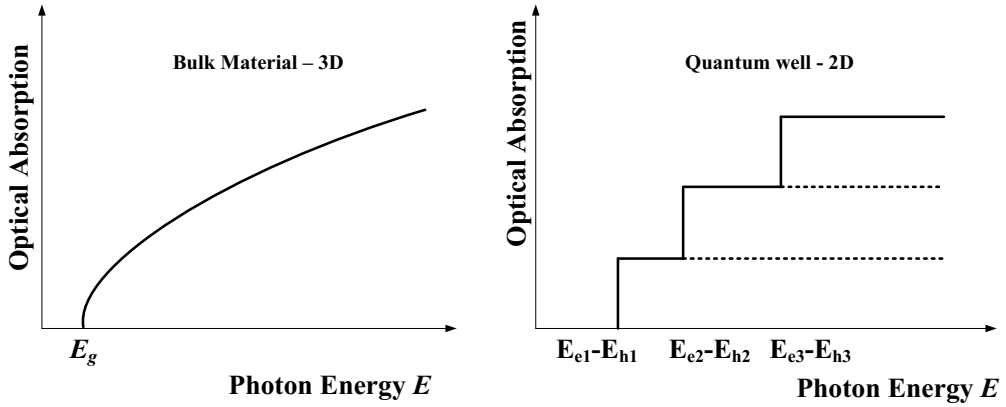

(a) (b)

Fig. 19 Optical continuum absorption in (a) a bulk material and (b) a quantum well.

the light polarized along *x*, *y* or *z*, since the crystal in bulk is symmetric. Thus, the transition matrix element in bulk material is isotropic. As mentioned above, the heavy hole and light hole valence bands are separated in quantum well structures. The separation of the heavy hole and the light hole band indicates the change of the crystal symmetry which leads to the anisotropic transition matrix element M_T. In quantum well structures, the consequence for optical absorption can be understood as two sets of absorption: the heavy-hole-to-electron (hh-e) set and the light-hole-to-electron (lh-e) set.

To get the transition matrix element, the conduction band Bloch function u_e and valence band Bloch functions u_{hh}, u_{lh} for heavy hole and light hole, respectively, should be analyzed. Assuming that the electron's wave vector $\boldsymbol{k}$ is along *z*, the valence band Bloch functions can be written as [1]

$$\begin{cases} u_{hh} = -\frac{1}{\sqrt{2}}(u_x + iu_y), \bar{u}_{hh} = \frac{1}{\sqrt{2}}(\bar{u}_x - i\bar{u}_y) \\ u_{lh} = -\frac{1}{\sqrt{6}}(\bar{u}_x + i\bar{u}_y - 2u_z), \bar{u}_{lh} = \frac{1}{\sqrt{6}}(u_x - iu_y + 2\bar{u}_z) \end{cases}, \tag{48}$$

where u_x, u_y, u_z are the basis Bloch functions for atomic orbitals, u and $\bar{u}$ indicate spin-up and spin-down functions. The transition probability between the electron Bloch function u_e and the basic functions (u_x, u_y, u_z) can be obtained by [28]

$$|M|^2 = \frac{m_0^2 E_g(E_g + \Delta)}{12 m_e(E_g + \frac{2}{3}\Delta)} \tag{49}$$

where m_e is the electron effective mass and Δ is the spin orbit splitting energy of the valence bands. By expanding the u_h in Eq. (53) in terms of u_x, u_y, and u_z using Eq. (48), the transition probability $|M_T|^2$ between u_e and the valence band Bloch functions u_{hh}, u_{lh} can be expressed in terms of $|M|^2$

$$|M_T|^2 = |M|^2 \cdot |< F_h \,|F_e >|^2 \cdot \begin{cases} 1 - \left|\hat{\boldsymbol{e}} \cdot \hat{\boldsymbol{k}}\right|^2 & for\ hh - e \\ \frac{1}{3} + \left|\hat{\boldsymbol{e}} \cdot \hat{\boldsymbol{k}}\right|^2 & for\ lh - e \end{cases} \tag{50}$$

where $\hat{\boldsymbol{k}}$ is a unit vector of electron vector $\boldsymbol{k}$. For bulk material, the vectors $\boldsymbol{k}$ point in all the directions. However, in quantum wells the $\boldsymbol{k}$ vectors are quantized along z direction (assuming that the growth direction along *z*) and point along the same axis *z*. Thus, the unit vector $\hat{\boldsymbol{k}}$ of $\boldsymbol{k}$ can be written as

$$\hat{\boldsymbol{k}} = \begin{cases} \frac{1}{\sqrt{3}}(\boldsymbol{e}_x + \boldsymbol{e}_y + \boldsymbol{e}_z) & for\ Bulk \\ \boldsymbol{e}_z & for\ quantum\ well. \end{cases} \tag{51}$$

For bulk material, $|M_T|^2 = \frac{2}{3} \cdot |M|^2 \cdot |< F_h \,|F_e >|^2$ is for any input light polarization. For quantum well structures, with a light propagation perpendicular

to the quantum well layers, the electric unit vector $\hat{\boldsymbol{e}}$ of the input light is always in the plane of the quantum wells. Thus for the light propagation perpendicular to the quantum well layers, $|M_T|^2$ is constant which can be obtained as

$$|M_T|^2 = |M|^2 \begin{cases} 1 \ |< F_{hh} \ |F_e >|^2 & for\ hh-e \\ \frac{1}{3} \ |< F_{lh} \ |F_e >|^2 & for\ lh-e. \end{cases} \tag{52}$$

If the light propagates along the quantum well layers, the situation is changed. $|M_T|^2$ depends strongly on the optical polarization direction. There are two distinct optical polarization directions. One is transverse electric (TE) polarization, whose electric field is perpendicular to the plane of incidence (parallel to the quantum layers). The other is called as transverse magnetic (TM) polarization. The electrical field of TM polarized light is in the plane of the incidence (perpendicular to the quantum well layers). The situation for TE polarized input light is the same as that for the light propagating perpendicular to the quantum well layers. $|M_T|^2$ can be obtained according to Eq. (52) with $\left|\hat{\boldsymbol{e}} \cdot \hat{\boldsymbol{k}}\right|^2 = 0$. However, the TM case is quite different, since $\left|\hat{\boldsymbol{e}} \cdot \hat{\boldsymbol{k}}\right|^2 = 1$. The transition matrix element for TE and TM polarizations of the optical field is further obtained as

$$|M_T|^2 = |M|^2 \begin{cases} 1 \ |< F_{hh} \ |F_e >|^2 + \frac{1}{3} \ |< F_{lh} \ |F_e >|^2 & for\ TE \\ \frac{4}{3} \ |< F_{lh} \ |F_e >|^2 & for\ TM. \end{cases} \tag{53}$$

From Eq. (53), it is clear that for a TM polarized light, the hh-e transitions are forbidden and only the lh-e transitions contribute to the light absorption. For a TE polarized light, both the hh-e and lh-e transition take place. The absorption associated with heavy holes is three times larger than that with light holes.

Thus, the absorption coefficient of the band-to-band transition can be further obtained as [28]

$$\alpha_{con} = \sum_{i,i_h} \frac{\mu e^2 |M_T|^2_{i_e,i_h}}{\varepsilon_0 c n m_0^2 \hbar^2 \omega D_w} \int_{E_{g,e-h}(i_e,i_h)}^{\infty} S_f(E, E_{g,e-h}(i_e,i_h)) L(E, \hbar\omega) dE \tag{54}$$

Where c is the light velocity in vacuum, n is the refractive index of the well, D_w is the well width, $E_{g,e\text{-}h}$ represents the energy band gap between the confined states of conduction band and the confined states of valence band, and i_e, i_h stand for the quantum number of the conduction band and valence band, respectively. $S_f(E, E_{g,e-h}(i_e,i_h))$ is the Sommerfeld factor [28], which can be expressed as

$$S_f\left(E, E_{g,e-h}(i_e,i_h)\right) = \frac{2}{1+\exp\left(-2\pi\sqrt{(E-E_{g,e-h}(i_e,i_h))/R_y}\right)} \tag{55}$$

where $R_y = {e^4\mu}/{(2\varepsilon_0^2\hbar^2)}$ is the Rydberg constant. $L(E,\hbar\omega)$ is the Lorentzian broadening function, which can be expressed as

$$L(E,\hbar\omega) = \frac{\Gamma}{\pi[(\hbar\omega - E)^2 + \Gamma^2]} \tag{56}$$

where Γ is the broadening width.

It is worth mentioning that the optical continuum absorption in a quantum well shown in Fig. 19 does not consider the absorption broadening effect.

2.3.2 Optical absorption due to excitons

The optical continuum band-to-band transition absorption spectra have a step form. The other optical absorption in MQWs is caused by exciton resonance. This absorption is called as the excitonic absorption. As mentioned above, an exciton consists of an electron and a hole interacting through Coulomb attraction. In quantum well layers, the excitons own a larger binding energy and a stronger oscillator strength than in bulk materials because the excitons are strongly compressed in the quantum well layers. Thus, the exciton optical absorption spectra are easier to be observed at room temperature.

The excitonic absorption creates excitons by absorbing the photons with the energy E_b less than that required to create a free electron-hole pair. The total optical absorption spectra around the absorption edge as shown in Fig. 20 have a step-like continuum band-to-band transition absorption and two excitonic absorption peaks. The peak at lower energy is caused by the electron-hh exciton

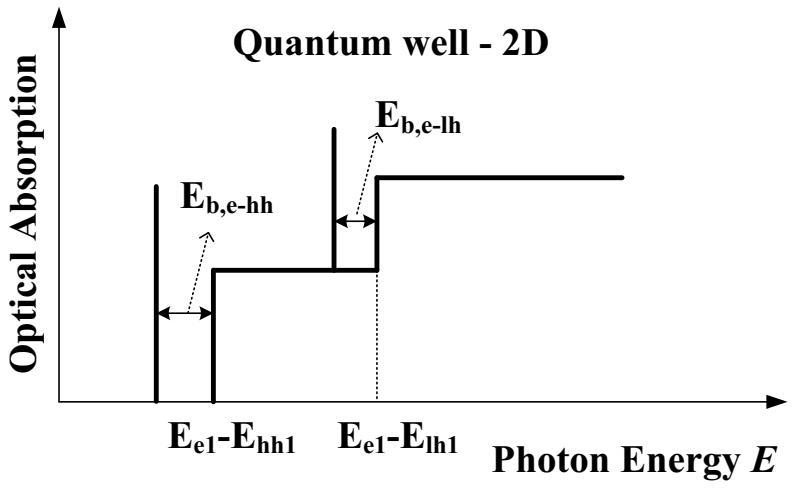

Fig. 20 Optical absorption in quantum wells: continuum band-to-band transition absorption and excitonic absorption.

with binding energy of $E_{b,e\text{-}hh}$ and the peak at larger energy is due to the optical absorption of electron-lh exciton with binding energy of $E_{b,e\text{-}lh}$.

We cannot use the above discussed single electrons and single holes model to analyze the excitonic effects. The exciton should be considered as a bounded electron-hole pair. The wave function of the excitons φ_{ex} in quantum wells can be obtained as [28] [31]

$$\varphi_{ex} = \frac{1}{\sqrt{S}} e^{j\boldsymbol{kR}} \varphi_e \varphi_h \phi_{ex}(\boldsymbol{r}) \tag{57}$$

where S is the area of quantum well, $\boldsymbol{R}$ is the in-plane center of mass of an electron and a hole, $\boldsymbol{k}$ is the wave vector, φ_e and φ_h are the wave function of an individual electron and hole, respectively, and $\phi_{ex}(\boldsymbol{r})$ denotes the relative in-plane motion of the electron-hole pair with their relative in-plane distance $\boldsymbol{r}$.

The relative in-plane motion of the electron-hole pair is obtained as

$$\phi_{ex}(\boldsymbol{r}) = \left(\frac{2}{\pi}\right)^{1/2} \frac{1}{\lambda_{ex}} e^{-\boldsymbol{r}/\lambda_{ex}} \tag{58}$$

where λ_{ex} is the Bohr radius of the exciton. The excitonic absorption in a quantum well can be calculated based on the time-dependent perturbation theory [28]

$$\alpha_{ex} = \sum_{i_e, i_h} Q(\dot{\imath_e}, \imath_h) L(E_{ex}(i_e, i_h), \hbar\omega) \, / D_w \tag{59}$$

where Q is the integrated intensity and $L(E_{ex}(i_e, i_h), \hbar\omega)$ is the Lorentzian broadening function. The exciton energy E_{ex} is given by

$$E_{ex} = E_{\mathrm{e}} - E_h - E_{b,e-h}. \tag{60}$$

According to Eq. (59), the excitonic absorption peak is proportional to the integrated intensity and to the inverse of the width of the broadening function. The

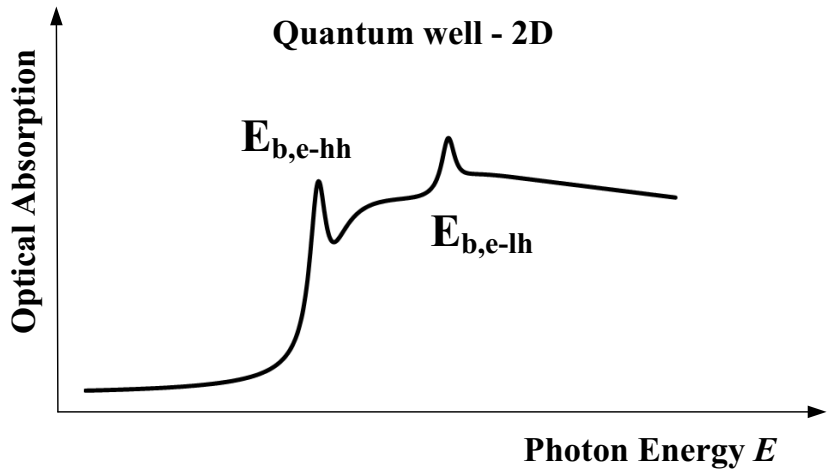

Fig. 21 Optical absorption in quantum wells considering the broadening effect.

integrated intensity describes the creation rate of excitons which depends on the wave function, binding energy of excitons in quantum wells, and the polarization of input light. The integrated intensity can be expressed as

$$Q(\dot{\iota_e}, \iota_h) = \frac{4e^2\hbar}{\varepsilon_0 cnm^2 E_{ex}(i_e, i)\lambda_{ex}^2(i_e, i_h)} |M_T|^2{}_{j_e, j_h} \tag{61}$$

where M_T is the transition matrix element which can be calculated using Eqs. (46), (52), and (53).

The Lorentzian broadening factor $L(E_{ex}, \hbar\omega)$ can be obtained [32]

$$L(E_{ex}, \hbar\omega) = \frac{\Gamma}{\pi((\hbar\omega - E_{ex})^2 + \Gamma^2)} \tag{62}$$

where Γ is the exciton spectrum width.

Fig. 21 shows the total optical absorption including continuum band-to-band transition absorption and excitonic absorption considering the broadening effect. The spectrum broadening depends strongly on many parameters such as the temperature, the electrical field, and the carrier density. The spatial inhomogeneity is the main spectrum broadening reason at low temperatures. The spatial inhomogeneity is caused by structural imperfections in the quantum wells [28] such as interface roughness and composition fluctuations of the constituent alloys. Excitons can be ionized to be free electrons and holes by phonon scattering. At high temperature, the density of the phonons in quantum wells increases and more excitons are ionized broadening the spectrum. The temperature dependent exciton spectrum width Γ can be obtained as the combination of inhomogeneous broadening width Γ_0 and the thermal broadening width $\Gamma_T(T)$

$$\Gamma = \Gamma_0 + \Gamma_T(T), \tag{63}$$

$$\Gamma_T(T) = \frac{\Gamma_{ph}}{\exp\left(\frac{\hbar\omega_{LO}}{k_B T}\right) - 1} \tag{64}$$

where $\hbar\omega_{LO}$ is the longitudinal optical (LO) phonon energy and Γ_{ph} is the parameter related to the exciton-phonon interaction [33]. Γ_0, $\hbar\omega_{LO}$, and Γ_{ph} are kept as free parameters in the model.

2.3.3 Influence of electrical field on optical absorption spectra

In this section, only the effects of electric fields perpendicular to the quantum well layers with intrinsic barriers and wells will be discussed. Fig. 22 shows the optical absorption spectra for electric fields applied perpendicular to the quantum well layers. It can be seen that the exciton absorption peaks are strongly shifted to longer wavelength by the field (red shift). This shift of the exciton absorption peaks with the applied electric field is called as the quantum-confined Stark effect

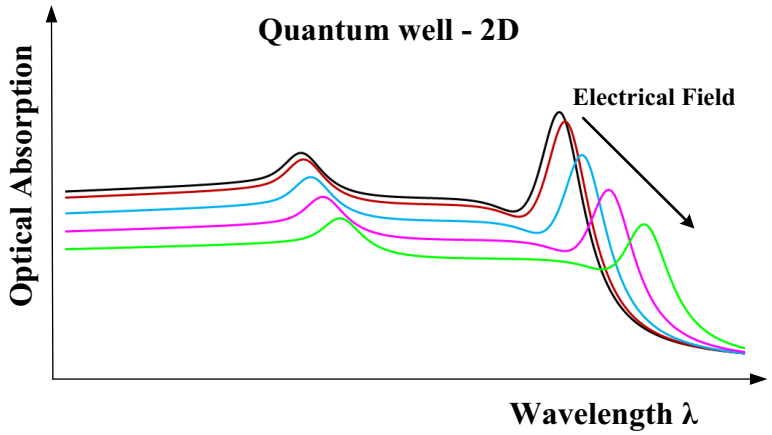

Fig. 22 Optical absorption in quantum wells for different electric field applied perpendicular to the quantum well layers.

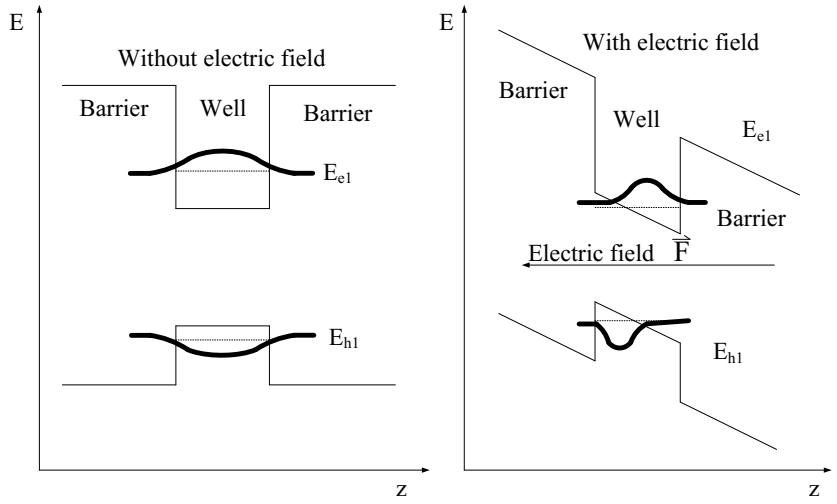

Fig. 23 Electron and hole wave functions of first state in quantum wells and band. (a) without electric field; (b) with external electric field perpendicular to the quantum well layer. The barriers and wells are undoped.

(QCSE). The excitonic absorption strength (the exciton absorption peak) decreases with the applied field [33]. And the exciton absorption peak is broadened by increasing the applied electric field strength. In the following part, the theory of the effects of electric field on the optical absorption spectra will be discussed.

Fig. 23 shows the influences of the electric field on the band structures and wave functions in quantum well layers. Without electric field, the wave functions of electron and hole are symmetric as shown in Fig. 23 (a). Applying an electric field perpendicular to the wells, the band structure starts to slant (Fig. 23 (b)). The discrete electron energy level move down and the discrete hole energy level move up, leading to a reduced energy separation between the discrete electron and hole energy levels. The reduced energy separation between the electron and hole

energy levels results in the red shift of the absorption peak. Moreover, the electrons and the holes are separated from one another by being pulled in the opposite directions with applied electric field. The symmetry of the wave functions of electron and hole are distorted. In this case, the overlap integrals between all possible states decrease, reducing the absorption strength. With the presence of the electrical field, the electrons and holes are pulled to opposite sides of the well, which causes the reduction in the Coulomb attraction of the electron and hole. This reduction in the Coulomb attraction of the electron and hole increases the linewidth of the exciton broadening the excitonic absorption.

The shifted sub-energy levels E_j of electron and holes and the distorted eigen wave functions φ_j caused by the applied electric field can be calculated by solving the Schrödinger equation by including electric field F.

$$\begin{cases} -\frac{\hbar^2}{2m^*(z)}\frac{\partial^2}{\partial z^2}\varphi_e(\mathrm{z}) + (\mathrm{U}_e(\mathrm{z}) + \mathrm{eFz})\varphi_e(\mathrm{z}) = E_{z,e}\varphi_e(z) \;\; for\ electrons \\ -\frac{\hbar^2}{2m^*(z)}\frac{\partial^2}{\partial z^2}\varphi_h(\mathrm{z}) - (\mathrm{U}_h(\mathrm{z}) + \mathrm{eFz})\varphi_h(\mathrm{z}) = E_{z,h}\varphi_h(z) \;\; for\ holes \end{cases} \tag{65}$$

where F is the electric field strength perpendicular to the quantum well layers.

In summary, compared to the bulk material, the quantum well structure has the following special properties of optical absorption. The separation of heavy-hole band and light-hole band in quantum wells results in the different optical absorption strength of TE and TM polarized light, which causes a large PDL. The strain can be introduced to tune the heavy-hole and light-hole band structure. By introducing compressive strain, the separation of heavy-hole and light-hole band becomes larger (the heavy-hole band lies above the light-hole band with larger distance) (Fig. 18) which leads to TE preferred optical absorption (large PDL). By introducing tensile strain, the light-hole band moves closer to the heavy-hole band. If these two bands are overlapped, there will be no polarization dependent optical absorption. By further increasing the tensile strain, the light-hole band will lie eventually above the heavy-hole band, which leads to TM preferred optical absorption.

Because of the strong confinement of the electrons and holes in wells, the excitons can be easily observed at room temperature in quantum wells while the excitons in bulk material are rapidly ionized in times short compared with a classical orbit time and become unresolvable. Thanks to the strong excitonic absorption, there are sets of peaks in the optical absorption spectra, leading to stronger optical absorption in quantum wells compared to the bulk materials.

In bulk materials, the optical absorption also depends on the electrical field strength. This phenomenon is called as Franz-Keldysh Effect (FKE). In MQWs, the QCSE causes the red shift of the optical absorption peaks with the electrical field. Moreover, for MQWs the applied electrical field broadens the absorption

spectra and reduces the absorption peak value. Therefore, optimal electric field strength should be set to get a maximum absorption coefficient at a certain wavelength of input light.

2.4 Physical effects in waveguide integrated MQW pin photodiodes

A schematic view of a waveguide integrated MQW pin PD is shown in Fig. 24. The pin PD mesa consists of a p-contact with heavy p-doping, an intrinsic MQW absorber layer, and a n-contact with heavy n-doping. The PD mesa is located on top of an optical single-mode waveguide. The input light will be coupled from a

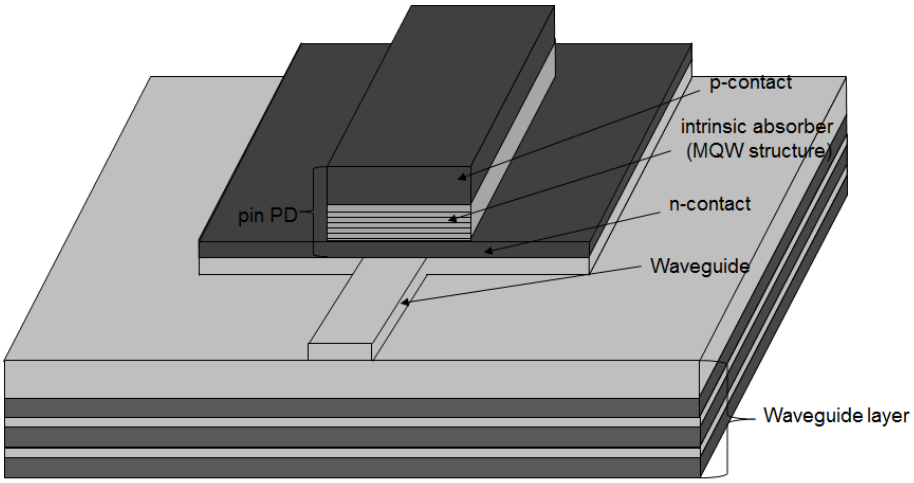

Fig. 24 3-D schematic diagram of waveguide integrated MQW pin PD.

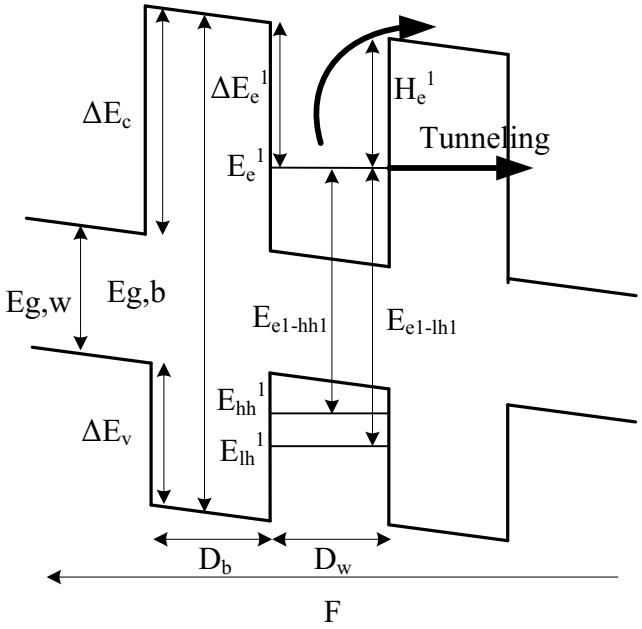

Fig. 25 Schematic diagram of carrier transit phenomenon in MQW layers.

tapered fiber into the single-mode waveguide and then coupled evanescently into the MQW pin PD. The n-contact layer works also as the light coupling layer from waveguide layer to the intrinsic MQW absorber layer.
There are many physical effects influencing the performance of the MQW p-i-n PD, such as carrier transit time through MQW layers and photon generated free carrier density.

2.4.1 Transit time

There are two main mechanisms for free carriers to sweep out of the MQW layers into the n-contact for electrons and the p-contact for holes [34]. One is thermal emission and the other one is tunneling.
Due to thermal energy, the free carriers transit over the barrier energy heights to the nearby barrier layer as shown in Fig. 25. The thermal transit time can be expressed as [35]

$$\tau_{therm,i} = \left(\frac{2\pi m_i D_w^2}{k_B T}\right)^{1/2} \exp\left(\frac{H_i(\boldsymbol{F})}{k_B T}\right) \tag{66}$$

where the subscript *i* can be *e* for the electron, *hh* for the heavy hole, and *lh* for the light hole, because the transit time for electrons, heavy holes, and light holes can differ. m_i stands for the effective mass in wells, $\mathrm{D_w}$ represents the well thickness, T is the temperature, e is the charge of electron, and ΔE_i represents the effective barrier height for electrons, heavy holes, or light holes. F is the electric field strength. $H_i(F)$ is the barrier height, which can be expressed as [34]

$$H_i(F) = \Delta E_i - e \cdot F \cdot \mathrm{D_w}. \tag{67}$$

Tunneling happens when free carriers get through the barrier layers into next wells, as shown in Fig. 25. The tunneling time can be expressed as [35]

$$\tau_{tunnel,i} = \left(\frac{2m_i D_w^2}{\pi\hbar}\right) \exp\left(\frac{2D_b\sqrt{2m_{bi}H_i(F)}}{\hbar}\right) \tag{68}$$

where D_b is the barrier thickness and m_{bi} is the effective mass in barrier layer for electrons, heavy holes, or light holes. According to Eq. (73), the carrier tunneling time is exponentially dependent on the barrier thickness.
Thus, considering the carrier drift phenomenon the total carrier transit time through MQW layers is obtained [35]

$$\tau_i = n \cdot \left(\frac{1}{\tau_{tunnel,i}} + \frac{1}{\tau_{therm,i}}\right)^{-1} + \frac{n(D_w + D_b)}{\upsilon_i} \tag{69}$$

where n is the number of MQW layers and υ_i the carrier drift velocity in MQW layers.
The transit time for TE and TM absorption can be different. Electrons, heavy holes, and light holes are generated by absorbing a TE polarized light, while only electrons and light holes are generated by absorbing a TM polarized light.

According to Eqs. (66)-(69), electrons, heavy holes, and light holes have different transit times because of different effective masses and barrier heights. Considering the polarization of the input light the transit time through MQWs can be further obtained

$$\tau = \max(\tau_e, \tau_{hh}, \tau_{lh})\ for\ TE, \tag{70}$$

$$\tau = \max(\tau_e, \tau_{lh})\ for\ TM. \tag{71}$$

Here τ_e, τ_{hh} and τ_{lh} are the electron, heavy hole, and light hole transit time through the MQW layers obtained using Eqs. (66)-(69).

The transit time in MQW layers is limited by the large tunneling time and thermal emission time. However, in a p-i-n PD with an intrinsic bulk material as the absorber layer, the transit time is mainly limited by the carrier drift velocity v_i (i: e for electron, h for holes) and the thickness D_{abs} of the intrinsic absorber layer

$$\tau = \frac{D_{abs}}{v_i}. \tag{72}$$

If the transit time is comparable to or even larger than the recombination time, the free carriers produced by absorbed photons will recombine before they transit through the quantum wells to the electrodes. In this case the free carriers will not contribute to the photocurrent. It decreases the optoelectronic conversion efficiency.

Because of the different transit time of electrons and holes, the electron densities and the hole densities are different in the quantum wells, building up a space charge [34] [36]. The effect becomes important with the increasing input light intensity. The space charge distorts the electric field and generates field non-uniformities. When reducing the applied electric field, the transit time increases, which decreases the internal quantum efficiency. The field non-uniformity causes exciton broadening, which leads to a reduction in the exciton peak absorption.

From Eqs. (66)-(69) the main design parameters for influencing the transit time are: the applied electrical field, the temperature, and the structure of MQW (material and geometry). The material and geometry determine the effective mass, the well thickness, the barrier thickness, and the barrier height. The large electric field strength lowers the barrier height $H_i(F)$ and consequently decreases the transit time. By increasing temperature, the transit time decreases simultaneously. Large effective carrier mass increases the transit time. Typically, for zero strained MQW layers, the transit time for the TM absorption is smaller than that for the TE absorption, due to the smaller effective mass and the lower barrier height of light holes compared to heavy holes.

2.4.2 DC saturation effects generated by the photocurrent

The optical absorption spectrum of MQW structures, especially the excitonic absorption, can be strongly affected by free carriers. Large free carrier densities can depress or even fully quench the strong excitonic absorption in MQWs which leads to the saturation of the optical absorption. Increasing the input light power, more excitons and free carriers are produced in quantum wells. For large free carrier densities, the free carrier induced effects on excitonic features are essentially due to the many-body effects. The many-body effects can be summarized as two main categories: the charge screening and the phase-space filling.

The charge screening effect can be understood as the phenomenon of the interaction between charge carriers and excitons. With absorbing light, excitons and free carriers are generated in MQW layers. Because of the coexistence of excitons and free carriers, the Coulomb interaction between the electron and hole of an exciton will be affected, or even screened by the free carriers [36]. Moreover, if the input light intensity is very high, only free electrons and holes instead of excitons are generated. For this reason, the free carriers reduce the exciton binding energy and lifetime, which in turn reduces the excitonic absorption.

Phase-space filling comes from the Pauli Exclusion Principle. Fig. 26 illustrates the saturation absorption due to filling space with excitons and free carriers. Since two electrons cannot be in the same state at the same time, the free carriers which occupy the states near the bandgap of the well where excitons are located prevent creation of more excitons [4]. It causes directly a reduction of exciton binding energy by reducing the number of single-particle states that contribute to excitons [37]. As a result, the excitonic absorption reduces.

Both effects reduce the excitonic absorption, leading to saturation of the optical absorption. To describe the saturation of the absorption, the dependence of the absorption coefficient on the input light intensity I can be expressed as [38]

$$\alpha(I) = \frac{\alpha_0}{1 + I/I_s} \tag{73}$$

where α_0 is the absorption coefficient without considering saturation of the optical

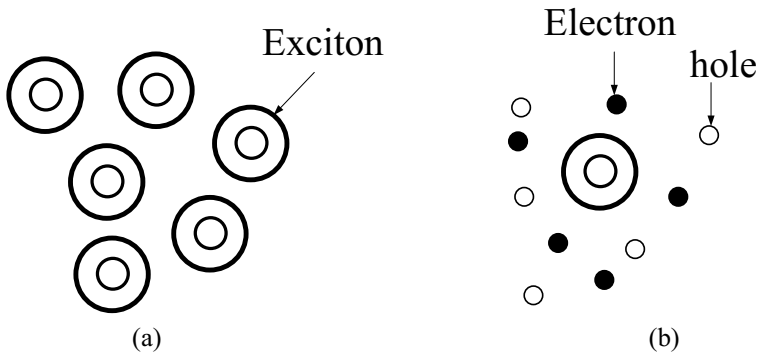

Fig. 26 Illustration of saturation by (a) excitons filling space and (b) free carrier filling space.

absorption and I_s is the saturation intensity. I_s can be obtained with [38]

$$I_s = \frac{\hbar\omega N_s}{\alpha_0(D_w + D_b)} \frac{m_e + m_h}{m_e\tau_{lifetime,h} + m_h\tau_{lifetime,e}} \tag{74}$$

where N_s is the saturation density of the excitons (cm^{-2}) [38], D_w and D_b are the thickness of wells and barriers, respectively. $\tau_{lifetime,e}$ and $\tau_{lifetime,h}$ are the lifetime of holes and electrons. The corresponding optical saturation power P_s can be obtained as $P_s = I_s \times S_{mode}$, where S_{mode} is the area of the optical mode. Considering the recombination time $\tau_{recombination,i}$ and the carrier transit time τ_i from Eq. 69, the carrier lifetime can be expressed as [34]

$$\tau_{lifetime,i} = \left(\frac{1}{\tau_{recombination,i}} + \frac{1}{\tau_i}\right)^{-1}, \tag{75}$$

$$\tau_{recombination,i} = \frac{1}{\zeta_1 + 2\zeta_2 N + 3\zeta_3 N^2} \tag{76}$$

where i can be e for electron and be h for hole, ζ_1 is the recombination coefficient for impurity, defect, or at surface, ζ_2 is the coefficient for bimolecular recombination, ζ_3 is the coefficient for Auger recombination, and N is the carrier density (cm^{-3}).

By increasing the transit time, the internal quantum efficiency decreases and the exciton linewidth is broadened, while large free carrier densities saturate the exciton absorption. Furthermore, according to Eq. (73) and Eq. (74), the carrier transit time affects saturation of the absorption. Typically, free carriers generated by absorbing photons are immediately swept out of the quantum well area, attributing to the photocurrent. However, because of large transit times, additional free carriers will be generated, before the other free carriers transit over the quantum wells. Thus, free carriers accumulate, leading to the increasing free carrier density. The free carrier density N_i (cm^{-3}) generated with input light intensity of I can be expressed by [34]

$$\begin{cases} N_e = \dfrac{I\alpha_0\tau_{lifetime,e}}{\hbar\omega} \; for\ electrons \\ N_h = \dfrac{I\alpha_0\tau_{lifetime,h}}{\hbar\omega} \; for\ holes \end{cases}. \tag{77}$$

The free carrier density is proportional to carrier lifetime. For typical p-i-n PDs, the carrier recombination time is large (in the μs range) in intrinsic absorption layers. For this reason, the saturation intensity I_s depends strongly on the carrier transit time.

3. Modeling of waveguide integrated MQW pin PD

To design MQW PDs, there are several issues such as carrier transit time and carrier density that have to be considered. However, there are no commercial design tools for the modeling of MQW PDs. In this chapter, a numerical model is introduced for simulating the performances of MQW PDs, such as the responsivity, the PDL, the DC saturation of optical absorption, the dark current, and the frequency response. Firstly, a theoretical model of the optical absorption coefficient of MQW structures is presented. The MQW materials are taken from InGaAsP and InGaAlAs material systems for telecommunication applications. By solving Poisson equation and Schrödinger equation, the optical absorption with different input light intensities, different input light wavelengths, and different input light polarization can be accurately described. After obtaining the optical absorption spectra of the MQW structures, the responsivity and the PDL are modeled. The modeling of the responsivity and the PDL of MQW p-i-n PDs includes the optical simulation (evanescent coupling) of waveguide integrated MQW pin PDs, the transit time induced internal quantum efficiency, and the saturation of optical absorption. After that the modeling of the dark current is presented. Finally, the RF performances such as the bandwidth, the maximum RF output power, and the nonlinearity of the waveguide integrated MQW p-i-n PDs are modeled.

3.1 Modeling of the absorption coefficient spectra

To simulate the optical absorption spectra, the Schrödinger equation is solved to get discrete energy levels E_j and their corresponding wave-functions φ_j, as the first step according to the theory presented in Chapter 2. To solve the Schrödinger equation, the basic physical parameters such as the bandgap, the effective mass, and the lattice constant of the InGaAsP and InGaAlAs material systems are applied. In this paper, the following model is used for these basic physical parameters. The unstrained bandgap of these two material systems is given as [26]

$$\begin{aligned} &E_g\left(In_{1-x}Ga_xAs_yP_{1-y}\right)\,(eV) \\ &\quad = 1.35 + 0.668x - 1.068y + 0.758x^2 + 0.078y^2 \\ &\quad - 0.068xy - 0.322x^2y + 0.03xy^2\ (0 \le x, y \le 1), \end{aligned} \tag{78}$$

$$\begin{aligned} &E_g\left(In_{1-x-y}Ga_xAl_yAs\right)\,(eV) \\ &\quad = 0.36 + 0.629x + 2.093y + 0.436x^2 + 0.577y^2 \\ &\quad + 1.013xy - 2.0xy(1-x-y)\ (0 \le x + y \le 1). \end{aligned} \tag{79}$$

Other physical parameters J such as the effective mass and the lattice constant of the two material systems with arbitrary composition can be derived from the interpolations between the corresponding physical parameters of the relevant binary semiconductors [26]

$$J\left(In_{1-x}Ga_xAs_yP_{1-y}\right) = J(GaAs)xy + J(GaP)x(1-y) + J(InAs)(1-x)y + J(InP)(1-x)(1-y)\ (0 \le x, y \le 1), \tag{80}$$

$$J\left(In_{1-x-y}Ga_xAl_yAs\right) = J(InAs)(1-x-y) + J(GaAs)x + J(AlAs)y \quad (0 \le x+y \le 1). \tag{81}$$

The basic parameters at room temperature (300K) of the binary semiconductors are listed in Table 1 [26] [39] [40]. $m_{hh//}$ and $m_{lh//}$ are the effective heavy hole and light hole mass in plane of the quantum well layers, while $m_{hh\perp}$ and $m_{lh\perp}$ are the effective heavy hole and light hole mass perpendicular to the quantum well layers. The elastic stiffness factor G, hydrostatic deformation potential a_c and a_v, and shear deformation potential for valence band b are used to calculate the bandgap energy considering strains.

With the calculated strain using Eq. (36)-Eq. (37), the shift of the conduction band and the valence bands can be calculated

$$\delta E_c(x,y) = 2a_c(1-G)\epsilon, \tag{82}$$

$$\delta E_{hh}(x,y) = 2a_v(1-G)\epsilon + b(1+2G)\epsilon, \tag{83}$$

$$\delta E_{lh}(x,y) = 2a_v(1-G)\epsilon - b(1+2G)\epsilon \tag{84}$$

where the strain ϵ is defined as

$$\epsilon = \left(a_s - a(x,y)\right)/a(x,y) \tag{85}$$

with a_s the lattice constant of the substrate. The modified bandgaps considering the strain can be obtained

$$E_{\mathrm{g,e-hh}}(x,y) = E_g(x,y) + \delta E_c(x,y) - \delta E_{hh}(x,y), \tag{86}$$

$$E_{\mathrm{g,e-lh}}(x,y) = E_g(x,y) + \delta E_c(x,y) - \delta E_{lh}(x,y). \tag{87}$$

The particles (electrons and holes) in MQWs under an external electrical field can be described using the Schrödinger equation according to Eq. (65). The discontinuity factor (band offset ratio) is obtained as $\Delta E_c/\Delta E_g$ = 0.4 for InGaAsP/InGaAsP interface and as $\Delta E_c/\Delta E_g$ = 0.7 for InGaAlAs/InGaAsP interface.

Table 1 Physical parameters for the $In_{1-x}Ga_xAs_yP_{1-y}$ and $In_{1-x-y}Ga_xAl_yAs$ material systems

Parameter	Symbol(unit)	GaAs	GaP	InAs	InP	AlAs
Lattice constant	a(Å)	5.65	5.45	6.058	5.87	5.66
Electron effective mass	m_e/m_0	0.067	0.114	0.024	0.0793	0.15
Heavy-hole effective mass	$m_{hh//}/m_0$	0.11	0.19	0.032	0.15	0.18
	$m_{hh\perp}/m_0$	0.5	0.54	0.517	0.56	0.79
Light-hole effective mass	$m_{lh//}/m_0$	0.23	0.34	0.082	0.29	0.36
	$m_{lh\perp}/m_0$	0.088	0.16	0.024	0.12	0.15
Elastic Stiffness Factor	G	0.45	0.44	0.54	0.55	0.43
Hydrostatic deformation potential						
for conduction band	a_c (eV)	-7.2	-7.1	-5.08	-5	-5.64
for valence band	a_v(eV)	1.16	1.7	1	1.27	2.47
Shear deformation potential for valence band	b(eV)	-1.7	-1.8	-1.8	-1.7	-1.5

With the physical parameters for the MQW material systems, the finite-difference analysis method (FDM) is used to solve the Schrödinger equation to get the eigen energy levels E_j and their corresponding eigen wavefunctions φ_j. The FDM is listed in the Appendix in Section 8.1.

As discussed in Chapter 2, the important parameter of the broadening width Γ is dependent on temperature and the strength of the electric field. The following models are used to calculate the broadening width for the band-to-band transition Γ_{con} and for excitons Γ_{ex}

$$\Gamma_i = \Gamma_{0,i} + \Gamma_{T,i}(T) + \Gamma_{F,i}(F), \tag{88}$$

$$\Gamma_{T,i}(T) = \frac{\Gamma_{ph,i}}{\exp\left(\frac{\hbar\omega_{LO,i}}{k_B T}\right) - 1}, \tag{89}$$

$$\Gamma_{F,i}(F) = \mathrm{F}/\Gamma_{F0,i} \tag{90}$$

where i = *con* (for the band-to-band transition), i = *ex* (for excitons), Γ_T and Γ_F stand for temperature dependent term and electric field dependent term, respectively. Γ_{ph}, Γ_0, Γ_{F0}, and ω_{LO} are constant as shown in Table 2. It is worth mentioning that these parameters may be different for the continuous band-to-band transition, electron-heavy hole excitons, and electron-light hole excitons.

Table 2 Parameters for broadening width [33]

Symbol	$\Gamma_{0,con}$	$\Gamma_{0,ex\text{-}e\text{-}hh}$	$\Gamma_{0,ex\text{-}e\text{-}lh}$	Γ_{ph}	Γ_{F0}	$\hbar\omega_{LO}$
Value [meV]	13.5	6	13	4.4	20	36

The exciton binding energy E_b and the exciton radius λ_{ex} can be calculated by a variational method to maximize the exicton binding energy E_b [28]

$$E_b(\lambda_{ex}) = -\frac{\hbar^2}{2\mu{\lambda_{ex}}^2} + \frac{e^2}{4\pi\varepsilon}\left\langle\varphi_{ex}\left|\frac{1}{\vartheta}\right|\varphi_{ex}\right\rangle \tag{91}$$

where μ is the reduced effective mass parallel to the quantum-well layers which can be expressed by

$$\mu = \frac{1}{m_e} + \frac{1}{m_h^{//}} \tag{92}$$

where m_e and $m_h^{//}$ are the effective masses of electron and hole, respectively. φ_{ex} is the wave function of the exciton which is given in Eq. (57). ϑ represents the relative position between particles which is denoted by [28]:

$$\vartheta = \sqrt{(z_e - z_h)^2 + |\boldsymbol{r}|^2} \tag{93}$$

where z_e and z_h are the z coordinates of the electron and the hole, respectively. The relative coordinate $\boldsymbol{r} = \boldsymbol{r}_e - \boldsymbol{r}_h$, where $\boldsymbol{r}_e$ and $\boldsymbol{r}_h$ are the positions of the electron and hole [28].

Finally, the absorption coefficient of the band-to-band transition α_{con} and the excitonic absorption α_{ex} can be calculated by substituting the obtained eigen energy levels E_j, their corresponding eigen wavefunctions φ_j, the broadening width Γ, the exciton binding energy E_b, and the exciton radius λ_{ex} into the Eq. (54)-Eq. (56) and into the Eq. (59)-Eq. (62), respectively. The total absorption coefficient α is then the sum of α_{con} and α_{ex}. All the calculations are simulated using Matlab. The matlab codes are listed in the Appendix.

3.2 Modeling of the responsivity spectra

3.2.1 Modeling of responsivity using light propagation software

After getting the absorption coefficient α according to the model in Section 3.1, without considering the effects of carrier transit time and free carrier density, the responsivity spectra R_e for TE and TM polarizations of waveguide integrated MQW PDs can be calculated using

$$R_e = (1 - R_0)\kappa[1 - \exp(-\alpha \int_0^{l_{pd}} \Pi_{xy}(z)dz)]R_{ideal} \tag{94}$$

where R_0 is the reflectivity of the front surface, κ is the input coupling efficiency due to the modal mismatch, l_{PD} represents the length of the photodiode, Π_{xy} is the light confinement factor along PD, and $\mathrm{R}_{ideal} = \frac{q}{h\upsilon} = \frac{\lambda}{1.24\mu m}[\frac{A}{W}]$ is the ideal responsivity, being 1.255A/W at a wavelength of 1.55μm. The light confinement factor $\Pi_{xy}(z)$ describes the fraction of the light power confined in the absorber cross section S_{abs} at certain position of z. The confinement factor of the light along the PD can be calculated

$$\Pi_{xy}(z) = \frac{P_{abs}(z)}{P(z)} = \frac{\int^{S_{abs}} I(x,y,z)dS}{\int_{-\infty}^{+\infty} I(x,y,z)dS} \tag{95}$$

where $I(x,y,z)$ is the field intensity. As discussed in Section 2.1.2, for the waveguide integrated PD, the input light is evanescently coupled from the single mode waveguide to the PD mesa. The distribution of the field intensity along the waveguide integrated PD is simulated using commercial light propagation software such as Rsoft´s Beamprop or PhotonDesign´s Fimmprop with the calculated absorption coefficient α. The light power $P(z)$ is calculated by

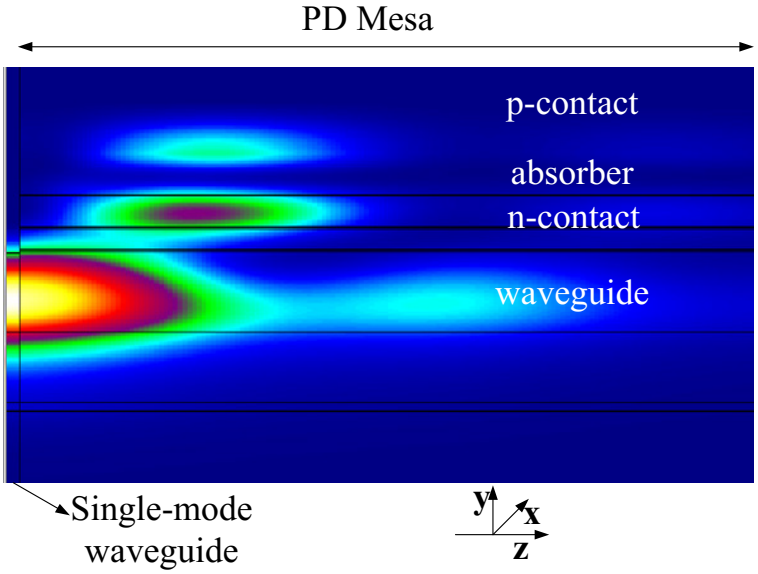

Fig. 27 Side view of the simulated optical intensity distribution along the waveguide integrated PD for TE polarized input light. The intensity is averaged over the x direction

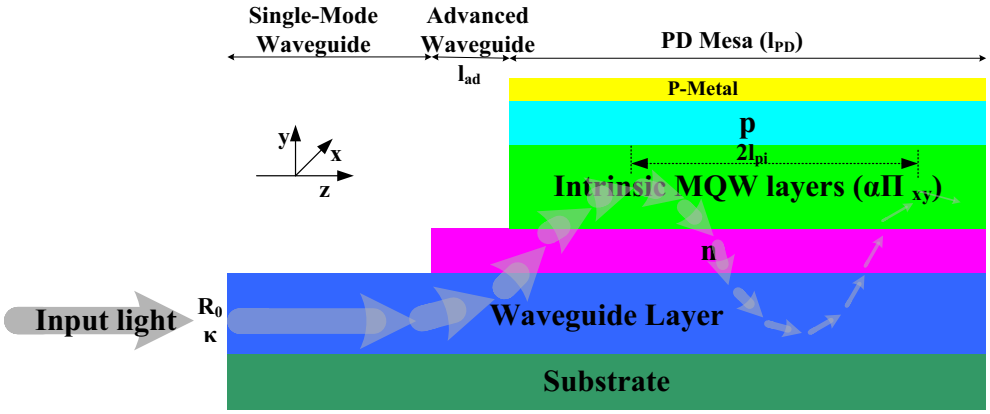

Fig. 28 Side view of the light distribution along the waveguide integrated PD with the advanced waveguide.

integrating the field intensity over the interested cross section in *xy* plane $P(z) = \iint I(x,y,z)dxdy$ (entire cross section for *P(z)* and only the cross section of the absorber for $P_{abs}(z)$). In this work, Fimmwave has been used to predict and simulate quantitatively the optical properties of the waveguide integrated MQW PD. Fig. 27 gives an example of a simulated structure from Fig. 3. The materials and the thicknesses of the n-contact layer and p-contact layer can be optimized based on the beat length l_{pi} and the imaginary part of the effective index of the corresponding modes according to Eq. (5) and Eq. (6).

Furthermore, a multi-mode waveguide called as the advanced waveguide which is formed by extending the n-contact layer is inserted between the single-mode waveguide and the PD mesa, as shown in Fig. 28. This advanced waveguide helps enhance the absorption process in the PD. The optimum device length ($=l_{ad}+ l_{PD}$) is related to the beat length l_{pi}. In this case, the n-contact layer not only provides a refractive index match between the waveguide and absorber but also controls the optical intensity distribution in the PD in dependence of the length of the advanced waveguide l_{ad}. Moreover, this advanced waveguide helps to reduce the influence caused by the misalignment between the single mode waveguide and PD mesa during the fabrication. More details of the design of the waveguide integrated MQW p-i-n PD can be found in the Fig. 28.

3.2.2 Modeling of responsivity considering internal quantum efficiency and saturation of optical absorption

After getting the ideal responsivity with the calculated absorption coefficient using the light propagation software, the effects of the carrier transit time and the free carrier density are to be considered in the model.

When the carrier transit time through the MQW layers is comparable to or even larger than the carrier recombination time, the photocurrent decreases, which can

be described as internal quantum efficiency η_{in}. The internal quantum efficiency can be written as

$$\eta_{in} = \tau_{recombination}/(\tau_{recombination} + \tau) \tag{96}$$

where $\tau_{recombination}$ is the carrier recombination time which can be calculated using Eq. (76) (ζ_1 = 6.6x10^5 s^{-1}, ζ_2 = 1.43x10^{-10} cm^3/s, ζ_3 = 8.1x10^{-29} cm^6/s for $InGa_{0.47}As$) and τ is the carrier transit time through the MQW layers from Eq. (66) – Eq. (71). According to Eq. (96), η_{in} equals one when the carrier transit time through MQW layers is at least two-order of magnitude smaller than the carrier recombination time which is in order of μs for the intrinsic InGaAs material.
Besides the transit time, the free carrier density affects the responsivity. As discussed in Section 2.4.2, a large free carrier density induces the saturation of optical absorption. The absorption efficiency due to the saturation of optical absorption can be described as

$$\eta_s(I,\tau) = \frac{1}{1 + (I/I_s)^a} \tag{97}$$

where I_s is the saturation light intensity which can be calculated using Eq. (73), and a is a correction factor. To obtain the absorption efficiency of 1, the input light intensity should be at least two orders of magnitude less than the saturation intensity I_s.
Summarizing Section 3.2.1 and 3.2.2, the model for responsivity R can be written as

$$R = \eta_{in}\eta_s(I,\tau)R_e = \eta R_e \tag{98}$$

where η is the absorption efficiency considering the effects of transit time and free carrier density and R_e is the responsivity without considering the effects of transit time and free carrier density which can be calculated using Eq. (94). The PDL is defined as

$$PDL = 10\log\left({R_{TE}}/{R_{TM}}\right) \tag{99}$$

where R_{TE} and R_{TM} are the responsivity with TE and TM polarized input light, respectively.

3.3 Modeling of current-voltage characteristic

To determine the bandwidth of the PD, the series resistance of the PD should be studied. Normally, the series resistance can be analyzed according to the forward

current of the PD. The current at forward voltages and reverse voltages can be generally modeled as [44] [45]

$$I(V) = I_0 \left[\exp\left(\frac{(eV - IR_s)}{n_F k_B T}\right) - 1\right] \tag{100}$$

where e is the electron charge, V is the applied voltage, R_s is the series resistance, k_BT is the thermal energy, I_0 is the reverse saturation current, and n_F is the ideality factor. The series resistance R_s includes contact resistance, bulk and sheet resistances, and the resistance in the undepleted MQW region.

I_0 denotes the dark current level for a reverse bias, which can be calculated

$$I_0 = eSp_{n0}\sqrt{\dot{D}_p/\tau_{p0}} + eSn_{p0}\sqrt{\dot{D}_n/\tau_{n0}} \tag{101}$$

where $\dot{D}_p$ and $\dot{D}_n$ are the diffusion coefficient for holes and electrons, τ_{p0} and τ_{n0} are the carrier lifetime for holes and electrons which can be calculated using Eq. (76), and S is the PD area. n_{p0} and p_{n0} are the electron minority density in p region and the hole minority density in n region under thermal equilibrium condition, respectively.

At the low current injection (low forward biases), the IR_s product is negligible in comparison to the applied voltage and the model can be simplified as

$$I(V) = I_0 \left[\exp\left(\frac{eV}{n_F k_B T}\right) - 1\right]. \tag{102}$$

The ideality factor n_F equals 1 if the diode's space charge is limited by diffusion, while n_F equals 2 if the space charge is limited by the recombination. If the transit time is much smaller than the carrier lifetime (in the order of μs), the model with n_F=1 should be used. If the transit time is comparable to or larger than the carrier lifetime, n_F=2 is used in the model.

At high current injection (high forward bias), the voltage drop across the series resistance controls the I-V characteristics. The current no longer increases exponentially with the voltage. Instead, it increases linearly due to the series resistance. The model for I-V characteristics at high current injection is described as

$$I(V) = \frac{V}{R_s} + I_a \tag{103}$$

where I_a is a fitted parameter. The series resistance R_s can be approximately written as:

$$R_s = \frac{{D_d}^2}{(\mu_n + \mu_p) I \tau} + R_{s0} \tag{104}$$

where D_d is the thickness of the undepleted MQW region at a forward bias, μ_n and μ_p are the carrier mobility for electrons and holes, respectively, I is the current, τ is

the minority carrier transit time through the undepleted MQW region, and R_{s0} is the sum of the contact, bulk, and sheet resistances of the p-contact and n-contact. Using the equations above, the dark current at reverse biases and the series resistance of the PD can be analyzed. The large transit time reduces the reverse saturation dark current according to the Eq. (101). Moreover, the resistance in the undepleted MQW region becomes dominant in the series resistance by increasing the transit time. As a result, the series resistance increases.

3.4 Modeling of RF performances

3.4.1 Modeling of bandwidth

The bandwidth of a p-i-n photodiode is mainly limited by the carrier transit time and the RC constant. To discuss about the RF performances of the p-i-n PD, an equivalent circuit of a p-i-n photodiode at the reverse bias condition is shown in Fig. 29. In the model, the optical input signal $P(t) = P_0 + P_1 cos(\omega t)$ consists of a CW optical power P_0 and an AC optical power $P_1 cos(\omega t)$. The AC optical power P_1 is obtained as $P_1 = mP_0$, where m is the modulation ratio ($0 \leq m \leq 1$) The optical input signal *P(t)* is approximated as an input voltage source $V(t) = V_0 + V_1 cos(\omega t)$. The AC photo current i_L is taken as the output. The effects of the carrier transit time (region 1 in Fig. 29) and the *RC* constant (region 2 in Fig. 29) are taken into consideration. To analyze the transit time response of the photodiode, the R_tC_t delay block in region 1 is fed with the input AC voltage source V_1. V_2 is the output AC voltage after the transit time block. The output AC voltage controls the AC photo current source *i* of region 2: $i=g_mV_2$, where g_m represents the optical to electrical conversion efficiency known as the responsivity *R* from Eq. (98). In region 2, the *RC*-effect is considered as a current source *i* parallel with a capacitance C_{PD}, a resistance R_P, a series resistance R_s, an inductance L_{PD}, and a load impedance R_L. Normally, the parallel resistance R_p is very high due to a nA-scale parallel leakage current. R_L is the load resistance

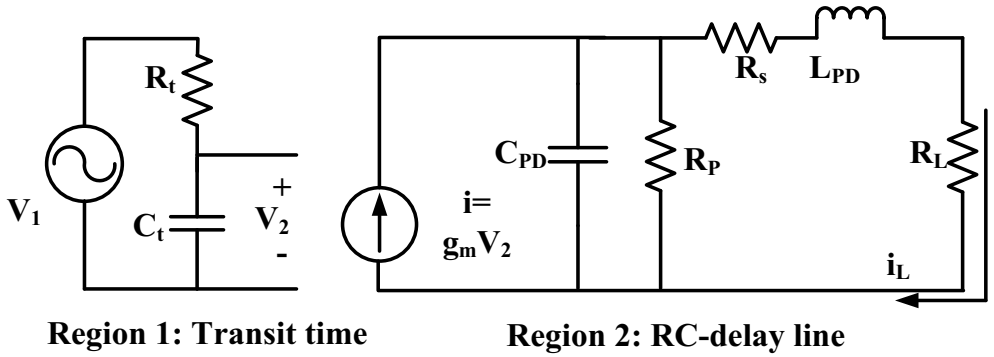

Fig. 29. Equivalent circuit of a lumped photodiode.

which is 50Ω for most applications. L_{PD} is the inductance caused by the electrical interconnection which is very small because of short electrical connection lines. The parallel capacitance C_{PD} is determined by the barrier capacitance C' in the depletion region and the parasitic capacitance C_p. The barrier capacitance C' is determined by the area of the photodiode $A=l_{PD}\cdot w_{PD}$ and the thickness of the depletion region D_d [16].

$$C_{pd} = C' + C_p, \tag{105}$$

$$C' = \frac{\varepsilon_0 \varepsilon_r A}{D_d}, \tag{106}$$

where l_{PD} is the length of the PD, w_{PD} is the width of the PD, ε_r is the dielectric constant of the depleted region, and D_d is the thickness of the depletion region which is the thickness of the intrinsic MQW absorber layer in our case. The series resistance R_s includes the bulk, the sheet, and the contact resistance.

The relative frequency response due to the transit time in region 1 is expressed as [43]

$$H_t(\omega) = \frac{V_2}{V_1} = \frac{1}{1 + j\omega R_t C_t} \tag{107}$$

$$R_t C_t = \frac{\tau}{3.5} \tag{108}$$

Where $\omega=2\pi f$, and τ is the transit time according to Eq. (70)-(71). It worth mentioning that the transit time for TE and TM input light can be different. The 3-dB bandwidth due to the transit time limitation can be approximated with

$$f_t = \frac{3.5}{2\pi\tau} \tag{109}$$

A relative transfer function for region 2 can be used to describe the frequency dependent current which flows through the load

$$H_{RC}(\omega) = \frac{i_L}{i} = \frac{1}{1 - \omega^2 L_{PD} C_{PD} + i\omega C_{PD} R_{tot}} \tag{110}$$

where R_{tot} is the total resistance,

$$R_{tot} = R_s + R_L\,. \tag{111}$$

Neglecting the inductance, the 3-dB bandwidth due to *RC* limitation is obtained

$$f_{RC} = \frac{1}{2\pi C_{PD} R_{tot}}, \tag{112}$$

Considering the transit time limitation and the RC limitation, the total relative frequency response is obtained as

$$H(\omega) = H_t(\omega) H_{RC}(\omega) = \frac{1}{1 + j\omega R_t C_t} \cdot \frac{1}{1 + j\omega R_{tot} C_{PD}} \tag{113}$$

The power related frequency response on a logarithmic scale is $H(\omega)[dB] = 20\log(H(\omega))$. The 3-dB bandwidth is approximated as

$$f_{3dB} \approx \sqrt{\frac{1}{\frac{1}{f_{RC}^2}+\frac{1}{f_t^2}}}. \tag{114}$$

3.4.2 Modeling of RF saturation

The maximum electrical output power is limited by the space-charge effect and the thermal failure. In this work, only the space-charge effect is considered because the PDs typically operate below the thermal failure limit. The electrical output power is calculated

$$\begin{aligned} \mathrm{P}_L(\omega) = {i_L}^2 \mathrm{R_L} &= \left(\frac{R\mathrm{P}_1}{(1+\mathrm{j}\omega \mathrm{R_t C_t})(1+\mathrm{j}\omega \mathrm{R_{tot} C_{PD}})}\right)^2 \mathrm{R_L} \\ &= (\mathrm{H}(\omega)\mathrm{P}_1 \mathrm{R})^2 \mathrm{R_L}. \end{aligned} \tag{115}$$

The electrical output power on a logarithmic scale is calculated as $\mathrm{P}_L(\omega)[\mathrm{dBm}] = 10\log\left(\frac{\mathrm{P}_L(\omega)}{1mW}\right)$. Fig. 30 shows the typical behavior of the electrical output power of a PD as the function of the optical input power according to Eq. (115).

At low optical input power, the electrical field in the depletion region is not collapsed and the free carriers drift with constant saturation velocity. The parameters R, τ, R_{tot} and C_{PD} are constant with the optical input power causing the constant relative frequency response $H(\omega)$ with the continuum wave (CW) optical input power $\left(\frac{d(H(\omega))}{dP_0} = 0\right)$. Thus, the RF output power increases with the square of the optical input power (dotted curve in Fig. 30, $\left(\frac{dP_L\,[dBm]}{dP_0\,[dBm]} = 2\right)$. This means

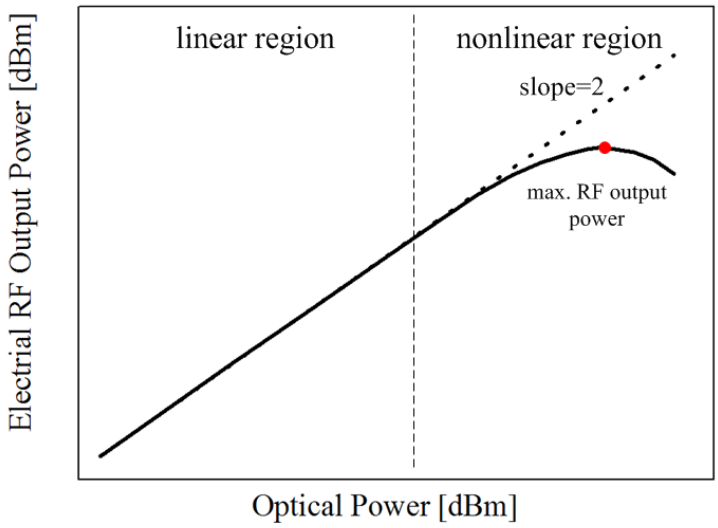

Fig. 30. Schematic plot of the electrical output power of a PD versus optical input power.

that the PD operates in the linear region.

At large CW optical input power, the parameters τ and C_{PD} vary with the optical input power leading to the dependence of relative frequency response H(ω) on the CW optical input power $\left(\frac{d(H(\omega))}{dP_0} \neq 0\right)$. Thus, the RF output power changes nonlinearly with the square of the optical input power. As a consequence, the PD operates in the nonlinear region. If the relative frequency response H(ω) increases with optical input power $\left(\frac{d(H(\omega))}{dP_0} > 0\right)$, the increase of the RF output power with the optical input power satisfies the inequality of $\frac{dP_L(\omega)\,[dBm]}{dP_1[dBm]} > 2$. If the relative frequency response H(ω)decreases with optical input power $\left(\frac{dH(\omega)}{dP_0} < 0\right)$, the RF output power increases slowly with the square of the optical input power $\left(\frac{dP_L(\omega)\,[dBm]}{dP_1\,[dBm]} < 2\right)$. If the slope of the relative frequency response H(ω) with the optical input power is less than -1, the RF output power decreases with the optical input power. In the nonlinear region, the RF output power reaches its maximum when $\frac{dH(\omega)[dB]}{dP_0[dBm]} = -1$.

According to the model above, if the relative frequency response $H(\omega)$ of a PD has a weak dependence on the optical input power, more RF output power can be achieved.

3.4.3 Modeling of nonlinearity

Many effects such as the space-charge effect, the nonzero load resistance, scattering, recombination, and trap sites cause the nonlinear behavior of PDs. By decoupling the parameters such as R, τ, R_{tot} , and C_{PD}, the root causes for the nonlinearity can be separated and analyzed.

The nonlinear behavior of the PD can be explained by the variation of the parameters R, τ, R_{tot} and $C_{PD}$with the optical input power and the bias voltage. The dependence of the parameter on the voltage or the CW optical input power can be expressed as

$$\Upsilon = a_{0,\Upsilon} + a_{1,\Upsilon}\Psi + a_{2,\Upsilon}\Psi^2 + a_{3,\Upsilon}\Psi^3 \tag{116}$$

where Υ represents the parameter of R, τ, R_{tot} or C_{PD}. Ψ is either the voltage V or the CW optical input power P_0. $a_{0,\Upsilon}$ is the voltage and optical input power independent constant, $a_{n,\Upsilon}$ (n=1, 2, 3) is the n^{th}-order nonlinear factor of the parameter Υ.

Using Taylor expansion, the AC output photocurrent can be written as:

$$
\begin{aligned}
&\mathrm{i_L}(\Psi_0 + \Delta\Psi) \\
&\quad = \mathrm{i_L}(\Psi_0) + \mathrm{k_{1,R}b_R}\Delta\Psi + \mathrm{k_{1,\tau}b_\tau}\,\Delta\Psi \\
&\quad + \mathrm{k_{1,R_{tot}}b_{R_{tot}}}\Delta\Psi + \mathrm{k_{1,C_{PD}}b_{C_{PD}}}\Delta\Psi + \mathrm{k_{2,r}b_r}^2\Delta\Psi^2 \\
&\quad + \mathrm{k_{2,\tau}b_\tau}^2\Delta\Psi^2 + \mathrm{k_{2,R_{tot}}b_{R_{tot}}}^2\Delta\Psi^2 \\
&\quad + \mathrm{k_{2,C_{PD}}b_{C_{PD}}}^2\Delta\Psi^2 \cdots)
\end{aligned}
\tag{117}
$$

where b_Υ is the weight parameter $\mathrm{b}_\Upsilon = {\mathrm{di_L}}/{\mathrm{d}\Upsilon}$, and

$$
\begin{cases}
\mathrm{k_{1,\Upsilon}} = {\mathrm{d}\Upsilon}/{\mathrm{d}\Psi} = \mathrm{a_{1,\Upsilon}} + 2\mathrm{a_{2,\Upsilon}}\Psi + 3\mathrm{a_{3,\Upsilon}}\Psi^2 \\
\mathrm{k_{2,\Upsilon}} = {\mathrm{d}\Upsilon^2}/{2\mathrm{d}^2\Psi} = 2\mathrm{a_{2,\Upsilon}} + 6\mathrm{a_{3,\Upsilon}}\Psi.
\end{cases}
\tag{118}
$$

The third-order intermodulation distortions (IMD3) are usually used to represent the nonlinearity in PDs, since their frequencies are close to the fundamental modulation frequencies. To determine the power of the third-order intermodulation product, it is assumed that the optical input power $\mathrm{P(t)}$ is given as: $\mathrm{P(t)} = \mathrm{P_0} + \mathrm{P_1}\cos(\omega_1\mathrm{t}) + \mathrm{P_2}\cos(\omega_2\mathrm{t})$. The AC photocurrent i_L is obtained as $\mathrm{i}_L = \mathrm{i}_{L1}\cos(\omega_1\mathrm{t}) + \mathrm{i}_{L2}\cos(\omega_2\mathrm{t}) + \mathrm{i}_{IM}\cos\big((2\omega_2 - \omega_1)t\big) + \cdots$. Using Eq. (117) and Eq. (118), the photocurrent i_{IM} at frequency $2\omega_1 - \omega_2$ as the third-order intermodulation product is obtained as

$$
\begin{aligned}
&|\mathrm{i}_{IM}(2\omega_2 - \omega_1)| \\
&\quad = \frac{3}{8}\mathrm{i_{L2}}^2\,\mathrm{i_{L,1}}\big(\mathrm{b_\tau}^2\mathrm{a_{3,\tau}} + \mathrm{b_R}^2\mathrm{a_{3,R}} \\
&\quad + \mathrm{b_{R_{tot}}}^2\mathrm{a_{3,R_{tot}}} + \mathrm{b_{C_{PD}}}^2\mathrm{a_{3,C_{PD}}}\big).
\end{aligned}
\tag{119}
$$

According to Eq. (119) the third-order intermodulation distortion product is dependent on the nonlinear coefficient $b_\Upsilon{}^2 a_{3,\Upsilon}$ of the parameters of R, τ, R_{tot}, and C_{PD}. The linear coefficient $\frac{1}{b_\Upsilon{}^2 a_{3,\Upsilon}}$ is defined as the reciprocal of its nonlinear coefficient.

If the parameters of a PD have weak dependence on the bias voltage and CW optical input power, this PD can achieve high linearity.

4. Design and Fabrication

Based on the model presented in Chapter 3, three MQW-PDs are designed. The design "InP" uses lattice matched $InGa_{0.47}As$ as the well layer and InP as the barrier layer. The design "Q1.33" uses $InGa_{0.47}As/InGa_{0.3}As_{0.64}P$ (lattice matched to InP) as the well/barrier while the design "Al" uses $InGa_{0.47}As/InGaAlAs$ (lattice matched to InP) as the well/barrier. The epitaxy layers of the three designs are optimized based on the optical propagation simulation using Fimmprop. After optimizing the epitaxy layers, the waveguide integrated MQW p-i-n PD chips of the design "InP", the design "Q1.33", and the design "Al" are fabricated.

4.1 Design of waveguide integrated MQW p-i-n PDs

Fig. 31(a) shows the 3D view of the waveguide integrated MQW p-i-n PD chip which includes a monolithically integrated spot size converter, a single mode waveguide, a single p-i-n PD using MQW layers as the intrinsic absorber, and GSG RF probe pads. The spot-size converter is used for an efficient light coupling

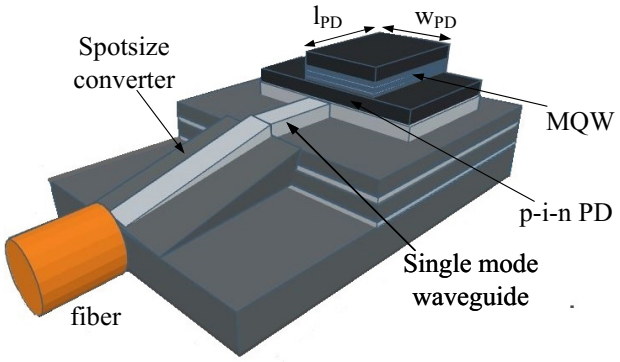

(a)

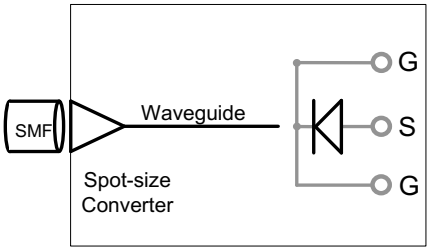

(b)

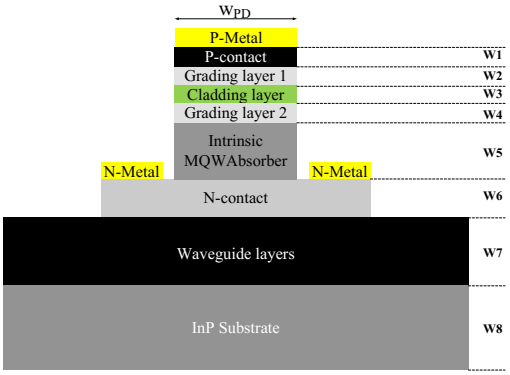

(c)

Fig. 31 (a) 3D view of the waveguide integrated MQW p-i-n PD; (b) Schematic diagram of the waveguide integrated MQW p-i-n PD; black: optical connections, grey: electrical connections; (c) cross section of the MQW p-i-n PD mesa.

Table 3 The intrinsic MQW absorber layers and the PD size of the three designs

	Design "InP"	Design "Q1.33"	Design "Al"
Well material	$InGa_{0.47}As$	$InGa_{0.47}As$	$InGa_{0.47}As$
Well thickness/nm	8	6.5	7.5
Barrier material	InP	$InGa_{0.3}As_{0.64}P$	$InGa_{0.29}Al_{0.18}As$
Barrier thickness/nm	10	10	10
Number of QWs	30	20	20
l_{PD}	20μm	20μm	20μm
w_{PD}	5μm	5μm	5μm
l_{ad}	2μm	2μm	2μm

from a cleaved single mode fiber to the single mode waveguide on the chip. The light is then evanescently coupled from the single-mode waveguide to the MQW p-i-n PD. The MQW p-i-n PD converts the optical signals into the electrical domain under a reverse bias voltage. After converting the optical input signal into the electrical domain, the RF output signal is coupled out of the chip via the integrated GSG RF pads. Fig. 31(b) shows the schematic diagram of the waveguide integrated MQW p-i-n PD. All the three designs have the same spot size converter, the same single mode waveguide, the same dimensions of the PD, and the same GSG RF pads. The length of the PDs of the three designs l_{PD} is 20μm which is about $1.5l_{pi}$. The width of the PDs of the three designs w_{PD} is 5μm. The length of the advanced waveguide of the three designs l_{ad} is 2μm. Fig. 31(c) shows the schematic diagram of the cross section of the MQW p-i-n PD mesa. The intrinsic MQW absorber layers of the three designs (*W5* layer in Fig. 31(c)) are listed in Table 3. Other layers of the three designs (*W1*-*W4* and *W6* layers in Fig. 31(c)) are optimized based on the model presented Section 3.2.1.

Design "InP"

Based on the MQW layers as listed in Table 3 and the corresponding physical parameters for $InGa_{0.47}As$/InP as shown in the Table 4, the absorption coefficient of the design "InP" can be obtained using the developed simulation program based on the model presented in Chapter 3. The parameters for the broadening factor are listed in Table 2. Fig. 32 shows the simulated absorption coefficients of the design "InP" over the C-band (1530nm – 1565nm) and the L-band (1565nm - 1620nm). It can be seen that due to the hh-e transition the exciton absorption peak is clearly resolved for TE with the electrical field up to 120kV/cm. The transit time τ, optical saturation power P_s, the internal quantum efficiency η_i for TE and TM, and the 3-dB bandwidth f_{3dB} are calculated at various electrical field strengths in Table 5. The optical saturation power is calculated with the calculated optical saturation intensity I_s and the area of the PD cross section of 5μm x 0.54μm. The 3dB bandwidth is calculated using Eq. (113). The 3dB bandwidth is mainly limited by the transit time. The carrier recombination time in MQWs is taken as 1.5μs in Eq.

(96) [44]. The large transit time of μs range is mainly caused by the large barrier heights ΔE_c and ΔE_v. Due to this large transit time, the internal quantum efficiency, the saturation photocurrent, and the bandwidth are limited. At low electrical field strength of 20kV/cm, the absorption efficiency η for TE and TM is only 0.32 and 0.43, respectively. By increasing the electrical field strength to 120kV/cm, the internal quantum efficiency for both TE and TM reaches 1 since the large electric field lowers the barrier height decreasing the carrier transit time. As a result, the total absorption efficiency increases. The large transit time on one hand reduces the transit time limited bandwidth and on the other hand increases the series resistance reducing the RC limited bandwidth. As a result, the 3dB bandwidth is limited as hundreds of kHz. In general, the performances of TM polarized input light are better than that of the TE polarized input light due to the shorter transit time of TM polarized input light which is contributed from the lh-e transition.
The epitaxial layers of the waveguide integrated MQW p-i-n PD design "InP" are listed in detail in Table 10 in Appendix. The light propagation of the waveguide integrated MQW p-i-n PD design "InP" for TE and TM polarization are shown in Fig. 33. It is clear that the TE polarized light is more strongly absorbed than the

Table 4 Parameters used in simulation of the absorption coefficient for $InGa_{0.47}As/InP$ MQW

Parameter	Symbol(unit)	$InGa_{0.47}As/InP$
Lattice constant	a(Å)	5.868/5.869
Bandgap	E_g (eV)	0.7519/1.35
Electron effective mass	m_e/m_0	0.053/0.095
Heavy-hole effective mass	m_{hh}/m_0	0.5091/0.56
Light-hole effective mass	m_{lh}/m_0	0.054/0.12
Conduction band offset	$\Delta E_c/\Delta E_g$ (eV)	0.4
Temperature	T (K)	300
Recombination time in MQWs	$\tau_{recombination}$	1.5μs

Table 5 Calculated transit time, optical saturation power, absorption efficiency η, and the transit time limited bandwidth of the design "InP" for TE and TM polarized input light of 0.3μW

	20kV/cm	40kV/cm	60kV/cm	80kV/cm	120kV/cm
τ(TE)	2 μs	0.83 μs	0.39 μs	0.15 μs	0.06 μs
τ(TM)	1 μs	0.4 μs	0.15 μs	0.038 μs	0.011 μs
P_s(TE)	4μW	10μW	24μW	74μW	200μW
P_s(TM)	19μW	40μW	93μW	370μW	1.28mW
η(TE)	0.32	0.49	0.7	0.9	0.95
η(TM)	0.43	0.62	0.84	0.99	1
f_{3dB}	270kHz	660kHz	1.4MHz	3.6MHz	9MHz

TM polarized light along the PD.

The simulated responsivities and PDL with different electrical field strengths are shown in Fig. 34 at the input optical power of 0.3μW. The simulated responsivity considers the coupling loss of 1dB from the single mode fiber to the spot size converter. The saturation absorption of CW input light is taken into consideration for the electrical field strength from 20kV/cm to 120kV/cm. It is clear that the responsivity for TE at 20kV/cm suffers from the low internal quantum efficiency and low optical saturation power reaching only 0.3A/W at 1550nm. The larger electrical field strength improves the internal quantum efficiency and saturation absorption leading to a larger responsivity at 1550nm. However, by further increasing the electrical field, the responsivity decreases due to the broadening of the exciton linewidth. Fig. 35 (a) plots the calculated PDL spectra according the

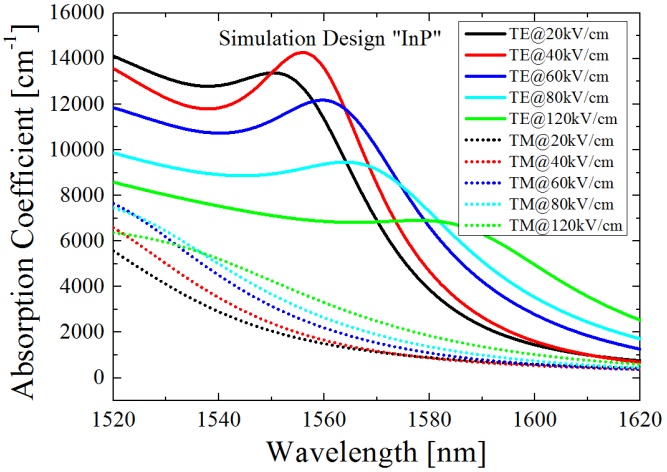

Fig. 32 The simulated optical absorption spectra of design-InP with the electrical field ranging from 20kV/cm to 120kV/cm (TE - solid curves, TM - dotted curves).

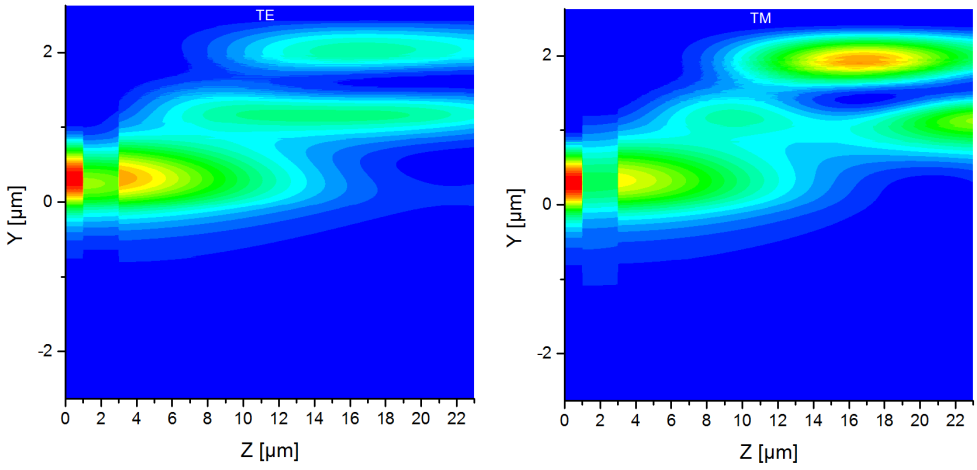

(a) (b)

Fig. 33 The simulated light propagation of the design “InP” for (a) TE and (b) TM.

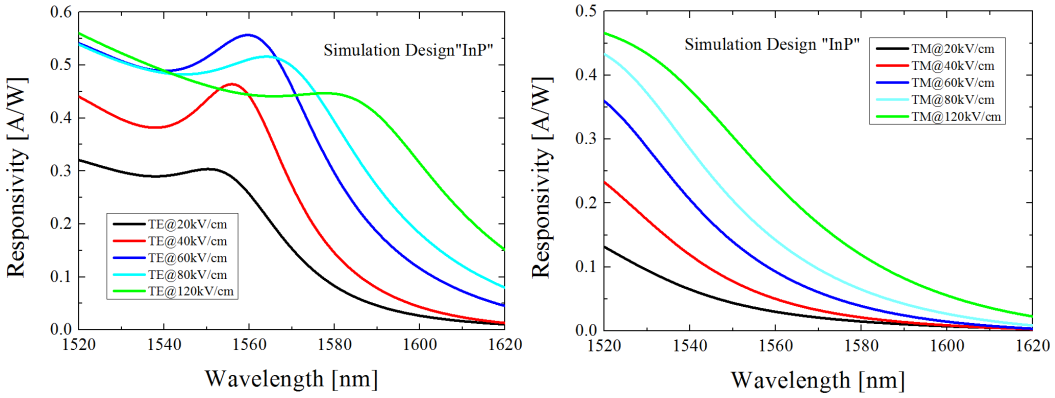

(a) (b)

Fig. 34 The simulated responsivity spectra of the design "InP" with the electrical field strength ranging from 20kV/cm to 120kV/cm for (a) TE and (b) TM.

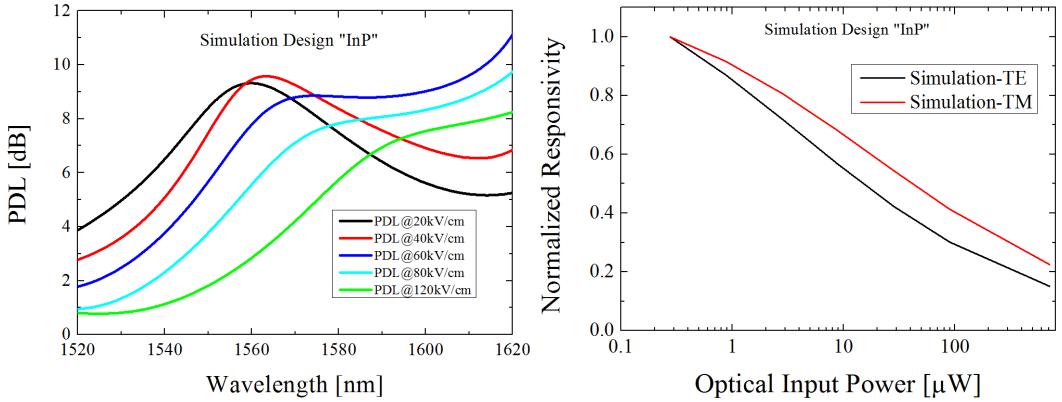

(a) (b)

Fig. 35 (a) The simulated PDL spectra of the design "InP" with the electric field ranging from 20kV/cm to 120kV/cm; (b) the normalized responsivity versus the optical input intensity for the modeling of a TE polarized input light (black), a TM polarized input light (red).

TE and TM responsivity with different electrical field strengths at the optical input power of 0.3μW. At 1550nm the PDL reaches 9dB at the electrical field strength of 20kV/cm and decreases to 1.5dB at the electrical field of 120kV/cm, since the TM responsivity increases to the level of the TE responsivity at the large electrical field strength.

Fig. 35 (b) shows the normalized responsivity versus the optical input power for the TE polarized input light with P_s=4μW and a=0.4 in Eq.(97) and the TM polarized input light with P_s=19μW and a=0.4 in Eq.(97). Because of the large transit time, the responsivity is strongly dependent on the optical input power.

In summary, the simulation results show that the performance of the design "InP" such as the saturation of optical absorption and the bandwidth are limited by its large transit time.

Design "Q1.33" and design "Al"

Since the responsivity, the saturation photocurrent, and the bandwidth of the design "InP" are limited by its large transit time, the design "Q1.33" and the design "Al" are introduced to achieve short transit time by using different barrier materials which are listed in Table 3. The physical parameters for $InGa_{0.47}As$/ $InGa_{0.3}As_{0.64}P$ and $InGa_{0.47}As$/ $InGa_{0.29}Al_{0.18}As$ are listed in Table 6. It is worth mentioning that the bandgap offset ratio between the barriers and wells for these two designs is different.

The absorption coefficients for the design "Q1.33" and the design "Al" are shown in Fig. 36 over the C- and L-band. For the design "Q1.33", the exciton absorption peak is clearly resolved for TE with the electrical field up to 60kV/cm while for design "Al" the exciton absorption peak for TE can be clearly resolved with the electrical field up to 80kV/cm. Since the performance of the TM polarized input

Table 6 Parameters used in simulation of the absorption coefficient for $InGa_{0.47}As$/ $InGa_{0.3}As_{0.64}P$ and $InGa_{0.47}As$/ $InGa_{0.29}Al_{0.18}As$ MQW

Parameter	Symbol (unit)	$InGa_{0.47}As$/ $InGa_{0.3}As_{0.64}P$	$InGa_{0.47}As$/ $InGa_{0.29}Al_{0.18}As$
Lattice constant	a(Å)	5.868/5.869	5.868/5.869
Bandgap	E_g (eV)	0.7519/0.9384	0.7519/0.9745
Electron effective mass	m_e/m_0	0.053/0.0671	0.053/0.0831
Heavy-hole effective mass	m_{hh}/m_0	0.509/0.5271	0.509/0.587
Light-hole effective mass	m_{lh}/m_0	0.054/0.0752	0.054/0.0842
Conduction band offset	$\Delta E_c/\Delta E_g$	0.4	0.72
Temperature	T (K)	300	300
Recombination time in MQWs	$\tau_{recombination}$	1.5μs	1.5μs

Table 7 The calculated transit time, saturation intensity, absorption efficiency, and 3dB bandwidth of the design "Q1.33" and the design "Al"

		20kV/cm	40kV/cm	60kV/cm	80kV/cm
τ(TE)	Design "Q1.33"	50 ps	35 ps	17 ps	9 ps
	Design "Al"	33 ps	22 ps	14 ps	8 ps
P_s(TE) W	Design "Q1.33"	0.1	0.15	0.3	0.6
	Design "Al"	0.12	0.18	0.3	0.52
η(TE)	Design "Q1.33"	1	1	1	1
	Design "Al"				
f_{3dB}	Design "Q1.33"	11GHz	16GHz	32GHz	61GHz
	Design "Al"	17GHz	25GHz	39GHz	68GHz

light are generally better than that of the TE polarized input light, only the electrical field dependent transit time τ, the optical saturation power, the internal quantum efficiency, and the 3dB bandwidth for TE are calculated as listed in Table 7. The transit time is reduced from the µs range of the design "InP" to the ps range for the design "Q1.33" and the design "Al" due to the reduced barrier height ΔE_c and ΔE_v. For the design "Q1.33", the transit time is mainly determined by the heavy hole. For design "Al", the transit time is determined by the electron due to the large conduction band offset ratio of 0.72 for the InGaAsP/InGaAlAs interface. Due to the short transit time, the performances regarding the internal quantum efficiency, the optical saturation intensity, and the bandwidth are improved. The absorption efficiency η for both designs equals 1 and is independent on the electrical field strength. The calculated optical saturation power for both designs reaches more than 100mW as listed in Table 7. It means that both designs don't suffer the saturation of optical absorption. Assuming that the series resistance is 10Ω, the 3dB bandwidth is mainly limited by the transit time which is over 10GHz at zero bias and increases to 63GHz for the design "Q1.33" and 68 GHz for the design "Al" by increasing the electrical field strength to 80kV/cm.

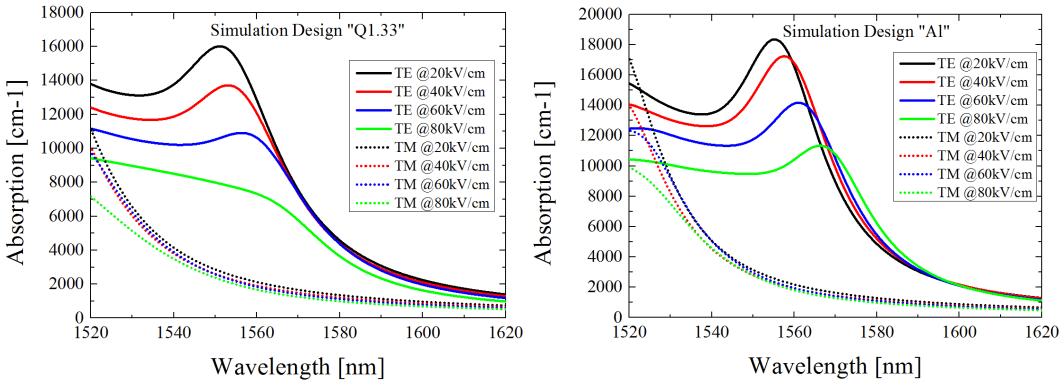

Fig. 36 The simulated optical absorption spectra with the electrical field ranging from 20kV/cm to 80kV/cm: (a) the design "InP"; (b) the design "Al" (TE - solid curves, TM - dotted curves).

The p-mesa and n-mesa layers for the waveguide integrated MQW p-i-n PD design "Q1.33" and design "Al" are optimized according to the light propagation simulation. The epitaxial layers of the both waveguide integrated MQW p-i-n PD designs are listed in Appendix Table 11 and Table 12, respectively.

The simulated responsivities for the design "Q1.33" and the design "Al" with different electrical field strengths are shown in Fig. 37. The simulated responsivity considers the coupling loss of 1dB from the single mode fiber to the spot size converter. Since the internal quantum efficiency for both designs equals 1, the responsivities at the low electrical field strengths are improved compared to that of the design "InP". The responsivities at 1550nm decrease with the electrical field strength for both designs because of the increasing exciton linewidth (broadening

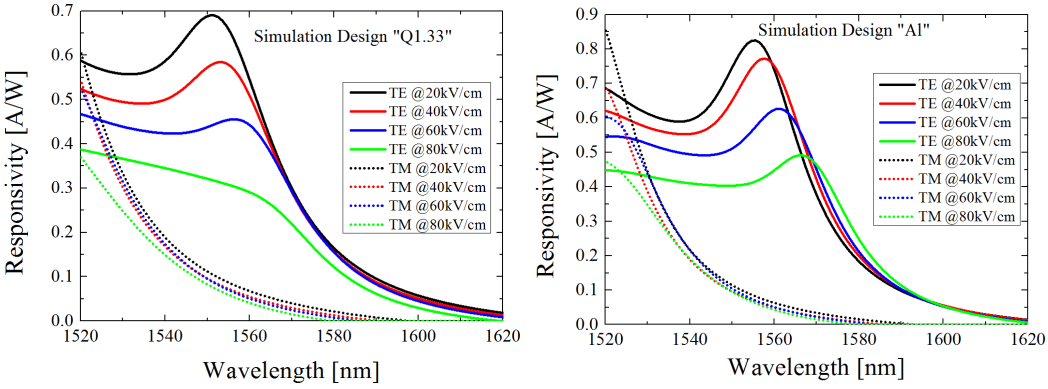

(a) (b)

Fig. 37 The simulated responsivity spectra with the electrical field strength ranging from 20kV/cm to 80kV/cm for (a) the design "Q1.33" and (b) the design "Al".

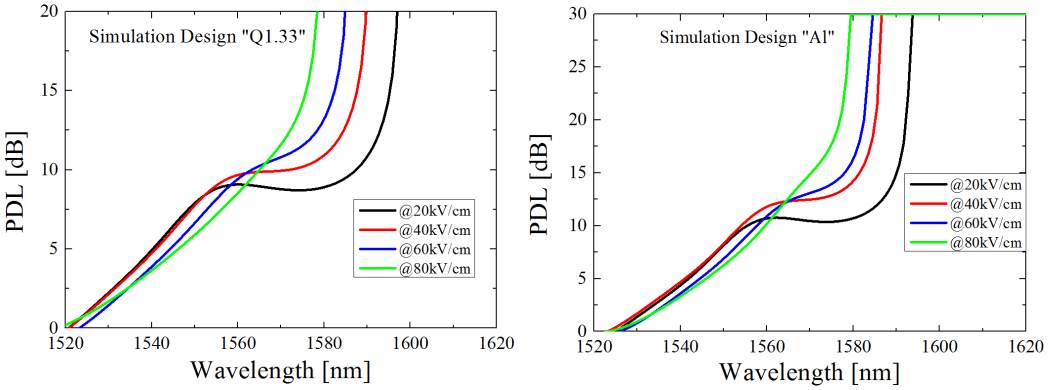

(a) (b)

Fig. 38 The simulated PDL spectra with the electric field ranging from 20kV/cm to 80kV/cm for (a) the design "Q1.33" and (b) the design "Al".

factor). At 1550nm, the responsivity for the design "Q1.33" decreases from 0.65A/W to 0.35A/W with the electrical field strength increasing from 20kV/cm to 80kV/cm. For the design "Al", the responsivity at 1550nm decreases from 0.7A/W to 0.4A/W with the electrical field strength increasing from 20kV/cm to 80kV/cm.

Fig. 38 plots the simulated PDL spectra for the design "Q1.33" and the design "Al" based on the TE and TM responsivity spectra shown in Fig. 37 with different electrical field strengths. For the design "Q1.33" at 1550nm the PDL reaches 8dB at the electrical field strength of 20kV/cm and decreases to 5dB at the electrical field of 80kV/cm. For the design "Al" at 1550nm the PDL reaches 7.5dB at the electrical field strength of 20kV/cm and decreases to 5dB at the electrical field of 80kV/cm.

In summary, because of the shorter transit time, the performances of the design "Q1.33" and the design "Al" such as the saturation of optical absorption and the bandwidth are improved compared to the design "InP".

4.2 Fabrication of waveguide integrated MQW p-i-n PDs

The epitaxial layers for the design “InP”, the design “Q1.33”, and the design “Al” as shown in Appendix Table 10, Table 11, and Table 12 are grown by a single metal organic vapor phase epitaxy (MOVPE) run on 3 inch semi-insulating InP substrate. The process steps are shown in Fig. 39 (a)-(d).

After the single step MOVPE, the P-metal is firstly evaporated on the surface. The active photodiode area is structured by Inductively Coupled Plasma (ICP) etching and wet chemical etching processes down to the N-contact layer using the P-metal as a mask. After that the N-contact is defined using standard lithography and ICP etching. The N-metal is deposited and tempered. The waveguide is formed using ICP as shown in Fig. 39 (d). Photoresist and SiN_x serve as etching masks. To form the electrical contacts and generate the on-chip bias circuits using air-bridges, gold-electro-plating was applied. For passivation, a layer of Benzocyclobuten (BCB) is spun on the entire wafer with the opening at the P- and N-contacts. Finally after cleaving, the wafer is anti-reflection coated by sputtering TiO_x layers on the facet to reduce the insertion loss and to avoid back reflection into the local oscillator. The optical return loss of the chip was measured below -35dB over the entire C- and L-band.

The measured photoluminescence (PL) curves for the 3 MQW layer designs are plotted in Fig. 40. The center wavelength is 1558nm for the design “InP”, is 1556nm for the design “Q1.33”, and is 1535nm for the design “Al”. The measured well thickness for the design “InP”, the design “Q1.33”, and the design “Al” is 8.2nm, 6.5nm, and 6.5nm, respectively. The center wavelengths for the design

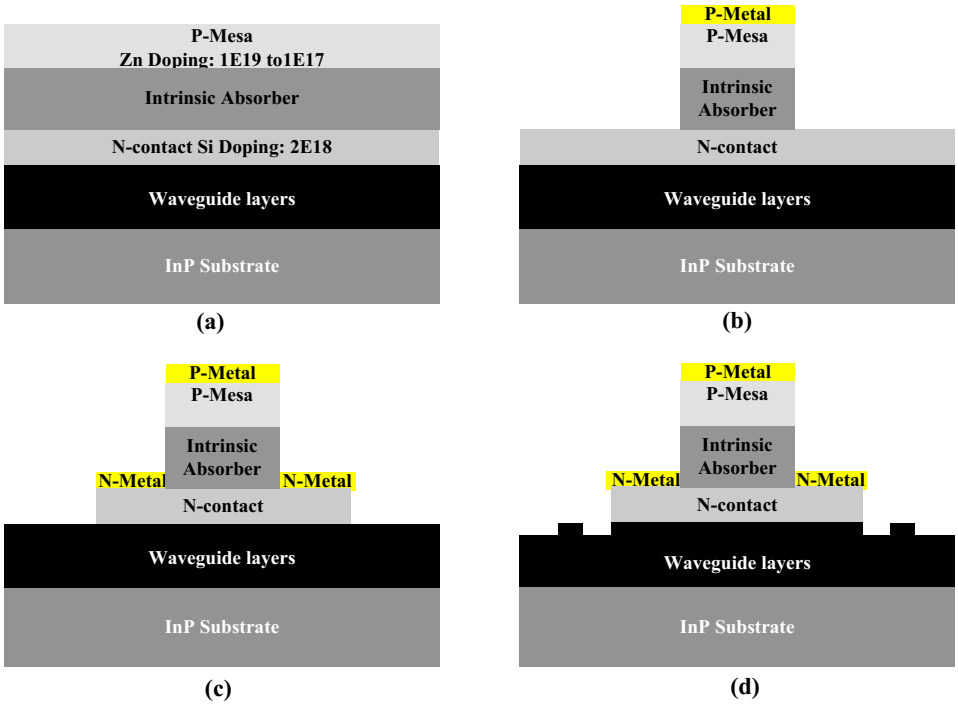

Fig. 39 Fabrication flow of the waveguide integrated MQW p-i-n PDs.

"InP" and the design "Q1.33" agree well with the simulation results as shown in Fig. 32 and Fig. 36. It is worth mentioning that the fabricated well thickness of design "Al" is 1nm smaller than the designed value of 7.5nm. As a result, the center wavelength of the design "Al" shifts to shorter wavelength compared to the simulation result and the peak of the photoluminescence is higher because of the stronger exciton confinement in wells. In Fig. 41 and Fig. 42, a micrograph and a SEM picture of the fabricated photodiode chip are shown, respectively.

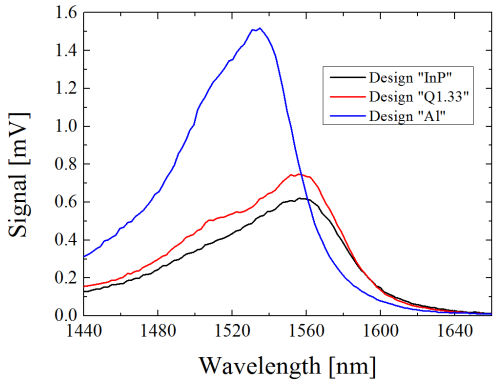

Fig. 40 The measured photoluminescence spectra of the fabricated epitaxial layers of the design "InP" (black curve), the design "Q1.33" (red curve), and the design "Al" (blue curve).

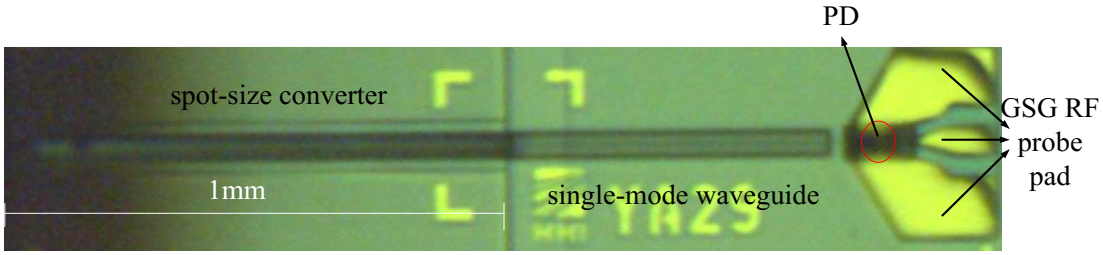

Fig. 41 Micrographs of the fabricated complete waveguide integrated MQW p-i-n PD chip including the detailed views.

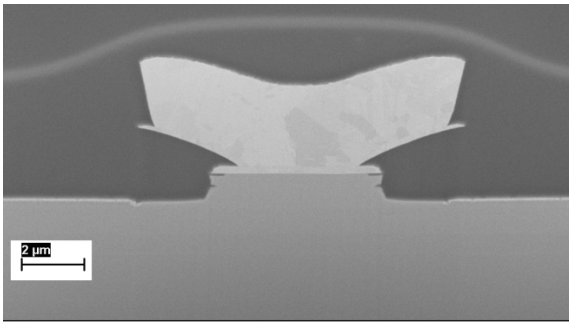

Fig. 42 SEM picture of the cross-section of the MQW p-i-n PD.

5. Device Characterization

In this chapter the fabricated waveguide integrated MQW p-i-n PDs of the 3 designs are characterized in terms of the dark current, the responsivity, the PDL, the DC saturation of optical absorption, the bandwidth, the maximum RF output power, and the nonlinearity.

5.1 DC characterization

5.1.1 Dark current

The I-V curves of the three MQW p-i-n PD designs are measured without illumination on the chip level as shown in Fig. 43(a). The absolute current in plotted in log-scale for clarification. For reverse biases, the design "InP" shows the smallest dark current which increases slightly to 0.1nA at -4V. The transit time for the design "InP" is in the range of µs resulting in a small reverse saturation current I_0 and a low dark current according to Eq. (101). The PD chip of the design "Q1.33" has the dark current of 0.3nA with the reverse bias voltage up to -4V while the PD chip of the design "Al" has the dark current of 8nA with the reverse bias voltage up to -4V mainly due to some process irregularities. The measurement results agrees well with the theories presented in Section 3.3 that the large transit time reduces the dark current.

In general, the design "Q1.33" and the design "Al" show much higher forward currents than the design "InP", as shown in Fig. 43 (b). Their ps-range transit time generates the small series resistances resulting in their high forward currents according to Eq. (102)-(104). At low current injection for the forward current, an ideality factor of 1.4 for the design "Q1.33" and the design "Al" is derived which indicates a combination of the recombination and diffusion current. For the design

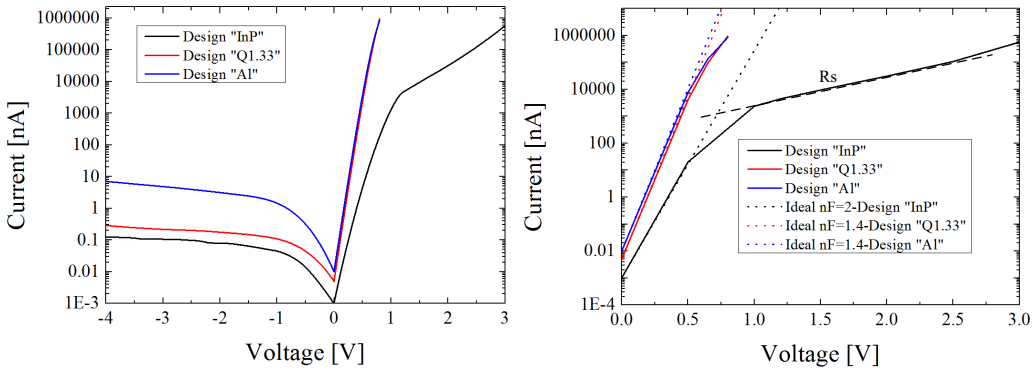

Fig. 43 (a) I-V characteristics of the fabricated waveguide integrated MQW p-i-n PDs; (b) I-V characteristics at the forwards bias voltage condition black; solid curves: measurement results; dotted curves: fitted ideal exponential curves.

"InP" an ideality factor of 2 can be obtained which indicates a dominance of the recombination current.
At high current injection, the forward current of the design "InP" chip is mainly limited by the large series resistance which is about 1MΩ because of the µs-range transit time according to Eq. (104). For the design "Q1.33" chip and the design "Al" chip, the forward currents at high current injection are limited by the contact resistance of about 10Ω.

5.1.2 Experimental setup

The responsivity, the PDL, and the DC saturation absorption of the three samples are measured using the measurement setup as depicted in Fig. 44. A tunable laser (Keysight 81960A) is used for the CW light source. The wavelength of the input light can be swept from 1520nm to 1620nm (the whole C- and L-Band). A polarization controller (Keysight N7786B) is used for setting the polarization status (TE and TM) of the input light. A variable optical attenuator (VOA) (Keysight 81571A) and an erbium-doped fiber amplifier (EDFA) are applied to tune the optical input power. The input light is butt-coupled to the PD chips (device under test (DUT)) using a cleaved single-mode fiber. The optical input power is monitored using an optical power meter (Keysight N7744A). At the output a source meter (Keithley 2602B) is used to supply the PD with a voltage from 0V to -8V and to monitor the converted photocurrent.
The spot size converter and the passive single-mode waveguide are supposed to have a PDL of 0dB over the wavelength. The measured optical loss considering the light coupling loss from a cleaved fiber to the spot size converter and the light propagation loss in the passive waveguide adds up to approximately 1dB over the wavelength.

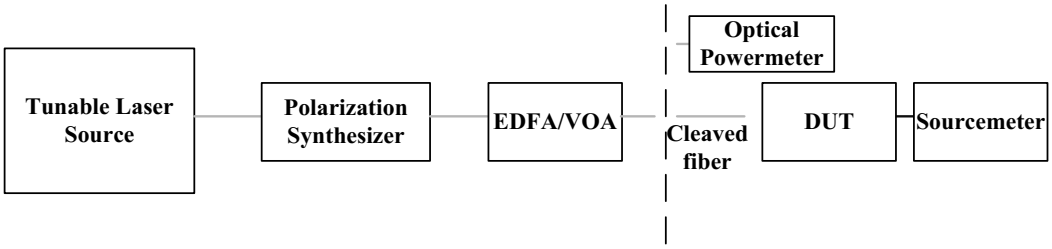

Fig. 44 Experimental setup for optoelectronic CW measurements; gray line: optical connection; black line: electrical connection; dashed line: input power reference plane.

5.1.3 Responsivity, PDL, and DC saturation

Design "InP"

Coupling the light with the wavelength ranging from 1520nm to 1620nm and the power of 0.3µW into the device, the measured responsivity spectra of the design

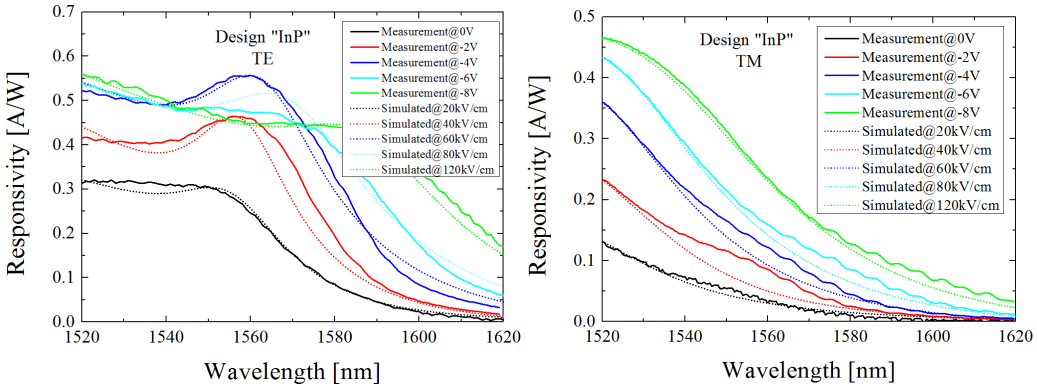

(a) (b)

Fig. 45. Measured responsivity spectra with the voltage ranging from 0V to -8V with a (a) TE and (b) TM polarized input light with an input light power of 0.3μW, compared to the simulated responsivity spectra from Fig. 34.

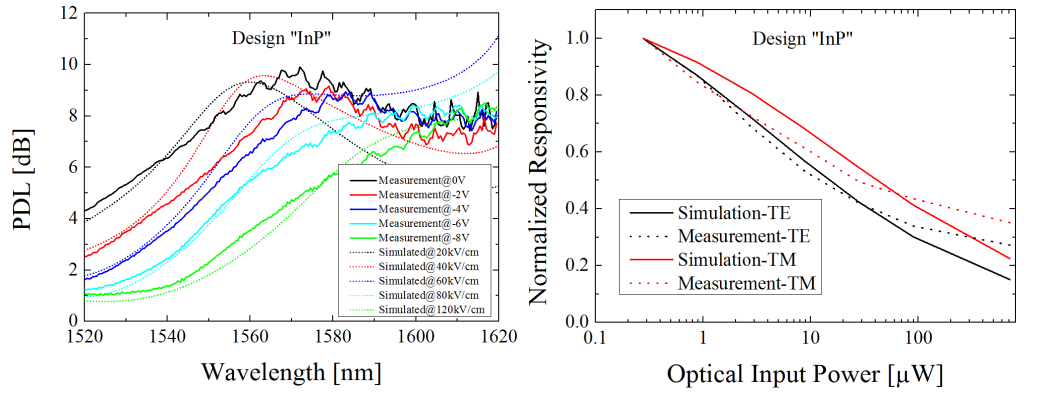

(a) (b)

Fig. 46. (a) Measured PDL spectra with the voltage ranging from 0V to -8V compared to the simulated PDL spectra from Fig. 35(a); (b) The normalized responsivity versus the optical input power; solid curves for the modeling of a TE polarized input light with Ps=4μW and a=0.4 (black), a TM polarized input light with Ps=19μW and a=0.4 (red), dotted curve for the measurement results of the TE polarized input light (black), the TM polarized input light (red).

"InP" chip are shown in Fig. 45 (a) for the TE polarization and in Fig. 45 (b) for the TM polarization at the revise bias from 0V to -8V. The responsivity is calculated by dividing the photocurrent by the optical input power including the coupling loss and the single-mode waveguide loss which add up to 1dB. The fabricated design "InP" chip has a low responsivity at low inverse voltages, suffering from its low absorption efficiency due to the large transit time. Increasing the inverse voltage the transit time decreases and the absorption efficiency increases. Moreover, the exciton absorption peak for the TE polarization and the QCSE can be clearly seen. The absorption peak shifts to

longer wavelength (red shift) with the larger inverse voltage. For the TM polarization, the responsivity decreases gradually with increasing the input light wavelength, since the light-hole to electron transit occurs below 1520nm at an inverse voltage up to -8V. Thus, a large PDL is obtained (Fig. 46). Comparing the measurement results with the simulation results an excellent agreement between simulation and measurement can be observed.
The responsivity is measured by varying the optical input power from 0.1μW to 1mW for the TE and TM polarization at -2V as shown in Fig. 46(b). In Fig. 46(b) the solid curves denote the measured responsivity versus the different input light powers while the dotted curves are the simulated results taken from Fig. 35 (b). The responsivity decreases by increasing the input light power for both TE and TM polarization. Because of the large carrier transit time, the large number of the free carriers produced by the large input light power cause the saturation of the light absorption. The obtained saturation optical input power P_s for TE polarized light at -2V is 7.5μW while the saturation optical input power P_s for TM polarized light at -2V is 35μW. The measurement results agree well with the simulated values as listed in Table 5 and the deviation appears at large input light intensity.

Design “Q1.33” and design “Al”

The responsivity of the design “Q1.33” chip and the design “Al” chip are measured with the TE and TM polarized input light. Fig. 47 and Fig. 48 show the responsivity and the derived PDL over whole C- and L-band for the design “Q1.33” and the design “Al”, respectively. The optical input power is set to be 1mW.
The measured responsivity for the TE and TM polarized input light shows the same trend compared to the simulation results as shown in Fig. 37 and Fig. 38. At the wavelengths below the wavelength of the measured PL peaks, both designs show a responsivity of about 0.5A/W which matches the simulated results. The QCSE is clearly seen in the measurement results. The large reverse bias voltage shifts the absorption peak to the large wavelength. Moreover the PDL decreases with the reverse bias voltage because of the increasing responsivity of TM with the reverse bias voltage.
However compared to the simulation results there are no excitonic absorption peaks for both designs in the measurement. The responsivity spectra for both TE and TM polarized input light are broader than the simulation results. The broadening is caused by the weak confined excitons in the wells due to the small bandgap discontinuum ΔE_g. The weak confined excitons lead to the increasing exciton broadening factor of $\Gamma_{ex,lh\text{-}e}$ and $\Gamma_{ex,hh\text{-}e}$. With the large exciton broadening factor of $\Gamma_{ex,lh\text{-}e}$ and $\Gamma_{ex,hh\text{-}e}$, the responsivity of TE and TM polarized input light is broadened leading to a lower PDL compared to the simulation results in in Fig. 47(b) and Fig. 48(b). And the responsivities near the PL wavelength for both

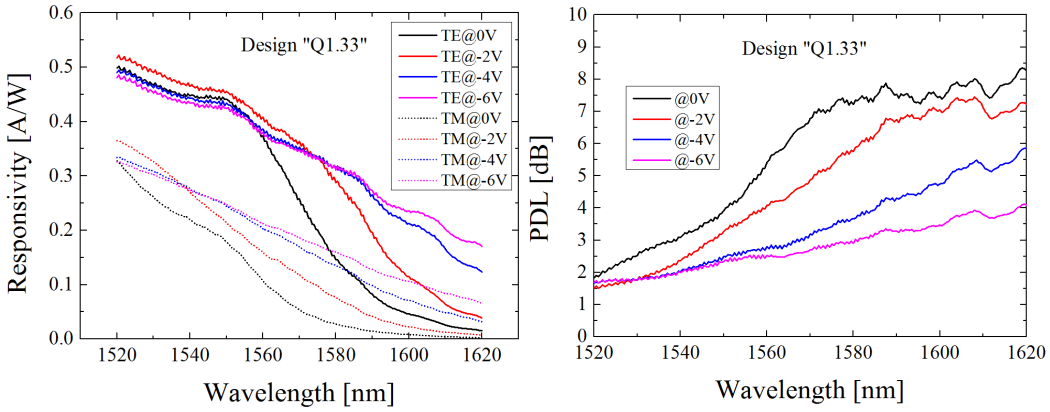

(a) (b)

Fig. 47 (a) The measured TE (solid curves) and TM (dotted curves) responsivity spectra; (b) the measured PDL of the fabricated MQW p-i-n PD of the design "Q1.33" with the voltage ranging from 0V to -6V for an input light power of 1mW.

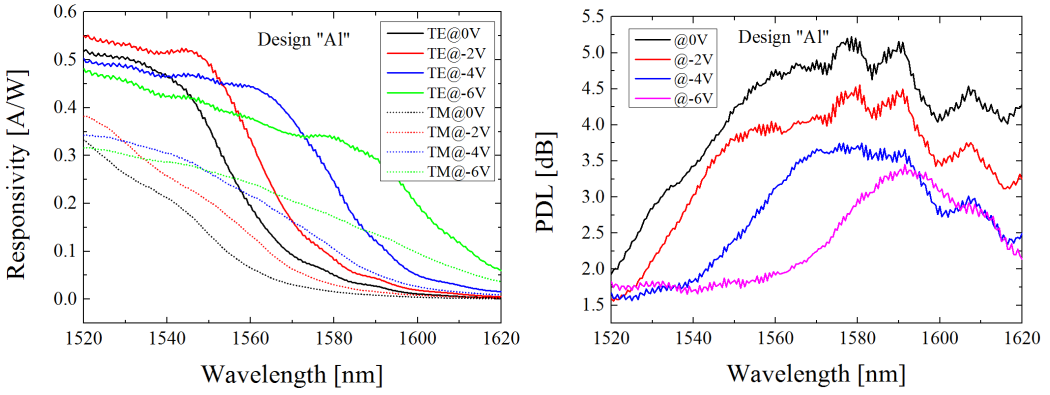

(a) (b)

Fig. 48. (a) The measured TE (solid curves) and TM (dotted curves) responsivity spectra; (b) the measured PDL of the fabricated MQW p-i-n PD of the design "Al" with the voltage ranging from 0V to -6V for an input light power of 1mW.

designs are lower than the simulated results. It is worth mentioning that the absorption peak for the design "Al" occurs at lower wavelength compared to the simulation results. It is caused by the reduced thickness of the fabricated well of the design "Al which is 1nm thinner than the designed value of 7.5nm.

The responsivities for both designs are measured by varying the optical input power from 1mW to 60mW for TE and TM polarization at different reverse bias voltages as shown in Fig. 49. At a low bias voltage of -1V, both designs suffer the DC saturation absorption due to the relative small saturation CW optical power of about 100mW. The large reverse bias voltage increases the linearity of the DC response. For both designs, the PDs are in the linear region with the DC photocurrent up to 60mA at the high bias voltages of -2V and -3V which agrees

well with the simulation results. The calculated saturation CW optical power is about 300mW at -2V and >500mW at -3V thanks to their ps-range carrier transit time.

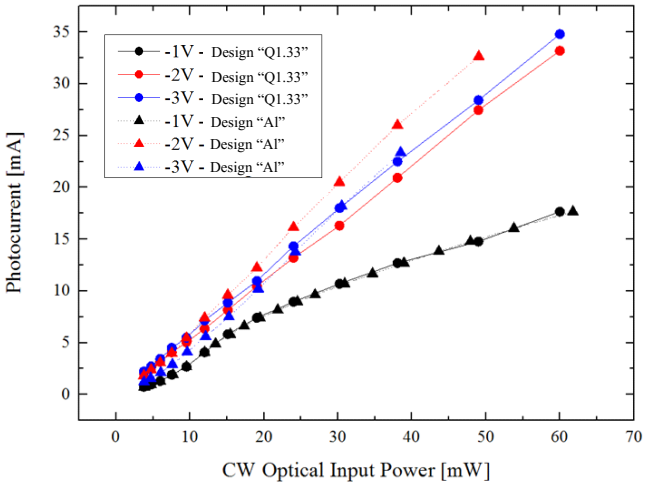

Fig. 49. DC photocurrent versus CW optical input power at various reverse bias voltages; solid curves (circle): the design "Q1.33"; dotted curves (rectangle): the design "Al".

5.2 RF characterization

5.2.1 Experimental setup

The O/E heterodyne setup is used for the measurement of the RF response and the RF saturation. The principle of the optical heterodyne detection is based on the nonlinear relation between the incident electromagnetic fields of the two CW laser sources with different carrier frequencies. The mixed signal is detected by the photodetector as the RF signal with the corresponding frequency of f_1. By tuning the f_1, the RF response can be measured from 0GHz to 110GHz (or even higher frequencies). Fig. 50 shows the measurement setup. The laser signals are provided by two tunable laser sources (Keysight 81960A) followed by two polarization controllers (Keysight N7786B) and two fiber-based 3dB-couplers. Laser 1 is set at the wavelength of 1550nm and to be TE polarized using polarization synthesizer 1. Laser 2 is tuned to provide variable wavelengths for the frequency sweep. The two laser signals are combined using a fiber-based 3-dB coupler. The optical powers and the wavelengths of the two laser signals are monitored by an optical power meter (Keysight N7744A) and a wavelength meter, respectively. To get 100% modulation depth, the two laser signals are set with the same optical input power and with the same state of polarization. The optical power of the mixed optical signal can be adjusted from -40dBm to 23dBm range using an EDFA and a VOA. The mixed optical signal is coupled into the DUT via a cleaved single-mode fiber. At the output side, the DUT is contacted with a high-frequency coplanar probe

head (Cascade Infinity Probe i110 G-S-G-100). A source meter serves as the DC voltage supplier and the monitor of the DC photocurrent. The RF electrical output power is detected with a calibrated electrical microwave power meter (R&S NRP2). After calibrating the effects of the microwave components (RF probe, bias-T), the RF output power can be obtained.

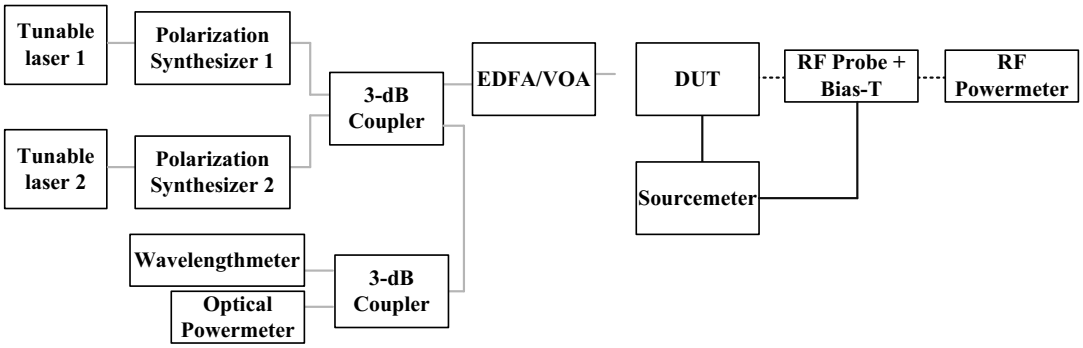

Fig. 50. Setup for O/E heterodyne measurements. Gray line: optical connection; solid black line: DC electrical connection; dotted black line: RF electrical connection.

5.2.2 Measurement results of the RF response

By sweeping the wavelength of the tunable laser 2 from 1550nm to

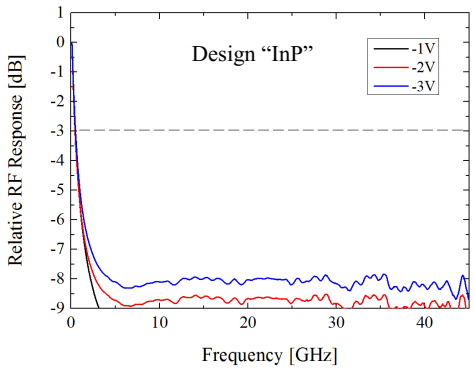

Fig. 51. Relative RF response of design-InP with different reverse bias voltages.

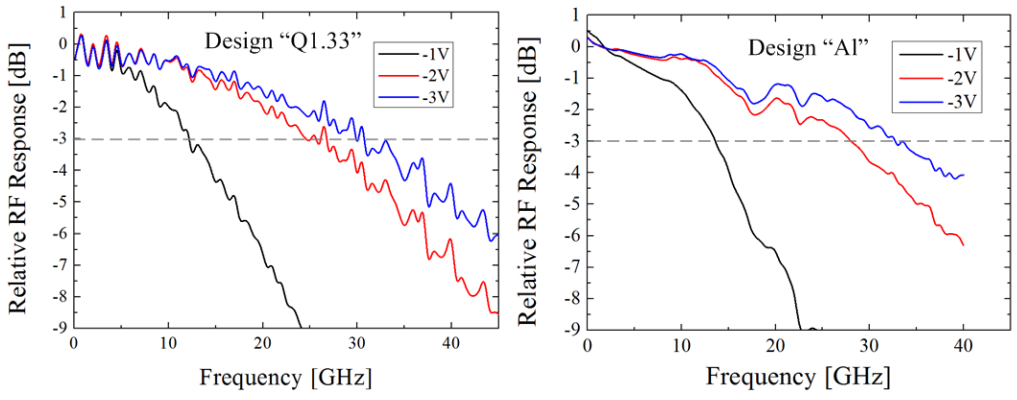

(a) (b)

Fig. 52. Relative RF response of (a) the design "Q1.33" and (b) the design "Al" with the bias voltages ranging from -1V to -3V.

1550nm+67GHz, the relative RF responses of the fabricated PD chips for the design “InP”, the design “Q1.33”, and the design “Al” are measured with an input light power of 1mW. Fig. 51 shows the relative RF response of the design “InP” chip with the bias voltage of 0V to -5V. The measured 3-dB bandwidth is only in the order of hundred MHz which is limited by its large µs-range transit time. By increasing the reverse bias voltage, the 3-dB bandwidth increases slightly. The difference between the measured 3-dB bandwidth and the simulation results in Table 5 is due to the measurement accuracy because the start frequency of the two laser heterodyne measurement setup is 100MHz which is already larger than the calculated bandwidth.

Fig. 52 (a) and Fig. 52 (b) show the measured relative RF response of the design “Q1.33” and the design “Al” at the bias voltage of -1V, -2V, and -3V. The ps-range transit time of the design “Q1.33” and the design “Al” increases their 3-dB bandwidths to the tens GHz range. The measurement results agree well with the simulated results as shown in Table 7. The 3-dB bandwidth at -1V is 12.5GHz for the design “Q1.33” and 14GHz for the design “Al”. For both designs, a large reverse bias voltage increases the 3-dB bandwidth. At the bias voltage of -2V, the 3-dB bandwidth for the design “Q1.33” is 25GHz and for design-Al is 28.5GHz. At the bias voltage of -3V, the 3-dB bandwidth for the design “Q1.33” is 30GHz and for the design “Al” is 34GHz. It is worth mentioning that at the bias voltages ranging from -1V to -3V the bandwidth of both designs is mainly limited by the transit time.

5.2.3 Measurement results of RF saturation effects

At high optical input power, the RF output power is limited due to a few physical effects such as the space-charge effect and heating. The space-charge effect is caused by the spatial distribution of the photo-generated carriers in the depletion region. At a large optical input power, the electrical field generated by the free carriers opposes the electrical field induced by the bias voltage and cannot be ignored. The total electrical field can collapse and the carrier transit time increases significantly leading to the compression of the RF output power. In this subchapter, the RF saturation effects of the design “Q1.33” and the design “Al” are characterized. Design “InP” is not measured due to its poor RF performance (3-dB bandwidth of hundreds KHz).

By varying the mixed optical input power from 0dBm to 18dBm, the electrical RF output powers for the design “Q1.33” and the design “Al” versus optical input power are shown in Fig. 53. The measured frequency is 10GHz. For both designs, the maximal RF output power increases with the reverse bias voltage. At -1V, the maximal RF output power for both designs is limited by their relative large transit time. At -3V, the design “Q1.33” and the design “Al” show a high maximal output

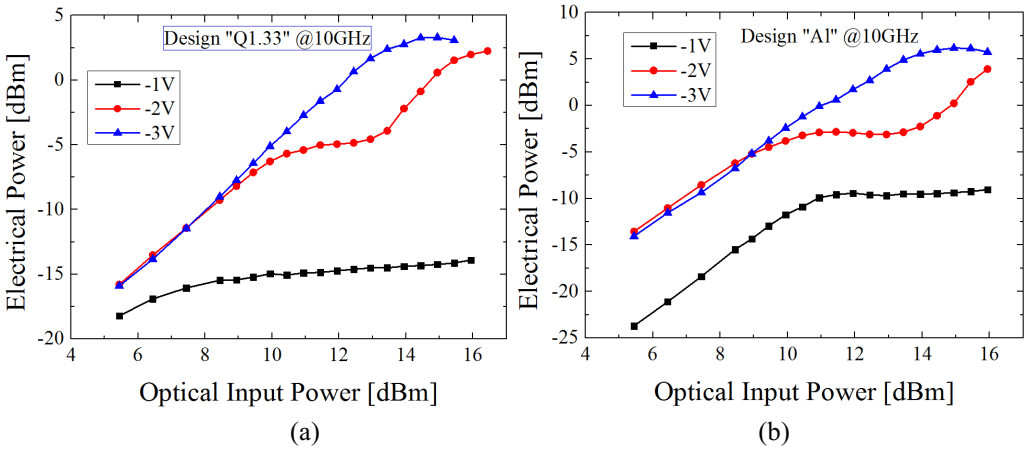

Fig. 53. Detected electrical RF output power of (a) the design "Q1.33" and (b) the design "Al" versus optical input power at different reverse bias voltages at the frequency of 10GHz.

power of 3.3dBm and 6.2dBm, respectively. Both designs show a high linearity with the optical input power up to 14dBm at -3V.

The decrease of the RF output power at high optical input power results from the reduction of the electrical field in the depletion region leading to a larger transit time. The reduction of the electrical field at high optical input power is mainly due to the voltage drop at the series resistance and the space-charge effect. Moreover, with high optical input power part of the depleted region is not fully depleted which increases the capacitance resulting in poorer RF performances. It is worth mentioning that at -2V for both designs the RF output power saturates firstly at the optical input power level of about 11dBm and increases further with the optical input power. The reason can be that by increasing the optical input power an increasing number of hot carriers in the quantum wells help the carriers to transit through the barriers resulting in a shorter transit time.

5.2.4 Measurement results of nonlinearity

The third-order output intercept point (OIP3) is usually used to quantify nonlinearities in PDs, since the frequencies of the third-order intermodulation distortions are close to the fundamental modulation frequencies. Using a four-laser optical heterodyne setup as shown in Fig. 54, the OIP3 values are measured. Laser 1 is set at the fixed frequency of 194THz with the wavelength of 1550nm. Laser 3 is set at the fixed frequency of 193THz with the wavelength of 1555nm. The frequency of laser 2 is swept from 194THz to 194THz+f_1, where f_1 is the measured frequency for the electrical signal. The frequency of laser 4 is swept from 193THz to 193THz+f_2, where f_2=f_1+0.5GHz. All the four lasers deliver the same power level of 1mW and the same polarization of TE. The laser set 1 (laser 1 and laser 2) is used to obtain the electrical signal with the frequency of f_1 while the laser set 2 (laser 3 and laser 4) is used to get the electrical signal with the

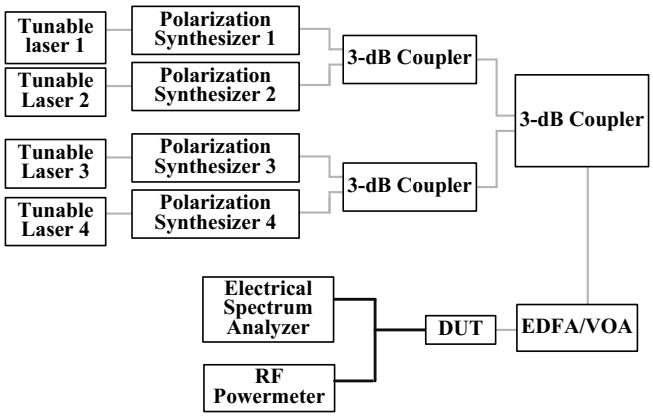

Fig. 54. Setup for O/E heterodyne measurements for OIP3 values, gray line: optical connection; solid black line: DC electrical connection; dotted black line: RF electrical connection.

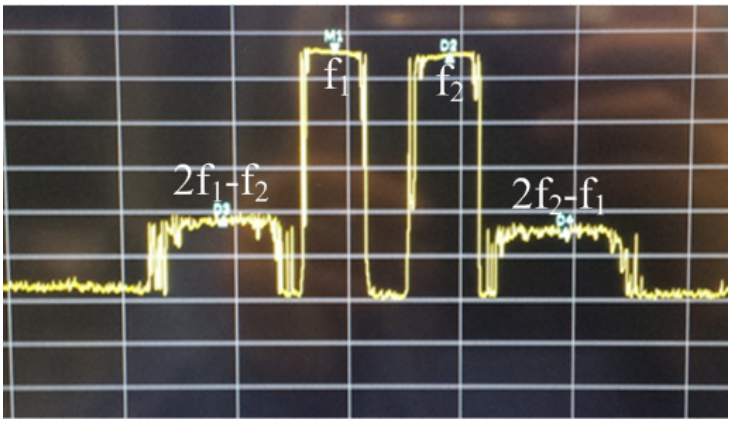

Fig. 55. Schematic spectrum of the detected RF output power of the measured PD in the electrical spectrum analyzer.

frequency of f_2. The power of the electrical RF signal with the frequency of f_1 and with the frequency of f_1 is the same which is proportional to the CW optical input power mP_0, where m is the modulation ratio. Thus, the RF power can be varied by the modulation ratio which can be set from 1 to 0 by changing the polarization of the laser 1 and laser 3 simultaneously. The RF output power of the measured PD chips is monitored by an electrical spectrum analyzer. Fig. 55 shows a schematic spectrum of the detected RF output signal. The detected RF signals consist of two fundamental signals with the frequency of f_1 and f_2, respectively, and two third-order harmonic signals with the frequency of $2f_1$-f_2 and $2f_2$-f_1, respectively. The calculation of the OIP3 values is schematically shown in Fig. 56. For the measurement, the RF input power is changed by the modulation ratio. The power of the fundamental signal and the third-order harmonic signal is measured with different modulation ratios. The OIP3 is a theoretical point at which the third-order harmonic signal amplitudes equal the input signals.

The measured OIP3 values versus the DC photocurrent at the frequency of f_1=10GHz for the design “Q1.33” and the design “Al” are shown in Fig. 57(a) and

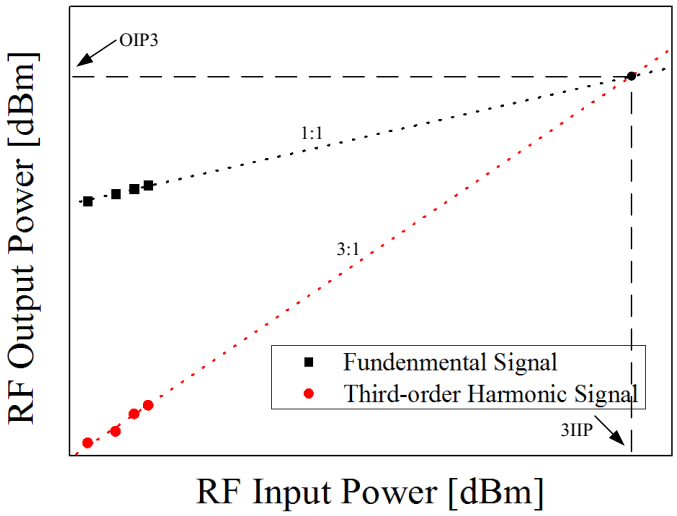

Fig. 56. Schematic calculation of third-order output interception point and third-order input interception point. Circle and square: measured points of the fundamental signal and third-order harmonic signal. Dotted curves: the fitted curves.

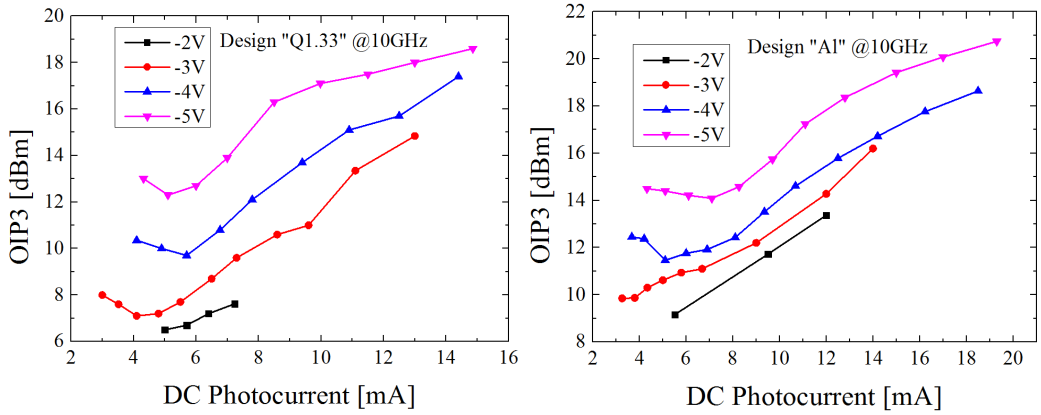

Fig. 57. Measured OIP3 value at 10GHz as function of DC photocurrent (a) the design "Q1.33" and (b) the design "Al".

Fig. 57(b), respectively. High reverse bias voltages increase the linearity for both designs. The reason is that at high reverse bias voltage condition, the parameters of the PD have weak dependence on the bias voltage and CW optical input increasing the linearity (OIP3 value). Furthermore, from Fig. 57 the OIP3 values for the design "Q1.33" and the design "Al" decrease with the DC photocurrent. By further increasing the DC photocurrent, the OIP3 values for the both designs increase. It can be explained based on the nonlinearity model presented in Section 3.4.3. Since the bandwidth of design "Q1.33" and design "Al" is mainly limited by the transit time, the OIP3 values should follow the trend of the linear coefficient of the carrier transit time $\frac{1}{b_\tau{}^2 a_{3,\tau}}$. And the linear coefficient of the carrier transit time $\frac{1}{b_\tau{}^2 a_{3,\tau}}$ decreases firstly with the DC photocurrent to reach its minimum. By further

increasing the DC photocurrent, $\frac{1}{b_\tau{}^2 a_{3,\tau}}$ for both designs increase. Therefore, the changes of OIP3 values of the both designs with the DC photocurrent are "v" formed as shown in Fig. 57.

In summary, for both PDs, the nonlinearity is mainly caused by the strong dependence of the carrier transit time on the bias voltage and the optical input power. By optimizing the epitaxial structure and the layout of the PD to a bandwidth being mainly limited by the RC time constant, the linearity can be improved and its photocurrent dependence can be reduced.

5.3 The new design

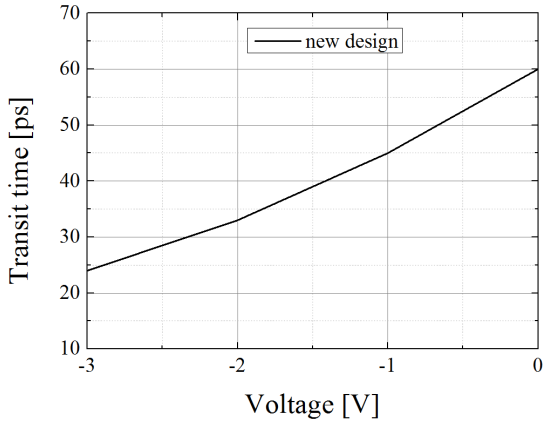

Fig. 58. Calculated transit time of the new design with the bias voltage from 0V to -3V

In summary of the three presented designs (the design "InP", the design "Q1.33", and the design "Al"), the design "InP" provides a higher PDL and a lower dark current. However, the design "InP" suffers its DC and RF saturation absorption with a limited 3-dB bandwidth of only hundreds of MHz caused by its µs-range transit time. In general, the DC and RF performances of the design "Q1.33" and the design "Al" are similar due to their comparable transit time. They provide much better DC saturation absorption and RF performances including the 3-dB bandwidth, the RF saturation power, and the linearity due to the ps-range transit time. However, their PDL is limited due to the absence of excitonic absorption.

There is one question: can you have a waveguide integrated MQW p-i-n PD design combing the high-PDL performance of the design "InP" and the high-RF performance of the design "Q1.33" and the design "Al"? According to the presented model, the answer is "yes". It is predicted in Section 2.3 that the PDL can be increased by introducing compressive strains in the MQW layers.

A new design of the waveguide integrated MQW p-i-n PD is presented which consists of 20, 3.5nm thick $InGa_{0.43}As$ wells with -0.26% strain separated by 10nm thick 0.091%-strained $InGa_{0.35}As_{0.73}$ barriers. The other layer stacks are optimized for optimal optical coupling and RF performances. The epitaxial layers are listed

in Table 14 in Appendix. All layers except the barriers and wells are lattice matched to InP. The wells are compressive-strained and the critical thickness h_c is calculated to be only 45nm. To get a thicker MQW layers and a good growth quality of the MQW layers, the barriers are designed to be tensile-strained. The length of the PDs of the three designs l_{PD} is 20μm. The width of the PDs of the three designs w_{PD} is 5μm. The length of the advanced waveguide of the three designs l_{ad} is 2μm. The calculated transit time is shown in Fig. 58. The simulated responsivity and PDL are shown in Fig. 59 and Fig. 60. It can be seen that the transit time for the new design is below 40ps even for zero-biasing condition. It predicts that the internal quantum efficiency equals 1 and the new design should have good RF performances regarding the bandwidth and the RF saturation.

By introducing strains in the MQWs, the new design combines the high-PDL performance of the design "InP" and the good RF performances of the design "Q1.33" and the design "Al". The new design with the improved PDL can be used in various applications such as polarization-diversity coherent optical receivers.

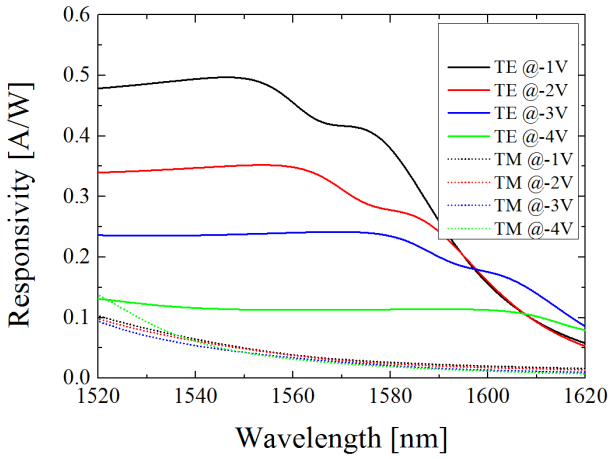

Fig. 59. Calculated responsivity of the new design with the bias voltage from -1V to -5V; solid curves: TE polarized input light; dotted curves: TM polarized input light.

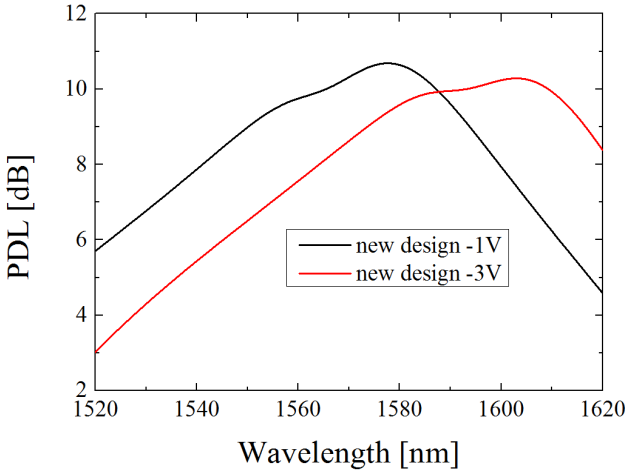

Fig. 60. Calculated PDL of the new design with the bias voltage of -1V and -3V.

In the end, the measured dark current, responsivity, PDL, 3-dB bandwidth, DC and RF saturation, and linearity of the design “InP”, the design “Q1.33”, and the design “Al” are summarized in Table 8. Table 8 lists the predicted DC and RF performances of the new design as well.

Table 8 The measured responsivity, PDL, bandwidth, DC and RF saturation absorption, and OIP3 of the design “InP”, the design “Q1.33”, and the design “Al”; the simulated DC and RF performances of the new design at different reverse biases

Parameter	Voltage [V]	Design “InP”	Design “Q1.33”	Design “Al”	New design
Dark current [nA]	-2	0.08	0.18	3.2	-
	-4	0.12	0.28	7	-
Responsivity [A/W] @ 1550nm	-2	0.45	0.45	0.49	0.35
	-4	0.53	0.43	0.46	0.12
Responsivity [A/W] @ 1570nm	-2	0.35	0.36	0.16	0.32
	-4	0.48	0.35	0.37	0.11
PDL @1550nm	-2	5.8	3.3	3.7	7.6
	-4	5	2.5	2.4	3.4
PDL @1570nm	-2	8.7	4.8	4.1	9.3
	-4	7.8	3.2	3.7	5.7
DC saturation optical input power [mW]	-2	7.5e-3	>60	>60	>60
	-4	6.5e-2	>60	>60	>60
RF maximal electrical output power [dBm]	-1	-	-13.9	-9	-
	-3	-	3.1	5.75	-
3-dB bandwidth [GHz]	-1	<1	13	14	17
	-3	<1	30	34	37
Maximal OIP3 [dBm]	-2	-	7.6	13	-
	-4	-	17.4	18.6	-

6. Advanced Receiver Concepts Using Waveguide Integrated MQW pin PDs

6.1 Conventional coherent receiver

The expansion of new services such as high definition video streaming, mobility applications, has led to an increasing demand for a high-capacity photonic network. To increase the signal bit rate in the network, advanced modulation formats such as quadrature phase shift keying (QPSK) and quadrature amplitude modulation (QAM) are used. Furthermore, polarization multiplexing is applied to increase the spectral efficiency. Monolithic integration of polarization diversity coherent receiver makes the deployment of such advanced modulation formats successful thanks to its low cost and compact size [45]. Fig. 61 shows the conventional dual-polarization coherent receiver. The conventional receiver chip comprises a polarization diversity network and a phase detection network. The phase detection network is composed of two separate single polarization coherent receivers (the upper one for TE and the lower one for TM in Fig. 61). The PBS is used for the separation of the TE and TM polarized light to the corresponding coherent receiver. The 90° hybrids demodulate the phase-encoded signals into power signals which are detected by waveguide integrated PDs. The 90° hybrid can be realized using a 2x4 multi-mode interference (MMI). The 2x4 MMI can be optimized to have a PDL less than 1dB [46]. The PBS can be realized using modal evolution [47], directional couplers [48], MMI devices [49], or MZIs [50]. The PBS based on the modal evolution provides good fabrication tolerance of about 100nm [47], but its large mm-range length limits the compact size of the chip. The PBSs based on interference exhibit compact size but poor fabrication tolerance. Moreover, these PBSs are quite sensitive on the wavelength. New solutions should be found to eliminate the PBSs to get a more compact and more fabrication tolerant coherent receiver.

6.2 Advanced coherent receiver

6.2.1 Concept of the advanced coherent receiver

Based on the presented waveguide integrated MQW pin PD with a high PDL, an advanced receiver concept is demonstrated as shown in Fig. 62. For the proposed advanced receiver, only one 90° hybrid is used as phase diversity network. Four PD sets (eight waveguide integrated PDs) are used as power detecting network and

polarization diversity network. Each PD set consists of a waveguide integrated MQW pin PD and a waveguide integrated bulk pin PD. Both PDs are optically connected in series as shown in Fig. 63. The TE polarized light is evanescently coupled to the MQW PD and totally absorbed contributing to the response photocurrent. The TM polarized light is also firstly evanescently coupled to the MQW PD. Thanks to the large PDL of the MQW PD, the TM polarized light travels through the MQW PD to the following bulk PD and is converted to the photocurrent. In that case, the MQW PD detects only the TE polarized light while the bulk PD detects only the TM polarized light. As a result, the proposed PD set can be used as the polarization diversity network.

The size of the proposed advanced receiver is only 1/4 of the conventional receiver, since the two PBSs and one 90° hybrid are eliminated in the proposed advanced receiver. Furthermore, by eliminating the PBS the fabrication tolerance can be improved.

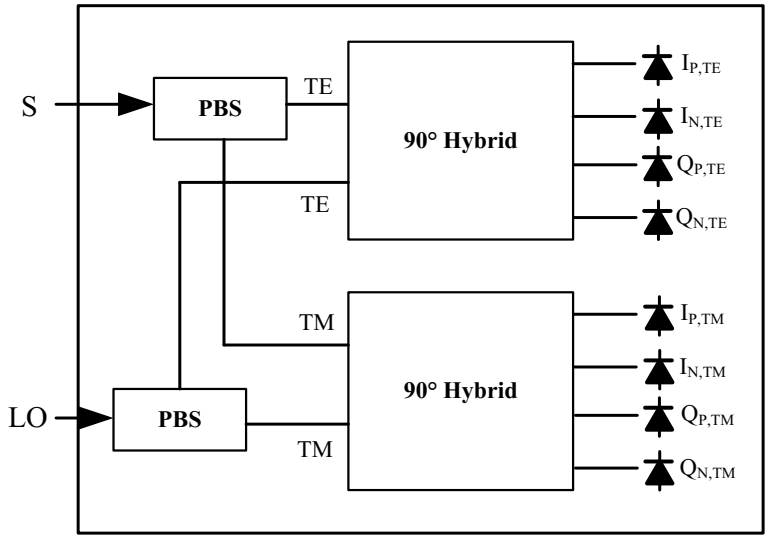

Fig. 61. Conventional concept of DP-QPSK coherent receiver chip; S – input data signal, LO – local oscillator

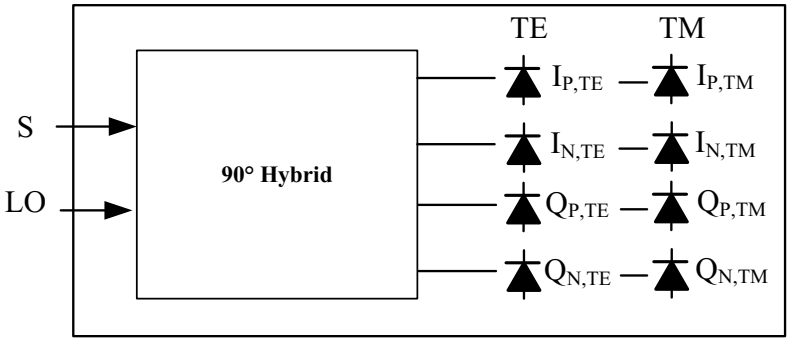

Fig. 62. Advanced concept of DP-QPSK coherent receiver chip; S – input data signal, LO – local oscillator

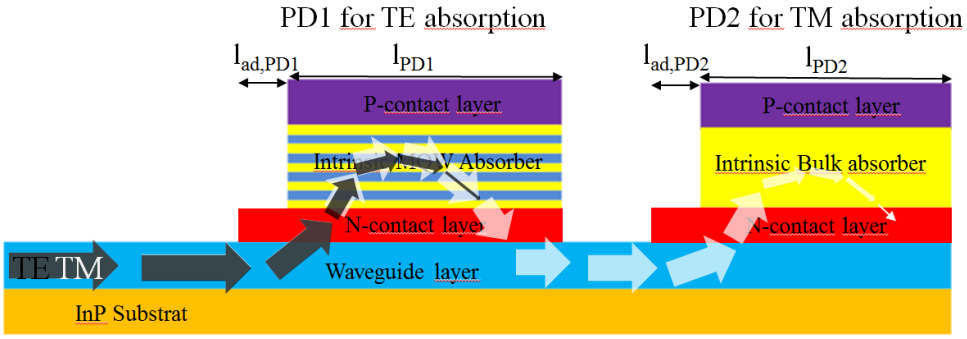

Fig. 63. The waveguide integrated PD set; a MQW pin- PD1 for TE absorption; a bulk pin PD2 for TM absorption; black arrow: propagation path of the TE polarized light; white arrow: propagation of the TM polarized light.

6.2.2 Characterization of the advanced coherent receiver

The proposed coherent receiver can be characterized in terms of responsivity, polarization splitting ratio (PSR), and polarization extinction ratio (PER).
The ratio between the photocurrents of the PD 1 and PD 2 with TE polarized input light is defined as the PSR for TE polarized input light. The ratio between the photocurrents of the PD 2 and PD 1 with TM polarized input light is defined as the PSR for TM polarized input light
for TE input light

$$PSR\ (TE) = 20log_{10}\left(R_{PD_1}/R_{PD_2}\right), \tag{120}$$

for TM input light

$$PSR\ (TM) = 20log_{10}\left(R_{PD_2}/R_{PD_1}\right). \tag{121}$$

The PER of PD1 is defined as the ratio between the photocurrents of the PD1 with TE and TM polarized input light. The PER of PD2 is defined as the ratio between the photocurrents of the PD2 with TM and TE polarized input light
for PD1

$$PER\ (PD_1) = 20log_{10}(R_{TE}/R_{TM}), \tag{122}$$

for PD2

$$PSR\ (PD_2) = 20log_{10}(R_{TM}/R_{TE}). \tag{123}$$

The epitaxial layers of the PD1 are shown in Table 11 which is the same as the design “Q1.33”. The epitaxial layers of the PD2 are shown in Table 13. The width of both PDs is 5µm. The length of the advanced waveguide of both PDs is 2µm. The length l_{PD1} of the PD1 is optimized as 34µm to couple the TM light 100%

back to the waveguide layer. The length l_{PD2} of the PD2 is set as 20µm. The responsivity, PSR, and PER can be simulated as shown in Table 9.

There are two aspects that limit the PER and PSR. One is the absorption of the TM polarized input light of the PD1. The other one is the rest of the TE polarized light which is coupled into the PD2. In order to increase the PSR and PER, The waveguide integrated MQW p-i-n PD should be optimized to achieve a large PDL, such as the new design presented in Section 5.2.5. As the future work, after fabricating and characterizing the new design of the waveguide integrated MQW p-i-n PD, the advanced coherent receiver should have better performances regarding of the PER and PSR by using the new design as PD1.

Thanks to its unique properties, the proposed advanced coherent receiver can be applied for low cost market such as fiber-to-the-home (FTTH) and Ethernet short haul data services.

Table 9 Simulated responsivity, PSR, and PER of the proposed advanced coherent receiver using the waveguide integrated MQW p-i-n PD design "Q1.33" as PD1 and bulk p-i-n PD as PD2

Wavelength [nm]	Responsivity [A/W]		PSR [dB]		PER [dB]	
	PD1 (TE)/(TM)	PD2 (TM)/(TE)	TE	TM	PD1	PD2
1530	0.69/0.45	0.35/0.12	17	2	3.6	9
1550	0.63/0.29	0.4/0.17	13	3	6.6	7.3
1570	0.54/0.17	0.45/0.22	9	9	9.8	6

7. Summary and further work

7.1 Summary

In this work waveguide integrated MQW p-i-n PDs with high PDL are studied. Firstly, the following theoretical aspects have been addressed.

1. The optical absorption in MQWs including the optical absorption due to continuum transition and due to exciton absorption was analyzed with different electrical field strengths and different polarization statuses of the input light.
2. The physical effects in waveguide integrated MQW p-i-n PDs were analyzed. The important physical effects are the carrier transit time through the MQW layers and the free carrier density in the MQWs. Furthermore, the both effects influence the internal quantum efficiency, the DC and RF saturation, the RF bandwidth, and the nonlinearity.
3. Based on the physical effects in waveguide integrated MQW p-i-n PDs, a model for MQW p-i-n PD was developed. The model accounts for optical absorption coefficient spectrum, responsivity spectrum, PDL, dark current, DC saturation of optical absorption, 3-dB bandwidth, maximal RF output power, and nonlinearity. It worth mentioning that the simulation procedure for calculating the responsivity in the model is based on Matlab and commercial light propagating software such as Fimmprop.

Three types of waveguide integrated MQW p-i-n PDs were designed and fabricated. All the three types are based on non-strained MQW layers (lattice matched to InP). The MQW layers of the design "InP" consist of $In_{0.56}Ga_{0.47}As$ as wells and InP as barriers. The MQW layers of the design "Q1.33" consist of $In_{0.56}Ga_{0.47}As$ as wells and $InGa_{0.3}As_{0.64}P$ as barriers. The MQW layers of the design "Al" consist of $In_{0.56}Ga_{0.47}As$ as wells and $In_{0.53}Ga_{0.29}Al_{0.18}As$ as barriers. The epitaxial layers of the three designs are further optimized considering the efficient optical coupling and RF electrical performances. The three designs were measured regarding of responsivity, PDL, dark current, DC saturation of optical absorption, bandwidth, maximal RF output power, and nonlinearity evaluated by OIP3. The detailed measurement results are listed in Table 8. The design "InP" shows the highest PDL values because of its strongly confined excitons in wells. Moreover, the design "InP" has the lowest dark current up to -4V due to its large transit time. However, its DC saturation of optical absorption and RF performances such as 3-dB bandwidth are limited by its large transit time. Compared to the design "InP", the design "Q1.33" and the design "Al" exhibit better RF performances thanks to their reduced transit time. However, for the design "Q1.33" and the design "Al" the confinement of excitons in wells becomes weaker by lowering their barrier heights. The weaker confinement decreases the

excitonic absorption and broadens the total absorption spectrum resulting in low PDL values. A new design of the waveguide integrated MQW p-i-n PD using compressive strained wells and tensil strained barrier is presented. The simulation results show that the new design combines the high-PDL performance of the design “InP” and the high RF performance of the design “Q1.33” and the design “Al”.

In the end, a novel advanced coherent receiver using proposed waveguide integrated MQW p-i-n PDs is demonstrated. Four sets of MQW PDs and bulk PDs are used as the polarization diversity network for the advanced coherent receiver. By eliminating PBSs and one MMI, the advanced coherent receiver shows only 1/4 area of the conventional one and more fabrication tolerances. This advanced coherent receiver can be applied for low cost market such as fiber-to-the-home (FTTH) and Ethernet short haul data services.

7.2 Future works

Using the presented model, the new design of waveguide integrated MQW p-i-n PD is simulated with an improved PDL and RF performance. As the next step, the new design should be fabricated and fully characterized in terms of responsivity, PDL, dark current, DC saturation of optical absorption, bandwidth, maximal RF output power, and nonlinearity. Afterwards, the advanced coherent receiver using the new design can be designed, fabricated, and characterized regarding of PER and PSR.

Till now, in this thesis, all the waveguide integrated MQW p-i-n PDs are realized using an evanescent coupling between the waveguide layer and the MQW p-i-n PD. A waveguide integrated MQW p-i-n PD using a butt-joint coupling between the waveguide layer and the MQW p-i-n PD can be studied. Compared to the waveguide integrated MQW p-i-n PD using the evanescent coupling, the MQW p-i-n PD using the butt-joint coupling can have a higher responsivity for TE polarized input light due to the stronger light confinement in the absorber. Moreover, for the application in the advanced coherent receiver, the size of the PD1 (the PD length and the PD width) can be more flexibly set compared to the evanescent coupling design, since the TM light through the PD1 using the butt-joint coupling will be directly coupled back to the waveguide layer regardless of the PD length.

8. Appendix

8.1 Solving Schrödinger equation using FDM

The finite-difference expression of the Schrödinger equation can be written as [51]

$$\alpha_w \varphi_{p-1} + (\alpha_x + \dot{U}_p)\varphi_p + \alpha_e \varphi_{p+1} = E\varphi_p \quad p = 1, 2, 3, \dots, j \tag{124}$$

$$\dot{U}_p = \mathrm{U}_p + \mathrm{qF}_p \mathrm{z}_p \tag{125}$$

where

$$\alpha_w = -\frac{\hbar^2}{2} \frac{2}{\Delta z_{p-1}(\Delta z_{p-1} + \Delta z_p)} \frac{2}{m^*{}_{p-1} + m^*{}_p}, \tag{126}$$

$$\alpha_e = -\frac{\hbar^2}{2} \frac{2}{\Delta z_p(\Delta z_{p-1} + \Delta z_p)} \frac{2}{m^*{}_p + m^*{}_{p+1}}, \tag{127}$$

$$\begin{aligned} \alpha_x = \frac{\hbar^2}{2} \Bigg(& \frac{2}{\Delta z_{p-1}(\Delta z_{p-1} + \Delta z_p)} \frac{2}{m^*{}_{p-1} + m^*{}_p} \\ & + \frac{2}{\Delta z_p(\Delta z_{p-1} + \Delta z_p)} \frac{2}{m^*{}_p + m^*{}_{p+1}} \Bigg) \\ & = -\alpha_w - \alpha_e. \end{aligned} \tag{128}$$

F_p is the electric field due to applied reverse bias voltage at the position of z_p, which can be calculated by solving the Poisson equation using FDM

$$-\nabla^2 V_e = \frac{\rho}{\varepsilon}, \overrightarrow{F_p} = -\nabla V_e \big| z_p \tag{129}$$

where V_e is the electrical potential in quantum wells, ρ is the local space charge density, and ε is the local permittivity.

The boundary conditions are

$$\varphi_0 = \varphi_{j+1} = 0. \tag{130}$$

Therefore, we get

$$(\alpha_{x,1} + \dot{U}_1)\varphi_1 + \alpha_{e,1}\varphi_2 = E\varphi_1, \tag{131}$$

$$(\alpha_{x,j} + \dot{U}_j)\varphi_j + \alpha_{w,j}\varphi_{j-1} = E\varphi_j. \tag{132}$$

The matrix equation can be constructed as:

$$\Lambda\{\varphi\} = E\{\varphi\} \tag{133}$$

where Λ is written as:

$$\Lambda = \begin{bmatrix} \alpha_{x,1} + \dot{U}_1 & \alpha_{e,1} & & \\ \alpha_{w,2} & \alpha_{x,2} + \dot{U}_2 & \alpha_{e,2} & \\ & \alpha_{w,p} & \alpha_{x,p} + \dot{U}_p & \alpha_{e,p} \\ & & \alpha_{w,j} & \alpha_{x,j} + \dot{U}_j \end{bmatrix}. \quad (134)$$

The matrix Λ is considered as a sparse matrix. For any band structure, the eigen energy levels E_j and their corresponding eigen wavefunctions φ_j can be obtained by using the functions of *eig()* or *eigs()* in Matlab to solve the constructed matrix equation.

8.2 Matlab codes

8.2.1 Main code

```
clear;
t0 = clock; tic;
para = [0.4,1,3,0.3,0.64,10,5E10,300];
Well.x =para(1); Well.y = para(2); Well.thickness = para(3);
Barrier.x =para(4); Barrier.y = para(5); Barrier.thickness = para(6);
Temperature = para(8);d_sub = 20;Num_mqw = 1; Num_sub = 20;h = 6.6260755E-34; h_ =
h/(2*pi);eV = 1.60217733E-19; c = 299792458; m0 = 9.1093897E-31;  % free electron mass (kg)
e0 = 8.854187817E-12;
um = 1e-6; nm = 1e-9;
Eg_well = Eg(Well.x,Well.y)*eV;
mc = m_1(Well.x,Well.y).*m0;
mhh001 = m_hh001(Well.x,Well.y)*m0;
mlh001 = m_lh001(Well.x,Well.y)*m0;
u_chh =0.04*m0;
u_clh = mc * mlh001/(mc + mlh001);
Eg_strain1 = Eg_strain(Well.x,Well.y);
permittivity_w = permittivity(Well.x,Well.y);
permittivity_b = permittivity(Barrier.x,Barrier.y);
permit = (permittivity_w*Well.thickness + permittivity_w*Barrier.thickness)/(Well.thickness +
Barrier.thickness);
InputWave=1.2:0.001:1.8;
ElectricField=10:10:50;
InputWave =InputWave'; ElectricField =ElectricField';
Index_w =3.56;Index_b = 3.41
Index_eff = (Index_w*Well.thickness + index_b*Barrier.thickness)/(Well.thickness +
Barrier.thickness);
Ry_chh = eV^4*u_chh/(8*(permit*e0*h)^2);
Ry_clh = eV^4*u_clh/(8*(permit*e0*h)^2);
B = [0.381,-0.357,0.087;-0.178,0.48,-0.343;0.138,-0.389,0.261];
delt0=(Eg(Barrier.x,Barrier.y)*eV-Eg(Well.x,Well.y)*eV)*0.6;
Mb_2 = 2* m0^2*Eg_well*(Eg_well+delt0*eV)/(12*mc*(Eg_well+2/3*delt0*eV));
Gama_0 = Gama0(Temperature);
for f = 1:length(ElectricField)%%% the first for&end
   disp(['this time is: ',num2str(toc),'s']);
   disp(['starting compute absorption at F = ',num2str(ElectricField(f)),'kV/cm']);
   pause(0.1);
   QW = Fun_FDM_Esub(Well,Barrier,Num_mqw,d_sub,ElectricField(f),Num_sub,0.4);
   Absorp_ex_TE = 0; Absorp_con_TE = 0;
   Absorp_ex_TM = 0; Absorp_con_TM = 0;
   E_light = 1.24./InputWave*eV;
   for i=1:1
   for j=1:1
        if j==i
        [Eb_hh,R_ex_hh] =
BindingEnergy(QW.position,QW.dX,Well.thickness,QW.Wave_c(:,i),QW.Wave_hh(:,j),u_chh,per
mit);
        Eb_hh = Eb_hh*eV;
        R_ex_hh =R_ex_hh*nm;
        Echhn = (Eg_strain1.c_hh + QW.Esub_c(i) + QW.Esub_hh(j))*eV;
        Eex_hh = Echhn + Eb_hh;
```

```
        Qex =
2*eV^2*h_./(e0*c*Index_eff.*m0^2.*Eex_hh.*R_ex_hh.^2*Well.thickness*nm*Num_mqw)*Mb
_2;
        Mchh_2 = abs(sum(QW.Wave_c(:,i).*conj(QW.Wave_hh(:,j)).*QW.dX))^2; % squre of
overlap integration
        Gama_hh =  (0.005+ElectricField(f)/10000)*eV;
        G = FunLorentzian(E_light, Eex_hh,Gama_hh);
        Absorp_ex_TE = Absorp_ex_TE + 3/2*Qex.*Mchh_2.*G;
        dE = 0.001*eV;
        Qcon =
u_chh*eV^2./(e0*c*Index_eff.*m0^2.*h_.*E_light*Well.thickness*nm*Num_mqw).*Mb_2;
        for E = Echhn:dE:max(E_light + 10* Gama_0)
           a0 =Echhn/E;
           u_hhj_TE = 3/4*(1+a0.^2);    % a0 <=1;
           u_hhj_TM = 3/2*(1-a0.^2);   % polarization direction factors for TE and TM
           K = FunSommerfeld(E,Echhn,Ry_chh);
           G = FunLorentzian(E, E_light, Gama_0);
           Absorp_con_TE = Absorp_con_TE + u_hhj_TE*Mchh_2.*Qcon.*K.*G*dE;
           Absorp_con_TM = Absorp_con_TM + u_hhj_TM*Mchh_2.*Qcon.*K.*G*dE;
        end
        end
      end
      for k=1:1
        if k==i
        Eclhn = (Eg_strain1.c_lh + QW.Esub_c(i) + QW.Esub_lh(k))*eV;
        [Eb_lh,R_ex_lh] =
BindingEnergy(QW.position,QW.dX,Well.thickness,QW.Wave_c(:,i),QW.Wave_lh(:,k),u_clh,per
mit);
        Eb_lh = Eb_lh*eV;
        R_ex_lh =R_ex_lh*nm;
        Eex_lh = Eclhn + Eb_lh;
        Qex =
2*eV^2*h_*Mb_2./(e0*c.*Index_eff*m0^2.*Eex_lh.*R_ex_lh.^2*Well.thickness*nm*Num_mqw
);
        Mclh_2 = abs(sum(QW.Wave_c(:,i).*QW.Wave_lh(:,k).*QW.dX))^2;
        Gama_lh =  (0.005+ElectricField(f)/10000)*eV;
        G = FunLorentzian(E_light, Eex_lh,Gama_lh);
        Absorp_ex_TE = Absorp_ex_TE + 1/2*Mclh_2.*Qex.*G;
        Absorp_ex_TM = Absorp_ex_TM + 2*Mclh_2.*Qex.*G;
        dE = 0.001*eV;
        Qcon =
u_clh*eV^2*Mb_2./(e0*c.*Index_eff*m0^2*h_.*E_light*Well.thickness*nm*Num_mqw);
        for E = Eclhn:dE:max(E_light + 10* Gama_0);
           a0 = Eclhn/E;
           u_lhk_TE = 5/4-3/4*a0.^2;
           u_lhk_TM = 1/2+3/2*a0.^2;
           K = FunSommerfeld(E,Eclhn,Ry_clh);
           G = FunLorentzian(E, E_light, Gama_0);
           Absorp_con_TE = Absorp_con_TE + u_lhk_TE*Mclh_2.*Qcon.*G.*dE;
           Absorp_con_TM = Absorp_con_TM + u_lhk_TM*Mclh_2.*Qcon.*G.*dE;
        end
        end
    end
  end
```

```
  Absorp_ex_TE = Absorp_ex_TE/100; Absorp_con_TE = Absorp_con_TE/100;   Absorp_ex_TM
= Absorp_ex_TM/100; Absorp_con_TM = Absorp_con_TM/100;
 figure;grid on; plot(InputWave,Absorp_con_TE);
 figure;grid on;plot(InputWave,Absorp_ex_TE);
  figure;grid on; plot(InputWave,Absorp_con_TM);
 figure;grid on; plot(InputWave,Absorp_ex_TM);
  Absorp_TE(:,f) = (Absorp_ex_TE + Absorp_con_TE);
  Absorp_TM(:,f) = (Absorp_ex_TM + Absorp_con_TM);
end
```

8.2.2 Subcode

Fun_FDM_Esub (for calculation of the sub energy levels and wavefunctions)

```
function  [results] =
Fun_FDM_Esub(Well,Barrier,Num_mqw,d_sub,ElectricField,Num_sub,Ec_Ratio)
tic; clear results;
m0=9.1093897*10^(-31); h=6.6260755*10^(-34); h_=h/(2*pi);
eV=1.60217733e-19; nm = 1e-9;
ElectricField = ElectricField*1e5;
Eg_w = Eg(Well.x,Well.y); Eg_b = Eg(Barrier.x,Barrier.y);
delt_Eg = Eg_b-Eg_w;
if abs(delt_Eg) < 0.001
  results.Esub_c = 0;
  results.Esub_hh = 0;
  results.Esub_lh = 0;
  return;
elseif delt_Eg < -0.001
   results = [];
   return;
end
mc_b = mc(Barrier.x,Barrier.y); mc_w=mc(Well.x,Well.y);
mhh_b = m_hhz(Barrier.x,Barrier.y); mhh_w=m_hhz(Well.x,Well.y);
mlh_b = m_lhz(Barrier.x,Barrier.y); mlh_w=m_lhz(Well.x,Well.y);
d_cover = d_sub;
mc0_sub = mc(0,0); mc0_cover = mc(0,0);
mhh_sub = m_hhz(0,0);  mhh_cover = m_hhz(0,0);
mlh_sub = m_lhz(0,0);  mlh_cover = m_lhz(0,0);
Eg_sub = Eg(0,0); Eg_cover = Eg(0,0);
d = [Barrier.thickness,Well.thickness,Barrier.thickness];
mc0 = [mc_b,mc_w,mc_b];
mhh = [mhh_b,mhh_w,mhh_b];
mlh = [mlh_b,mlh_w,mlh_b];
delt_Ec_b = (Eg_b-Eg_w)*0.4;   % the band-offset of 40:60 is used for InGaAsP/InP
Ec0 = [delt_Ec_b,0,delt_Ec_b];
delt_Ev_b = Eg_b - Eg_w - delt_Ec_b;
Ev0 = [-delt_Ev_b,0,-delt_Ev_b];
Eg_strain_w = Eg_strain(Well.x,Well.y);
Eg_strain_b = Eg_strain(Barrier.x,Barrier.y);
delt_Ec = [Eg_strain_b.d_Ec,Eg_strain_w.d_Ec,Eg_strain_b.d_Ec];
delt_Ehh = [Eg_strain_b.d_Ehh,Eg_strain_w.d_Ehh,Eg_strain_b.d_Ehh];
delt_Elh = [Eg_strain_b.d_Elh,Eg_strain_w.d_Elh,Eg_strain_b.d_Elh];
```

```
Ec = Ec0 + delt_Ec;
Ehh = Ev0 + delt_Ehh;
Elh = Ev0 + delt_Elh;
if Num_mqw >1
   for i = 2:Num_mqw
      d = [d,d(length(d)-1),d(length(d))];
      mc0 = [mc0,mc0(length(mc0)-1),mc0(length(mc0))];
      mhh = [mhh,mhh(length(mhh)-1),mhh(length(mhh))];
      mlh = [mlh,mlh(length(mlh)-1),mlh(length(mlh))];
      Ec = [Ec,Ec(length(Ec)-1),Ec(length(Ec))];
      Ehh = [Ehh,Ehh(length(Ehh)-1),Ehh(length(Ehh))];
      Elh = [Elh,Elh(length(Elh)-1),Elh(length(Elh))];
   end
end   %extent the field to Num_mqw
d = [d_sub,d,d_cover]; % add the Substrate and cover to the d[1] and d[length(d)+1]
mc0 = [mc0_sub,mc0,mc0_cover];
mhh = [mhh_sub,mhh,mhh_cover];
mlh = [mlh_sub,mlh,mlh_cover];
delt_Ec_sub = (Eg_sub-Eg_w)*0.4;
delt_Ec_cover = (Eg_sub-Eg_w)*0.4;
Ec = [delt_Ec_sub,Ec,delt_Ec_cover]-Eg_strain_w.d_Ec;%norminieren Ec_w=0
delt_Ev_sub = Eg_sub - Eg_w-delt_Ec_sub;
delt_Ev_cover = Eg_sub - Eg_w-delt_Ec_cover;
Ehh = [-delt_Ev_sub,Ehh,-delt_Ev_cover]-Eg_strain_w.d_Ehh;
Elh = [-delt_Ev_sub,Elh,-delt_Ev_cover]-Eg_strain_w.d_Elh;
V_bias = ElectricField*(sum(d)-d(1)-d(length(d)))*nm;   %V_bias unit is V;
 [x,dX,Nx0] = XY(d,100); %grid 0.1nm as step
x = x.';  dX =dX.'; d = d.';
for pp = 1:3  % pp=1,2,3, represent conduction,hh and lh band, respectively
   clear mass V;
   if pp==1
      Band = 'Conduction Band';
      m = mc0.'; E = Ec.'; sign0 = 1; Band = 'Ec';
   elseif pp == 2
      Band = 'Heavy Hole Band';
      m = mhh.'; E = Ehh.'; sign0 =-1; Band = 'Ehh';
      %V_bias = V_bias*sign0;
   else
      Band = 'Light Hole Band';
      m = mlh.'; E = Elh.';  sign0 = -1; Band = 'Elh';
   end
   mass(Nx0(1,1):Nx0(2,1)) = m(1);
   mass(Nx0(1,length(d)):Nx0(2,length(d))) = m(length(d));
   V(Nx0(1,1):Nx0(2,1)) =E(1);
   V(Nx0(1,length(d)):Nx0(2,length(d))) = E(length(d))+V_bias;
   for j = 2:length(d)-1
     V(Nx0(1,j):Nx0(2,j)) = E(j)+ElectricField*x(Nx0(1,j):Nx0(2,j))*nm;
     mass(1,Nx0(1,j):Nx0(2,j)) = m(j);
   end
   V = V -(V(Nx0(1,3))+V(Nx0(2,3)))/2;
   mass = mass.'; V = V.';
   switch  pp
      case 1
         mass_c = mass; Vc = V;
      case 2
```

```
            mass_hh = mass; Vhh = V;
        case 3
            mass_lh = mass; Vlh = V;
    end
    W0 = sum(d)*nm;
    E0 = (h_*pi)^2/(2*m0*W0^2)/eV;
    [Energe0,Wave0] = fdm1d(x*nm/W0,dX*nm/W0,mass,V*sign0/E0,Num_sub);  %% length and
energe are normilized.
    Energe0 = Energe0*E0;
    for i = 1:Num_sub
        Esub(i) = Energe0(i,i);
        a = sum(Wave0(:,i).*conj(Wave0(:,i)).*dX);
        Wave(:,i) = Wave0(:,i)./sqrt(a);
     end
    Wave = Wave(:,1:length(Esub));
   if pp ==1
      results.Esub_c = Esub;
      results.delt_Ec = min(V(Nx0(2,2)),V(Nx0(1,length(d)-1))) - Esub;
      results.Wave_c = Wave;
    elseif pp ==2
      results.Esub_hh = Esub;
      results.delt_Ev_hh = min(-V(Nx0(2,2)),-V(Nx0(1,length(d)-1))) - Esub;
      results.Wave_hh = Wave;
    else
      results.Esub_lh = Esub;
      results.delt_Ev_lh = min(-V(Nx0(2,2)),-V(Nx0(1,length(d)-1))) - Esub;
      results.Wave_lh = Wave;
    end
end
results.position = x; results.dX = dX;
```

BindingEnergy (for calculation of bindingenergy and bohr radius of excitons)

```
function [Eb,R_ex] = BindingEnergy(z,dz,d_well,wave1,wave2,mass,permittivity)
h = 6.6260755E-34; h_ = h/(2*pi);
eV = 1.60217733E-19;
m0 = 9.1093897E-31;  % free electron mass (kg)
nm = 10^-9;
z = z*nm; dz = dz*nm;
Lambda0 = 2.0*d_well;
while 1
    tic;
    Lambda = d_well/2:0.2:Lambda0;
    Lambda = Lambda*nm;
    Eb0 = h_^2./(2*mass*Lambda.^2);
    Eb = 0; N=0;
    r0 = 2*Lambda0*nm; dr = 1*nm;
    dd = dz(1)*dz(1)*dr;
    for i=1:length(z)
        A = wave1(i)*conj(wave1(i));
        for j = 1:length(z)
            B = wave2(j)*conj(wave2(j));
```

```
        dd = dz(i)*dz(j)*dr;
        r =0.1*nm:dr:r0;
            C = wave_cv(r,Lambda)^2;
            D = V_ev(z(i),z(j),r,permittivity);
            N = 2*pi*A*B*sum(r*C)*dd;
            Eb = Eb+2*pi*A*B*C*D*r*dd;
    end
end
toc
Eb = Eb./N + Eb0;
[Eb,n] = min(Eb); R_ex = Lambda(n);
Eb = Eb/eV; R_ex = R_ex/nm;
if R_ex<Lambda0-2
    break;
else
    Lambda0 = Lambda0+10;
end
```

Sommerfeld function

```
function K = FunSommerfeld(E_light,E,Ry)
K = 2./(1+exp(-2*pi.*((E_light - E)/Ry).^0.5));
```

Lorentzian function

```
function L = FunLorentzian(E_light,E,Gama_hom)
eV = 1.60217733E-19;
L = Gama_hom./(pi*((E_light - E).^2 + Gama_hom.^2));
```

8.3 List of epitaxial layer

Table 10 Epitaxy layers of the design “InP”

Function		Material	Thickness/nm	Doping	
Substrate		InP	~600μm	undoped	W8
Waveguide layer		InGaAsP/InP	>3μm	undoped	W7
N-contact		InGaAsP	320	n+	W6
Non-strain well	x30	InGaAs	8	undoped	W5
barrier		InP	10	undoped	
Grading layer 2		InGaAsP	30	p-	W4
Cladding layer		InGaAsP	180	p-	W3
Grading layer 1		InGaAsP	200	p+	W2
P-contact		InGaAs	80	p++	W1

Table 11 Epitaxy layers of the design “Q1.33”

Function		Material	Thickness/nm	Doping	
Substrate		InP	~600μm	undoped	W8
Waveguide layer		InGaAsP /InP	>3μm	undoped	W7
N-contact		InGaAsP	200	n+	W6
SCH		Q1.33	10	undoped	W5
Non-strain well	x20	InGaAs	6.5	undoped	
barrier		Q1.33	10	undoped	
SCH		Q1.33	100	undoped	
Grading layer 2		InGaAsP	200	p-	W4
Cladding layer		InGaAsP	180	p-	W3
Grading layer 1		InGaAsP	200	p+	W2
P-contact		InGaAs	80	p++	W1

Table 12 Epitaxy layers of the design “Al”

Function		Material	Thickness/nm	Doping	
Substrate		InP	~600µm	undoped	W8
Waveguide layer		InGaAsP/InP	>3µm	undoped	W7
N-contact		InGaAsP	320	n+	W6
SCH		InGaAlAs	50	undoped	W5
Non-strain well	x20	InGaAs	7.5	undoped	
barrier		InGaAlAs	10	undoped	
SCH		InGaAlAs	100	undoped	
Grading layer 2		InGaAlAs	200	p-	W4
Cladding layer		InP	180	p-	W3
Grading layer 1		InP	210	p+	W2
P-contact		InGaAs	80	p++	W1

Table 13 Epitaxy layers of the PD2 for the advanced coherent receiver

Function	Material	Thickness/nm	Doping	
Substrate	InP	~600µm	undoped	W8
Waveguide layer	InGaAsP /InP	>3µm	undoped	W7
N-contact	InGaAsP	200	n+	W6
Absorber	InGaAs	480	undoped	W5
Grading layer 1	InGaAsP	30	p-	W4
Cladding layer 2	InGaAsP	200	p-	W3
Grading layer	InGaAsP	220	p+	W2
P-contact	InGaAs	80	p++	W1

Table 14 Epitaxy layers of the new design

Function		Material / Strains	Thickness/nm	Doping	
Substrate		InP	~600µm	undoped	W8
Waveguide layer		InGaAsP/InP	>3µm	undoped	W7
N-contact		InGaAsP	320	n+	W6
SCH		InGaAsP	10	undoped	W5
Non-strain well	x20	InGaAs	3.5	undoped	
barrier		InGaAsP	10	undoped	
SCH		InGaAsP	100	undoped	
Grading layer 2		InGaAsP	200	p-	W4
Cladding layer		InGaAsP	180	p-	W3
Grading layer 1		InGaAsP	200	p+	W2
P-contact		InGaAs	80	p++	W1

8.4 List of symbols

2D	Two dimentional
3D	Three dimentional
AC	Alternating current
BCB	Benzocyclobuten
c.b	Conduction band
CW	Continuous wave
DBR	Distributed bragg reflector laser
DC	Direct current
DFB	Distributed feedback laser
DUT	Device under test
e	Electron
EAM	Electroabsorption modulator
EDFA	Erbium doped fiber amplifier
FKE	Franz-Keldysh effect
FoM	Figure of merit
FTTH	Fiber to the home
Ge	Germanium
hh	Heavy hole
hh-c	Heavy hole to conduction
HHI	Heinrich-Hertz-Institute
ICP	Inductively coupled plasma
IMD3	Third order intermodulation distortion
InGaAlAs	Indium gallium aluminum arsenide
InGaAs	Indium gallium arsenide
InGaAsP	Indium gallium arsenide phosphide
InP	Indium phosphide
lh	Light hole
lh-c	Light hole to conduction
MIM	Metal insulator metal
MMI	Multimode interference
MOVPE	Metal organic vapor phase epitaxy
MQW	Multi quantum well
MZM	Mach-zehnder modulator
NiCr	Nickel chromium
O/E	Opto-electronic
OIP3	Third order output intercept point
PBS	Polarization beam splitter
PD	Photodetector
PDL	Polarization dependent loss
PER	Polarization extinction ratio
PSR	Polarization splitting ratio
QAM	Quadrature amplitude modulation
QCSE	Quantum-confined Stark effect
QPSK	Quadrature phase shift keying

QW	Quantum well
RC	Resistance capacitance
RF	Radio frequency
SEM	Scanning electron microscope
Si	Silicon
SiGe	Silicon Germanium
SiNx	Silicon nitride
SL	Superlattice
SMF	Single mode fiber
SOA	Semiconductor optical amplifier
SQW	Single quantum well
TE	Transverse electric
TiOx	Titanium Dioxide
TLS	Tunable laser source
TM	Transverse magnetic
V	Voltage
v.b	Valence band
VOA	Variable optical attenuator
WG	Waveguide

8.5 List of abbreviations

$A(\mathbf{r})$	Vector potential of the photon [V]
a_c	Hydrostatic deformation potential for conduction band [eV]
a_e	Lattice constant of a epitaxial layer [m]
a_s	Lattice constant of the substrate [m]
a_v	Hydrostatic deformation potential for valence band [eV]
b	Shear deformation potential for valence band [eV]
c	Velocity of the light in vacuum 3x108 [m/s]
C’	Barrier capacitance in the depletion region [F]
C_p	Parasitic capacitance [F]
C_{PD}	Total capacitance of PD [F]
D_b	Thickness of the barrier [m]
D_d	Thickness of the depletion region [m]
D_w	Thickness of well [m]
e	Electron charge [C]
E	Energy [eV]
E_b	Binding energy [eV]
E_{ex}	Exciton total energy [eV]
E_g	The bandgap energy of a material [eV]
$E_{g,e\text{-}hh}$	Band gap of the electron-heavy hole pair [eV]
$E_{g,e\text{-}lh}$	Band gap of the electron-light hole pair [eV]
E_j	Energy of the j^{th} discrete states [eV]
E_k	Kinetic energy [eV]
E_t	Eigenenergy in plane direction [eV]
E_z	Eigenenergy in z direction [eV]
F	Electric field strength [V/m]
$F(\mathbf{r})$	Envelope function
f_{3dB}	Bandwidth, -3dB cut-off frequency
f_c	Probability of the occupied conduction band state
f_{RC}	RC limited bandwidth [Hz]
f_t	Transit time limited bandwidth [Hz]
f_v	Probability of the occupied valence band state
G	Elastic stiffness factor
h	Planck constant [Js]
ħ	Reduced Planck constant [Js]
h_c	Critical thickness [m]
$H_i(F)$	Barrier height [eV]
H_{RC}	Transfer function due to RC [dB]
H_t	Transfer function due to transit time [dB]
I_0	Reverse saturation current [A]
i_L	AC current at load resistance [A]
I_{PD}	Photogenerated current [A]
I_s	Saturation density [W/m^2]
$\mathbf{k}$	Wave vector
k_B	Boltzmann’s constant

k_BT	Thermal energy [eV]
l	Length [m]
l_{PD}	Length of PD [m]
L_{PD}	Inductance of PD [H]
l_{pi}	The beat length [m]
m	Mass [kg]
m*	Effective mass [kg]
m_e*	Effective mass of electron [kg]
m_{hh}*	Effective mass of heavy hole [kg]
m_{lh}*	Effective mass of light hole [kg]
M_T	Transition matrix element
mW	Mill watt
N	Carrier density [cm^{-3}]
n	Refractive index
$n_{absorber}$	The refractive index of the absorber
N_{eff}	The effective index of a mode
n_F	Ideality factor
$n_{n\text{-}contact}$	The refractive index of the n-contact layer
$n_{waveguide}$	The refractive index of the waveguide layer
p	Momentum [kg·m/s]
P_0	CW optical input power [W]
PDL	Polarization dependent loss [dB]
P_L	RF output power [W]
P_{max}	Maximum RF output power [W]
P_s	Saturation power [W]
R	Responsivity [A/W]
r	Position vector
R_0	Surface reflectance
R_{ideal}	Ideal responsivity [A/W]
R_L	Load resistance [Ω]
R_{max}	Maximum responsivity [A/W]
R_{min}	Minimum responsivity [A/W]
R_P	Parallel resistance [Ω]
R_s	Series resistance [Ω]
R_{tot}	Total resistance
R_y	Rydberg constant
S	In-plane area [m^2]
S_{abs}	Area of absorber cross section [m^2]
T	Temperature [K]
u()	Bloch function
V	Applied voltage [V]
V(z)	Position dependent potential [V]
v_e	Drift velocity of electrons [m/s]
v_h	Drift velocity of holes [m/s]
w_{PD}	Width of PD [m]
z	Position variable [m]

α_c	Absorption coefficient of the band-to-band transition [cm^{-1}]
β	The propagation constant [1/m]
Γ	Broadening width [eV]
Δ	Spin orbit splitting energy of the valence bands [eV]
ΔE_c	Conduction band energy difference [eV]
ΔE_g	Bandgap energy difference [eV]
ΔE_v	Valence band energy difference [eV]
$\varepsilon_{//}$	In-plane strain
ε_0	Permittivity of free space [As/Vm]
ε_r	Relative permittivity
η_{ext}	External quantum efficiency
η_i	Internal quantum efficiency
λ	Wavelength of light [m]
λ_{ex}	Bohr radius of the exciton [m]
λ_g	Wavelength in vacuum equivalent to the bandgap [m]
μ	Reduced mass [mg]
μm	Micro meter
μ_n	Carrier mobility of electrons [$cm^2/(V.s)$]
μ_p	Carrier mobility of holes [$cm^2/(V.s)$]
μW	Micro watt
ρ	Density of state
τ	Carrier transit time [s]
$\tau_{lifetime}$	Carrier lifetime [s]
$\tau_{recombination}$	Carrier recombination time [s]
τ_{therm}	Carrier thermal transit time [s]
τ_{tunnel}	Carrier tunneling transit time [s]
φ	Wave function
ω	Angular frequency [Hz]
Π_{xy}	Light confinement factor
$\dot{D}_p$	Diffusion coefficient for holes [cm^2/s]
$\dot{D}_n$	Diffusion coefficient for electrons [cm^2/s]
$b_\Upsilon{}^2 a_{3,\Upsilon}$	Nonlinear coefficient of the parameters of R, τ, R_{tot} and C_{PD}
$\frac{1}{b_\Upsilon{}^2 a_{3,\Upsilon}}$	Linear coefficient of the parameters of R, τ, R_{tot} and C_{PD}

9. References

[1] J. Peter S. Zory, Quantum Well Lasers, ACADEMIC PRESS, INC., 1993.

[2] G. L. Li, "Optical Intensity Modulators for Digital and Analog Applications," *J. of Lightwave Technology*, vol. 21, no. 9, pp. 2010-2030, 2003.

[3] M. O. Manasreh, Semiconductor Quantum Wells and Superlattices for Long-Wavelength Infrared Detectors, ARTECH HOUSE, INC., 1993.

[4] D. A. B. Miller, „Optical Physics of Quantum Wells," USA.

[5] C. R. Doerr, "Highly Integrated Monolithic Photonic Integrated Circuits," in *Proceedings European Conference on Optical Communications (ECOC)* , London, 2013.

[6] K. Wakita and I. Kotaka, "Multiple-quantum-well optical modulators and their monolithic integration with DFB lasers for optical fiber communication," *Microwave and Optical Technol. Lett.*, vol.7, no.3, pp. 120-128, 1994..

[7] R. Nagarijan et al., "Single-chip 40-channel InP transmitter photonic integrated circuit capable of aggregate data rate of 1.6 Tbit/s," *Electron. Lett.*, vol. 42, no. 13, pp. 771-773, 2006.

[8] T. Yoshimatsu et al., "100 Gbit/s error-free retiming operation of monolithic optical gate integrating with photodiode and electroabsorption modulator," *Electron Lett.*, vol. 40 no.10, 2004.

[9] J. W. Raring et al., "Single-Chip 40Gb/s Widely-Tunable Transceivers with Integrated SGDBR Laser, QW EAM, UTC Photodiode, and Low Confinement SOA," *Proceedings Optical Fiber Communications Conference and Exhibition (OFC)*, Anaheim, 2006.

[10] J. Dries, M. R. Gokhale, S. R. Forrest and G. H. Olsen, "A 2.0 um Cutoff Wavelength Separate Absorption, Charge, and Multiplication Layer Avalanche Photodiode Using Strain-Compensated InGaAs Quantum Wells," *Proceedings 11th International Conference on Indium Phosphide and Related Materials (IPRM), WeA1-6*, Davos, 1999.

[11] P. Chaisakul, D. Marris-Morini, G. Isella, D. Chrastina, X. L, Roux, S. Edmond, E. Cassan, J. R. Coudevylle and L. Vivien, "Ge/SiGe multiple quantum well photodiode with 30GHz bandwidth," *APPLIED PHYSICS LETTERS, vol. 98, pp. 332-334,* 2011.

[12] T. Bhowmick and T. Das, "Integrated MQW intermixed InGaAsP/InP waveguide

photodiodes," *Opt. Quant. Electrons*, vol 42, pp. 109-120, 2010..

[13] S. Agashe, K. T. Shju and S. R. Forrest, "Integratable High Linearity Compact Waveguide Coupled Tapered InGaAsP Photodetectors," *IEEE JOUNRAL OF QUANTUM QUANTUM ELECTRONICS*, vol. 43, no.7, pp. 597-606, 2007.

[14] S. Ramo, "Current induced by electron motion," in *Proceedings of the I. R. E*, 1939.

[15] S. Sze, Physics of Semiconductor Devices, A WILEY-INTERSCIENCE PUBLICATION, 1981.

[16] A. Beling, "Periodic Travelling Wave Photodetector with Serial and Parallel Optical Feed Based on InP," *P.h.D Thesis*, Technische Universität Berlin, 2006.

[17] K. Kato, S. Hata, K. Kawano and A. Kozen, "Design of Ultrawide-band, High-Sensitivity p-i-n Photodetectors," *IEICE Transactions on Electronics*, vol. E76-C, no. 2, pp. 214-221, 1993.

[18] K. Kato, „Ultrawide-Band/High-Frequency Photodetectors," *IEEE Tran. on Microwave Theory and Techniques*, vol. 47, no. 7, pp. 1265-1281, 1999.

[19] Y.-G. Wey, "100-GHz GaInAs/InP Double Heterostructure p-i-n Photodetectors," *J. Lightwave Technol.*, vol. 13, no. 7, pp. 1490-1499, 1995.

[20] K. Kato, "110GHz 50% efficiency mushroom mesa waveguide p-i-n photoiode for a 1.55um wavelength," *IEEE Photon. Technol. Lett.*, vol.6, no.6, pp. 719-721, 1994.

[21] G. Unterbörsch, "High-power performance of a high-speed potodetector," in *Proceedings European Conference on Optical Communications (ECOC),* pp. 67-68, Madrid, 1998.

[22] R. T. Weidner and R. L. Sells, Elementary Modern Physics, *Boston: Allyn and Bacon*, 1980.

[23] P. Harrison, Quantum wells, wires and dots, *West Sussex, England: John Wiley and Sons Ltd.*, 2005.

[24] R. L. Liboff, Introductory quantum mechanics, *Oakland: Holden-Day,* 1980.

[25] W. Y. Liang, Excitons, *Physics Education*, vol. 5, no. 4, 1970.

[26] J. Minch, S. H. Park, T. Keating and S. L. Chuang, "Theory and Experiment of In1-xGaxAsyP1-y and In1-x-yGaxAlyAs Long-Wavelength Strained Quantum-Well Lasers," *IEEE Journal of Quantum Electronics,* vol. 35, no. 5, 1999.

[27] A. Braun, K. M. Briggs and P. Boni, "Analytical solution to Matthews' and Blakeslee's critical dislocation formation thickness of epitaxially grown thin films," *Journal of Crystal Growth*, vol. 241, iss.1-2, pp. 231-234, 2002.

[28] M. Sugawara, T. Fujii, S. Yamazaki and K. Nakajima, "Theoretical and experimental study of the optical-absorption spectrum of exciton resonance in In0.53Ga0.47As/InP quantum wells," *Physical Review B*, vol. 42, iss. 15, pp. 42-52, 1990.

[29] O. Madelung, Introduction to solid-state theory, *Berlin: Springer-Verlag*, 1978.

[30] H. C. Casey and M. B. Panish, Heterostructure Lasers; Part A: Fundamental principles, *Orlando, Florida: Academic Press*, 1978.

[31] D. A. B. Miller, D. S. Chemla, T. C. Damen, A. C. Gossard, W. Wiegmann, T. H. Wood and C. A. Barrus, "Electric field dependence of optical absorption near the band gap of quantum-well structures," *Phys. Rev B*, vol. 32, iss. 2, pp. 1043-1060, 1985.

[32] P. J. Stevens, M. Whitehead, G. Parry and K. Woodbridge, "Computer modeling of the electric field dependent absorption spectrum of multiple quantum well material," *IEEE J. Quantum Electron.*, vol. 24,iss. 10, pp. 2007-2016, 1988.

[33] C. Arena, B. Rotelli and L. Tarricone, "Analysis of exicton absorption peak braodening contributions in InGaAs/InP multi quantum wells," *phys. stat. sol. (b)*, vol. 185, Iss. 2, pp. 505-511, 1994.

[34] A. M. Fox, D. A. B. Miller, G. Livescu, J. E. Cunningham and W. Y. Jan, "Quantum Well Carrier Sweep Out: Relation to Electroabsorption and Exciton Saturation," *IEEE J. Quantum Elctron.*, vol. 27, no. 10, pp. 2281-2295, 1993.

[35] H. Schneider and K. V. Klitzing, "Thermionic emission and Gaussian transport of holes in a GaAs/AlxGa1-xAs multiple-quantum-well structure," *Physical Review B*, vol. 38, iss. 9, pp. 6160-6165, 1988.

[36] E. X. Ping and H. X. Jiang, "Effect of charge-carrier screening on the exciton binding energy in GaAs/AlxGa1-xAs quantum well," *Physical Review B*, vol. 47, iss. 23, pp. 2101-2106, 1993.

[37] S. Hunsche, K. Leo and H. Kurz, "Exciton absorption saturation by phase-space filling: influence of carrier temperature and density," *Physical Review B*, vol. 49, no. 23, pp. 16565-16568, 1994.

[38] A. M. Fox, D. A. B. Miller, G. Liyescu and J. E. Cunningham, „Exciton saturation in electrically biased quantum wells," *Appl. Phys. Lett.*, vol. 57, no. 22, 1990.

[39] S. Adachi, Properties of Semiconductor Alloys Group-IV, III-V and II-VI Semiconductors, *John Wiley & Sons*, 2009.

[40] E. H. Li, "Material parameters of InGaAsP and InAlGaAs systems for use in quantum well structures at low and room temperatures," *Physica E: Low-dimensional Systems and Nanostructures*, vol. 5, iss.. 4, pp. 215-273, 2000.

[41] E. Gombia et al., "Vertical transport through GaAs/InGaP multi-quantum-wells p-i-n diode with evidence of tunneling effects," *Journal of Applied Physics*, vol. 110, iss. 10 pp. 103704-103704-10, 2011.

[42] M. Corparation, THE PIN DIODE CIRCUIT DESIGNER'S HANDBOOK, *Santa Ana, California: Microsemi Corparation*, 1992.

[43] H. Ito, S. Kodama, Y. Muramoto, T. Furuta, T. Nagatsuma and T. Ishibashi, "High-Speed and High-Output InP–InGaAs Unitraveling-Carrier Photodiodes," *Journal of Selected Topics in Quantum Electronics*, vol. 10, no. 4, pp- 709-727, 2004.

[44] B. Sermage, J. L. Benchimol and G. M. Cohen, "Carrier lifetime in p-doped InGaAs and InGaAsP," in *Proceedings 10th International Conference on Indium Phosphide and Related Materials (IPRM),* Paper Fa1-4, 1998.

[45] R. Zhang, P. Runge, G. Zhou, R. Klötzer, D. Pech, H.-G. Bach, D. Perez-Galacho, A. Ortega-Murnox, R. Halir and I. Molina-Fernandez, "56Gbaud DP-QPSK Receiver Module with a Monolithic Integrated PBS and 90° Hybrid InP Chip," in *Proceeding 26th International Conference on Indium Phosphide and Related Materials (IPRM)*, Mintpellier, France, 2014, pp. We-B1-4.

[46] R. Kunkel, H.-G. Bach, D. Hoffmann, G. Mekonnen, R. Zhang, D. Schmidt, M. Schell, A. R. Monux, R. Halir and I. Molina-Fernandez, "Athermal InP-based 90°-hybrid Rx OEICs with pin-PDs >60 GHz for coherent DP-QPSK photoreceivers," in *International Conference on Indium Phosphide & Related Materials (IPRM)* , Takamatsu, Japan, 31 May-4 June 2010.

[47] W. Yuan, K. Kojima, B. Wang, T. Koike-Akino, K. Parsons, S. Nishikawa and E. Yagyu, "Mode-evolution-based polarization rotator-splitter design via simple fabrication process," *Optics Express*, vol. 20, no.9, pp. 10163-10169, 18 April 2012.

[48] T. Yamazaki, H. Aono, J. Yamauchi and H. Nakano, "Coupled waveguide polarization splitter with slightly different core widths," *Journal of Lightwave Technology*, vol. 26, no. 21, pp. 3528-3533, 20 November 2008.

[49] Y. Jiao and Y. H. S. Shi, "Shortened Polarization Beam Splitters With Two Cascaded Multimode Interference Sections," *IEEE Photonics Technology Letters*, vol. 21, no. 20,

pp. 1538-1540, 15 October 2009.

[50] D. Dai, Z. Wang, J. Peters and J. E. Bowers, "Compact Polarization Beam Splitter Using an Asymmetrical Mach–Zehnder Interferometer Based on Silicon-on-Insulator Waveguides," *IEEE Photonics Technology Letters*, vol. 24, no. 8, pp. 673-675, 8 April 2012.

A. List of publications

G. Zhou and P. Runge, "Nonlinearities of High-Speed pin Photodiodes and MUTC Photodiodes," *IEEE Transactions on Microwave Theory and Techniques*, vol. 65, iss. 6, pp. 2063-2072, June 2017 (DOI: 10.1109/TMTT.2016.2645152).

G. Zhou, P. Runge, S. Keycaninia, S. Seifert, W. Ebert, S. Mutschall, A. Seeger, Q. Li, and A. Beling, "High-Power InP-Based Waveguide Integrated Modified Uni-Traveling-Carrier Photodiodes," *IEEE Journal of Lightwave Technology*, vol. 35, iss: 4, pp. 717-721, Feb. 2017 (invited) (DOI: 10.1109/JLT.2016.2591266).

G. Zhou and P. Runge, "Modeling of Multiple-Quantum-Well p-i-n Photodiodes*," IEEE Journal of Quantum Electronics*, vol. 50, iss. 4, pp. 220-227, April 2014.

G. Zhou, P. Runge, W. Ebert, A. Seeger, and M. Schell, "A Concept for Polarization Diversity Detection Using Waveguide Integrated Multiple Quantum Well Photodiodes," *Proceedings 27th Internatioanl Conference on Indium Phosphide and Related Materials (IPRM),* paper: Tu3O4, Santa Barbara, CA USA, 28 June – 2 July, 2015.

G. Zhou, P. Runge, S. Lankes, A. Seeger, and M. Schell, "Waveguide integrated pin-photodiode array with high power and high linearity," *Proceedings IEEE Internaltional Topical Meeting on Microwave Photonics (MWP)*, paper: TuC-1, 26-29 Oct., Paphos, Cyprus, 2015.

G. Zhou and P. Runge. "PDL optimization in waveguide MQW pin photodiodes," *Proceedings 14th International Conference on Numerical Simulation of Optoelectronic Devices (NUSOD)*, Palma de Mallorca, Spain, 1-4 Sept., 2014.

G. Zhou, W. Ebert, S. Mutschall, A. Seeger, P. Runge, Q. Li, and A. Beling, "High-power waveguide integrated modified uni-traveling-carrier (UTC) photodiode with 5 dBm RF output power at 120 GHz," *Proceedings Optical Fiber Communications Conference and Exhibition (OFC)*, paper: Tu2D.3, 20-24 March, Anaheim, CA USA, 2016.

P. Runge, G. Zhou, T. Beckerwerth, F. Ganzer, S. Keyvaninia, S. Seifert, W. Ebert, S. Mutscall, A. Seeger, and M. Schell, "Waveguide Integrated Balanced Photodetectors for Coherent Receivers," *IEEE Journal of Selected Topics in Quantum Electronics*, vol. 24, iss. 2, Mar. 2018 (DOI: 10.1109/JSTQE.2017.2723844).

P. Runge, G. Zhou, F. Ganzer, S. Seifert, S. Mutscall, and A. Seeger, "Polarisation Insensitive Coherent Receiver PIC for 100Gbaud Communication," *Proceedings Optical Fiber Communications Conference and Exhibition (OFC)*, paper: Tu2D.5, 20-24 March, Anaheim, CA USA, 2016.

P. Runge, G. Zhou, S. Keyvaninia, S. Seifert, W. Ebert, A. Seeger, Q. Li, and A. Beling, "Waveguide Integrated Balanced MUTC Photodiode," *Proceedings Conference on Lasers and Electro-Optics (CLEO)*, paper: STh1G.4, 5-10 June, San Jose, CA USA, 2016.

P. Runge, G. Zhou, F. Ganzer, S. Mutschall, and A. Seeger, "Waveguide Integrated InP-Based Photodetector for 100Gbaud Applications Operating at Wavelengths of 1310nm and 1550nm," *Proceedings European Conference on Optical Communication (ECOC)*, pp. 1-3, Valencia Spain, 2015.

P. Runge, G. Zhou, A. Seeger, K. Janiak, J. Stephan, E. Rouvalis, and D. Trommer, "80GHz Balanced Photodetector Chip for Next Generation Optical Networks," *Proceedings Optical Fiber Communications Conference and Exhibition (OFC)*, paper: M2G.3, 09-13 March, San Francisco, CA USA, 2014.

P. Rung, F. Ganzer, G. Zhou, R. Zhang, A. Seeger, M. Schell, P. J. Reyes-Iglesias, D. Perez-Galacho, A. Ortega-Monux, and I. Molina-Fernandez, "Monolithic integrated InP receiver chip for coherent phase sensitive detection in the C- and L-band for colorless WDM applications," *Proceedings 40th European Conference on Optical Communications (ECOC)*, Cannes, France, p.2.2., 2014.

RY. Zhang, P. Runge, G. Zhou, R. Klotzer, D. Pech, HG. Bach, D. Perez-Galacho, A. Ortega-Murnox, R. Halir, and I. Molina-Fernandez, "56Gbaud DP-QPSK Receiver Module with a Monolithic Integrated PBS and 90 degrees Hybrid InP Chip," *Proceedings 26th Internatioanl Conference on Indium Phosphide and Related Materials (IPRM)*, Montpellier, France, 11-15 May, 2014.

D. Perez-Galacho, RY. Zhang, A. Ortega-Monux, R. Halir, C. Alonso-Ramos, P. Rung, K. Janiak, G. Zhou, HG. Back, AG. Steffan, and I. Molina-Fernandez, "Integrated Polarization Beam Splitter for 100/400 GE Polarization Multiplexed Coherent Optical Communications," *IEEE Journal of Lightwave Technology*, vol. 32, iss. 3, Feb. 2014.

C. Yao, HG. Bach, RY. Zhang, G. Zhou, JH. Choi, CH, Jiang, and R: Kunkel, "An ultracompact multimode interference wavelength splitter employing asymmetrical multi-section structures," *Optics Express*, vol. 20, iss. 16, 30 Jul., 2012.

B. Acknowledgment

Finaaaally, after about 5.5 years… Lots of things happened in the last 5.5 years. I met the two most important persons in my life: my beautiful wife and my lovely son. First of all, I would like to express my deepest thanks to my family, especially my parents and my parents in law for supporting me and trusting in me.

I would like to express my sincere gratitude to my dissertation supervisor Professor K. Petermann from Technischen Universität Berlin for his guidance. I would like to acknowledge Prof. M. Schell to give me the opportunity to work in Fraunhofer Heinrich-Hertz-Institute and do my Ph.D research. Many thanks are given to Prof. A. Stöhr to be my third supervisor of my dissertation.

Furthermore, I would like to thank Dr. Patrick Runge as well. Firstly, he helped me a lot to fix the topic of my dissertation. During my Ph.D study, he supported me and gave me lots of valuable advices. Without him, I will not finish my Ph.D in time.

I will thank Dr. Bach for the fruitful discussions. He teaches me a lot, especially the theories of the photonic devices. Every talk with him opens another window of the view for me.

I would like to thank my colleges and former colleges, Klemens Janiak, Shahram Keyvaninia, Felix Ganzer, Sten Seifert, Tobias Beckerwerth, Detlef Hoffmann, Lara Sophie Hoppe, Alex Schindler… It is one of the most treasured time to work with you. By the way, thank you for correcting my German language to help me to improve. ☺

In the end, I will thank my friends, Ruiyong Zhang, Lu You, Chenghui Jiang, Lei Yan, Chen Yao, Feng Yin, Liang Zhang…. You make my life colorful. Friendship lasts forever.